MAGNETOM Flash

The Magazine of MR

Issue Number 1/2008
ISMRM Edition

SIEMENS

Clinical

Technology

38

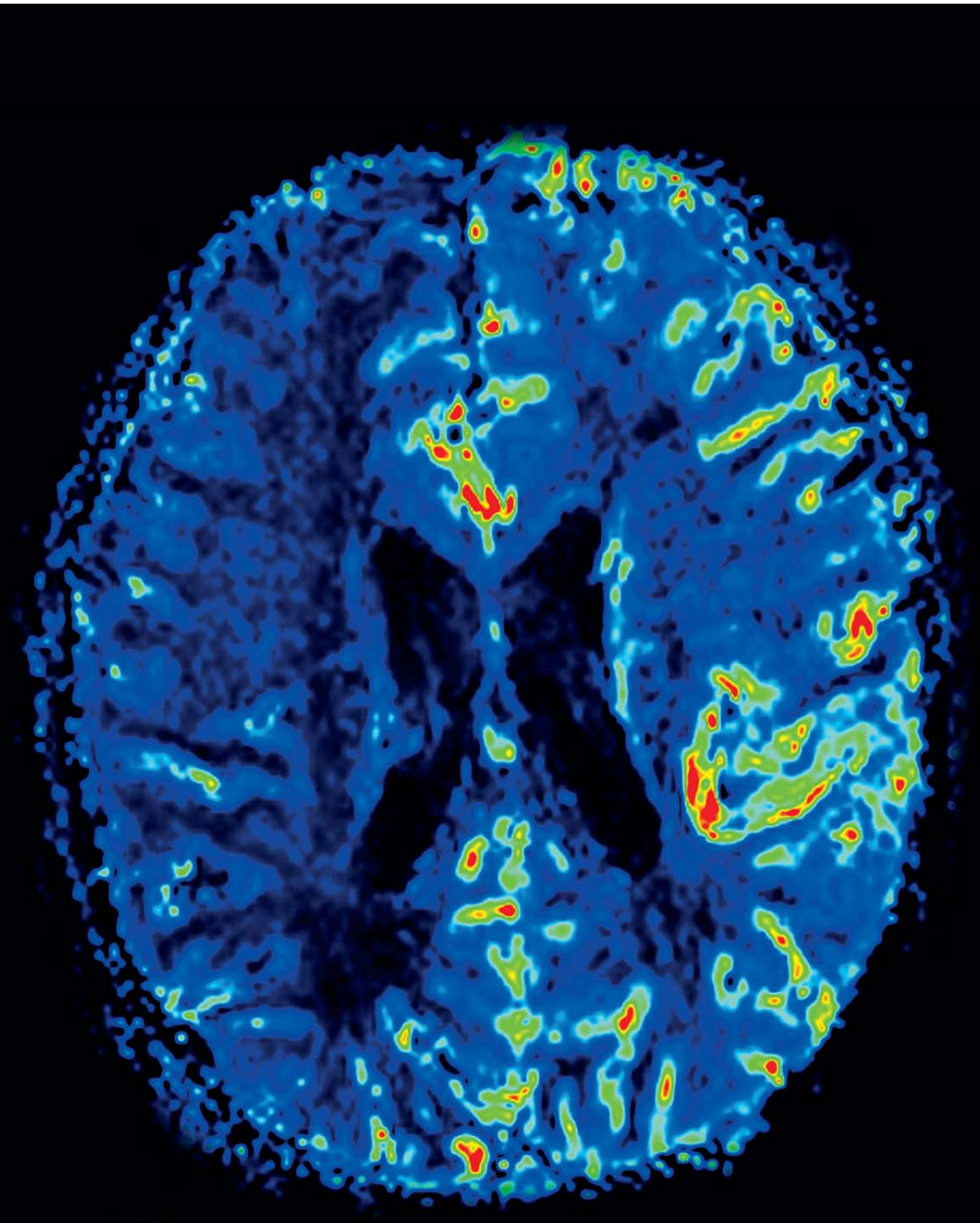

syngo ASL: Perfusion MR **without** IV contrast media

Dear MAGNETOM user,

Arterial Spin Labeling (ASL) is unique. It is the only **noninvasive MR imaging** technique which allows one to study the regional cerebral blood flow (rCBF).

Siemens MAGNETOM systems are unique. They are the first to provide robust PASL (Pulsed ASL) sequences as a product for MR users.

ASL may revolutionize the imaging approach when it comes to perfusion evaluation of tumors in the brain, acute stroke, obstructive carotid artery disease, epilepsy, dementia and many other diseases.

This special issue reveals the first examples from our worldwide research collaboration partners. We hope you will appreciate the benefits of this application and share our view that the usefulness of rCBF measurements will be enhanced by this noninvasive approach.

Enjoy reading the Flash.

Ali Nejat Bengi, M.D.

MAGNETOM Flash is part of Life, Siemens' unique customer care solution that helps you get the most from your investment. With its programs and services Life sharpens your skills so you can see optimal clinical value. It provides the support you need to maximize productivity and it assures that as technology changes, you will always be at the cutting edge.

The Editorial Team

We appreciate your comments.
Please contact us at magnetomworld.med@siemens.com

A. Nejat Bengi, M.D.
Editor in Chief

Antje Hellwich
Associate Editor

Dagmar Thomsik-Schröpfer, Ph.D., MR Marketing-Products, Erlangen, Germany

Ignacio Vallines, Ph.D., Applications Manager, Erlangen, Germany

Heike Weh,
Clinical Data Manager,
Erlangen, Germany

Bernhard Baden,
Clinical Data Manager,
Erlangen, Germany

Peter Kreisler, Ph.D.
Collaborations & Applications,
Erlangen, Germany

Milind Dhamankar, M.D.
Sr. Director, MR Product Marketing, Malvern, USA

Kathleen Giannini,
US Installed Base Manager,
Malvern, PA, USA

Michelle Kessler, US
Installed Base Manager,
Malvern, PA, USA

Gary R. McNeal, MS (BME)
Advanced Application Specialist,
Cardiovascular MR Imaging
Hoffman Estates, USA

Dr. Sunil Kumar S.L.
Senior Manager Applications,
Canada

Content

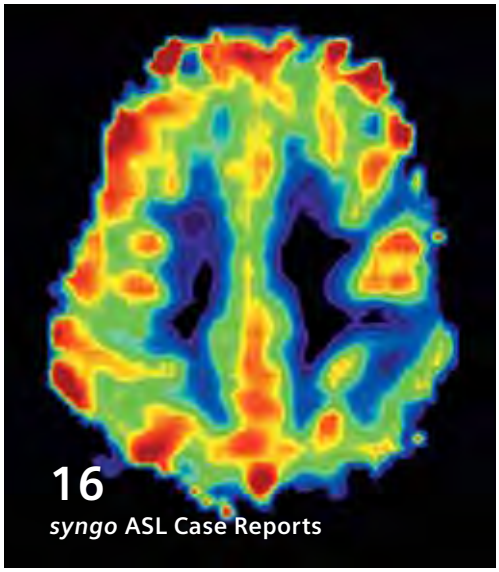

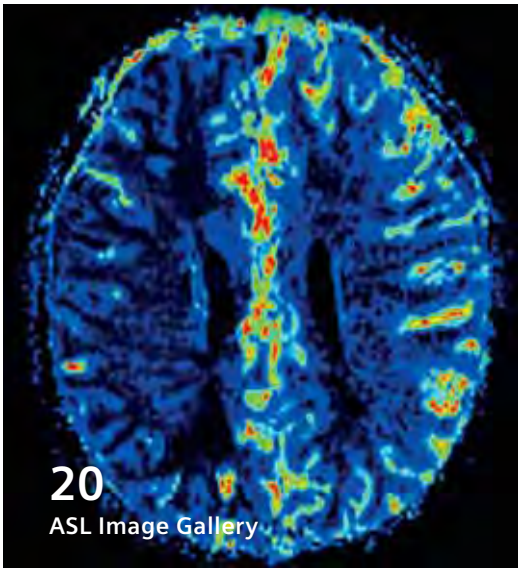

syngo ASL

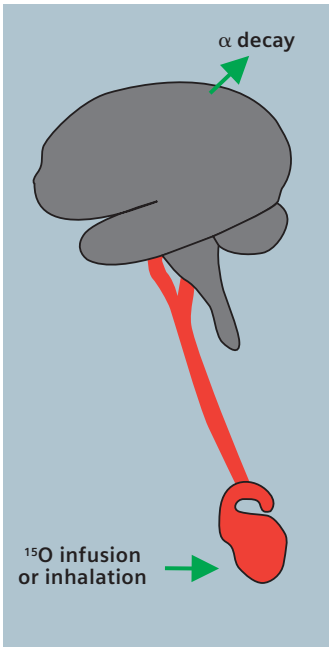

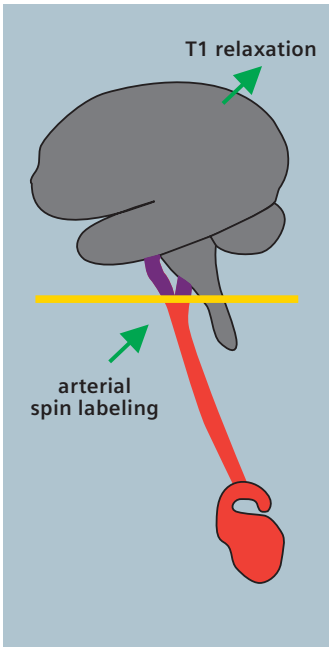

Arterial Spin Labeling (ASL) is using the water in arterial blood as an endogenous contrast agent to evaluate perfusion non-invasively.

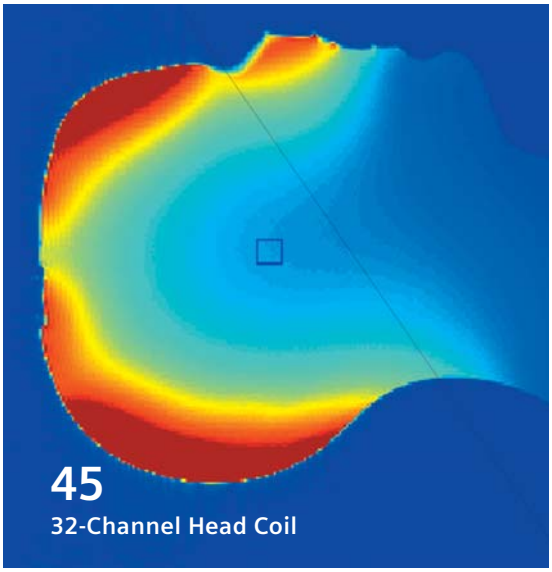

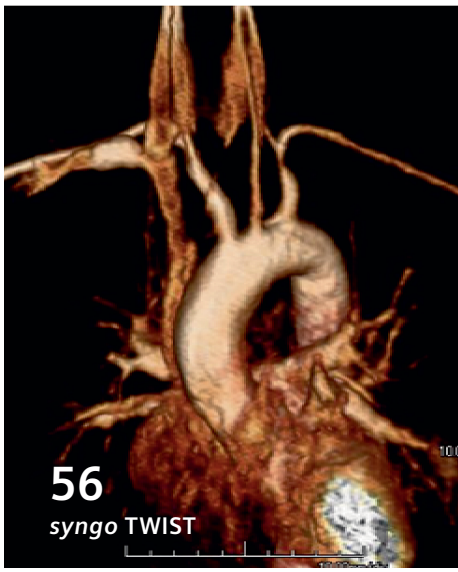

Clinical Neurology

Technology

Product News

Clinical Interventional

Clinical Cardiovascular

Arterial Spin Labeled Perfusion MRI

John A. Detre, M.D.

Center for Functional Neuroimaging, Department of Neurology and Radiology, University of Pennsylvania, Philadelphia, PA, USA

Perfusion refers to the delivery of oxygen and nutrients to tissues by means of blood flow and is one of the most fundamental physiological parameters. Disorders of perfusion also account for most of the leading causes of medical disability and mortality. While measurements of perfusion are of direct diagnostic value in vascular disorders, perfusion measurements also serve as biomarkers for a broader range of physiological and pathophysiological functions. A close coupling between cerebral blood flow and metabolism allows regional brain function to be assessed through measurements of cerebral perfusion and increased vascularity of neoplasms allows tumor perfusion to be used as a measure of tumor grade and to monitor the response to tumor therapy.

Classical tissue perfusion is measured using a diffusible tracer that can exchange between the vascular compartment and tissue. This yields a perfusion measurement in units of milliliters of blood flow per gram of tissue per unit time (ml/g/min). However, owing to the relative ease of inferring hemodynamic function from the passage of an intravascular tracer, the term "perfusion imaging" has also been applied to measurements of perfusion-related parameters such as mean transit time and blood volume that can be related to perfusion through the Central Volume Principle. In the field of MRI, most people associate the concept of perfusion imaging with dynamic susceptibility contrast imaging using a relaxation contrast agent. However, there are also several methods for the measurement of classical tissue perfusion using MRI. Diffusible tracers that can be monitored with MRI include fluorinated halocarbons [1], deuterated water ($^{2}H2O$) [2, 3], ^{17}O-water [4], and potentially ^{13}C labeled hydrocarbons.

Magnetically labeled endogenous blood water can also be used as a tracer for perfusion MRI. To accomplish this, the longitudinal magnetization of arterial blood water must be manipulated so that it differs from the tissue magnetization. It is quite analogous to the use of 15O-water for PET perfusion imaging except that the magnetic tracer decays with T1 instead of a radioactive decay and the ASL

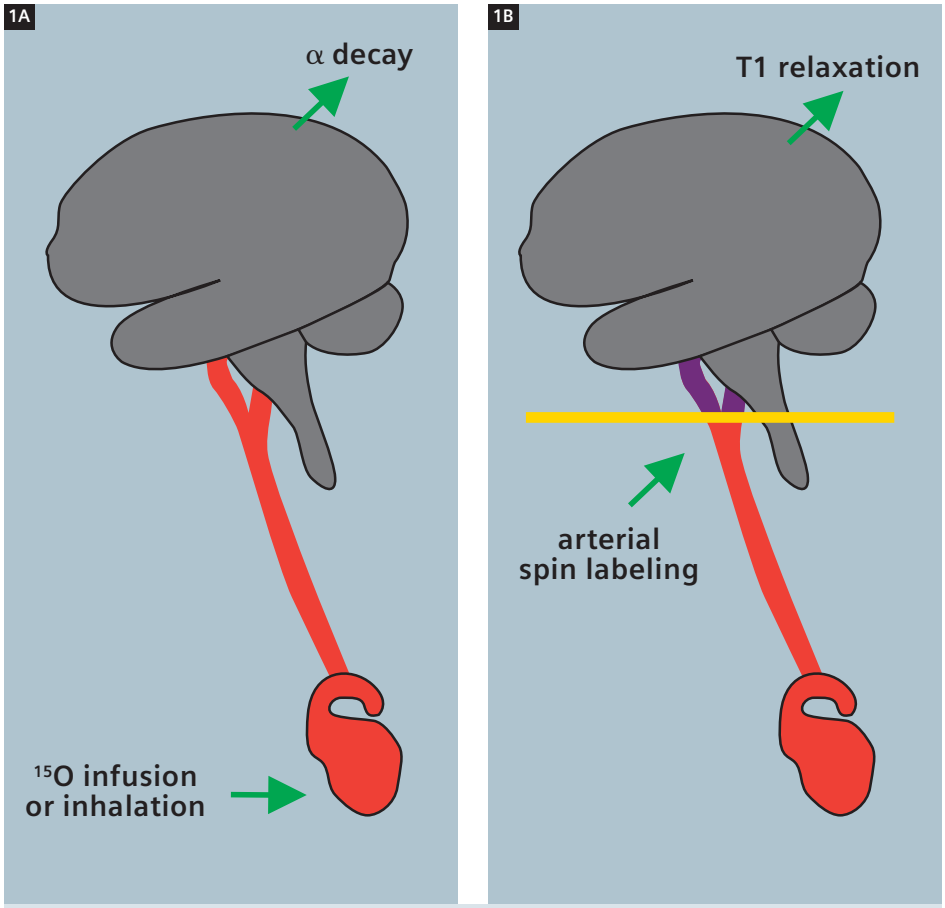

1 Concept of Arterial Spin Labeling (ASL), comparing 15O-PET (Fig. 1A)) and ASL (Fig. 1B) approaches. In ASL, endogenous arterial blood water is magnetically labeled instead of exogenously administered tracer, and the magnetic label decays with T1 instead of radioactive decay (α).

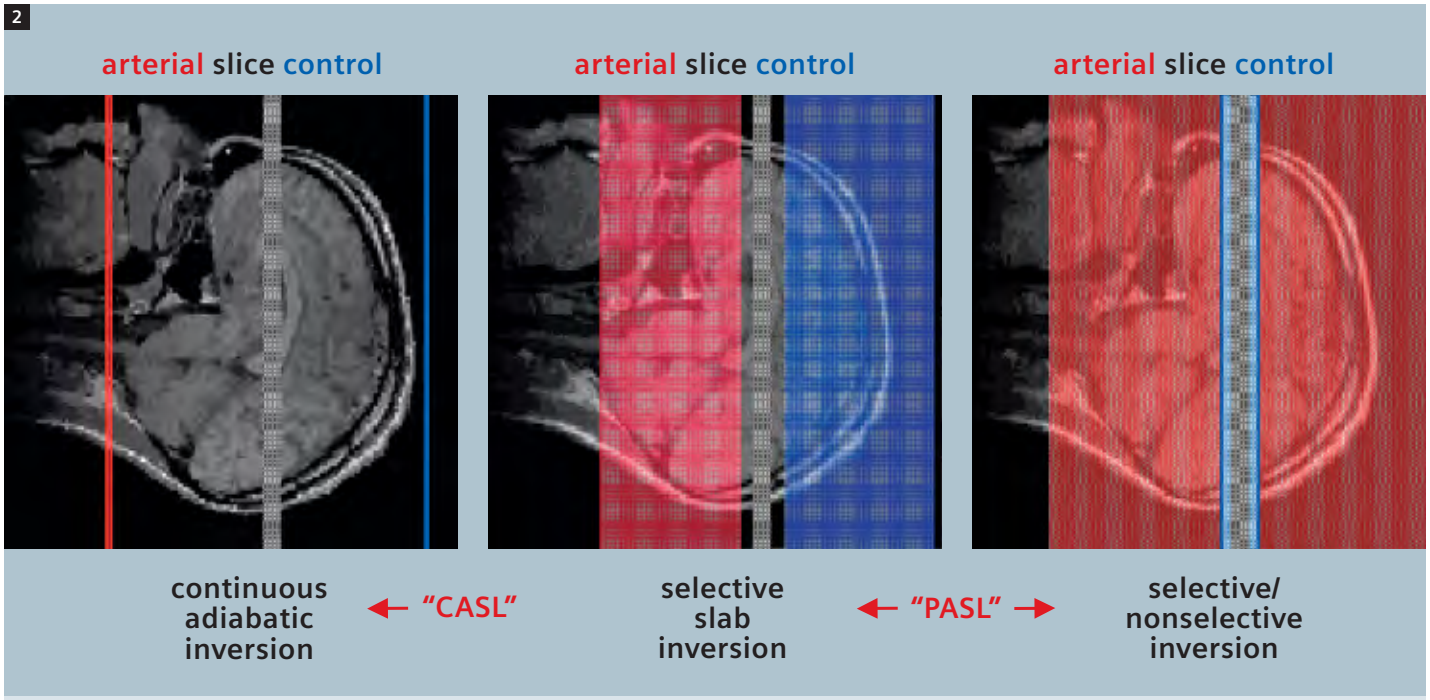

2 Schematic diagram illustrating arterial spin labeling strategies. Continuous ASL (CASL, left) labels arterial spins as they flow through a labeling plane. Pulsed ASL (PASL, middle and right) labels arterial spins using a spatially selective labeling pulse. Applications to single-slice imaging are illustrated for simplicity. Somewhat more complex schemes are used for multislice imaging.

approach is completely noninvasive. Because T1 relaxation is approximately 100 times faster than the radioactive decay rate of 15O, only a small amount of labeled water accumulates, though the temporal resolution is also correspondingly higher. The subtle difference between images acquired with and without arterial spin labeling (ASL) can be modeled to derive a calculated blood flow image showing perfusion in ml/g/min at each voxel. Key parameters required for ASL quantification include knowledge or assumptions about the T1 values in blood and tissue, the labeling efficiency, and the arterial transit time [5, 6]. ASL can be combined with any imaging sequence and theoretically provides a flow image that is completely independent of scanning parameters; As such, it represents one of the few MRI contrast mechanisms for which the physiological basis is really well understood. In practice, most ASL measurements are made with some compromises trading off sensitivity and convenience for a less pure measurement of tissue blood flow.

Arterial spin labeling can be accomplished using a variety of approaches and in nearly any organ. Most ASL has been carried out in the brain because the arterial supply is extremely well defined and perfusion to brain tissue is high. However, ASL studies have also successfully been carried out in kidney, lung, retina, heart, and skeletal muscle. The most common ASL approaches use either pulsed labeling (PASL) with an instantaneous spatially selective saturation or inversion pulse [7], or continuous labeling (CASL), most typically by flow driven adiabatic fast passage [8]. In some PASL methods, a spatially selective inversion pulse is administered to the tissue rather than to arterial blood [9]. More recently there have also been efforts label based on velocity rather than spatial selectivity for tissue arterial supply [10]. The first publication on ASL perfusion MRI actually used pseudocontinuous saturation to dephase arterial blood water in the neck of a rat [11]. Prior to that time, the idea of labeling arterial blood water had been considered primarily as a means for visualizing intraluminal flow in arteries and veins [12, 13]. Continuous labeling schemes allow brain magnetization to reach a steady-state that maximizes the signal difference between labeled and unlabeled conditions [14], though this occurs at the expense of both increased SAR deposition and magnetization transfer effects that complicate both the accurate measurement of the control (unlabeled) condition, and the extension to multislice imaging. Some groups have addressed this using a separate labeling coil [15], while others have pursued single coil approaches [16]. The myriad technical details of ASL implementation are beyond the scope of this article, but key advances have focused on improved labeling, improved measurements of the subtle effects of ASL on tissue signal, and improved modeling of measured signal changes in terms of tissue blood flow. For CBF, current tech-

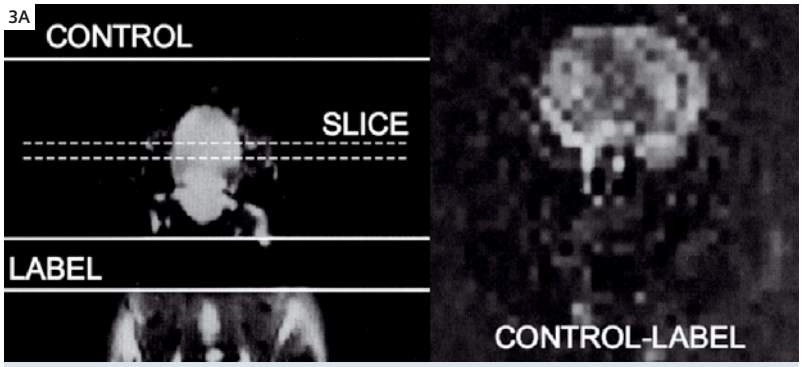

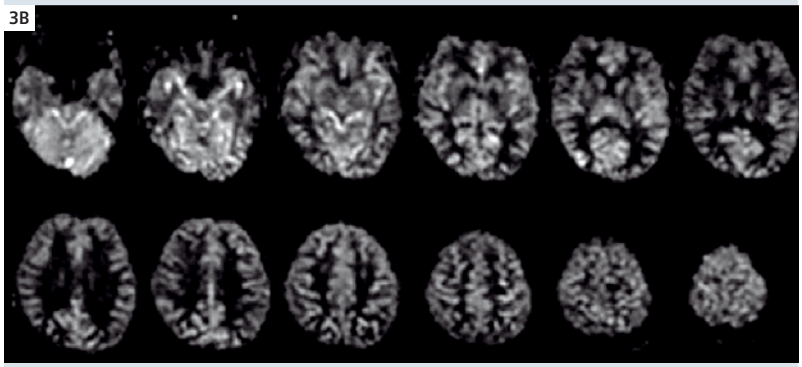

3 The original demonstration of ASL using pseudocontinuous ASL in the rat brain [11]. **(Fig. 3A)**
Multislice PASL of human brain acquired from a normal volunteer at 3T [18]. **(Fig. 3B)**

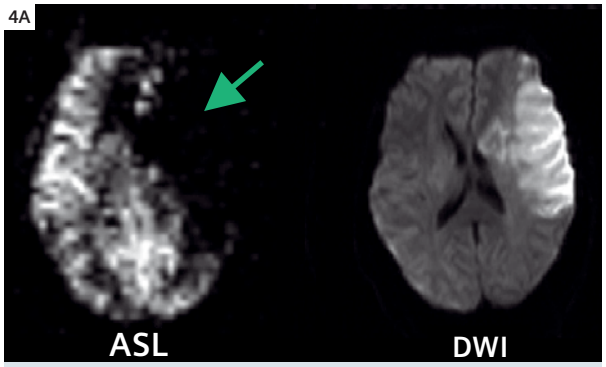

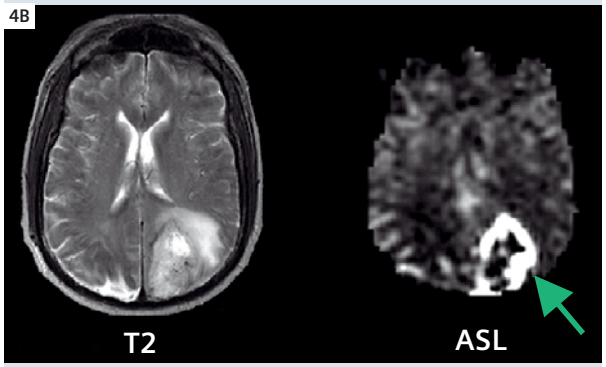

4 Representative clinical applications of ASL showing hypoperfusion in an acute stroke **(Fig. 4A)** and hyperperfusion in a glioblastoma **(Fig. 4B)**. For more details on clinical applications of ASL see [31].

nology provides a reasonably good whole-brain image in just a few minutes of scanning. ASL methods particularly benefit from high magnetic field trengths because not only is the sensitivity higher, but T1 also lengthens, allowing more label to accumulate [17, 18]. ASL methods also benefit from the increased sensitivity provided by multicoil receivers and are minimally degraded by parallel imaging [19]. The use of a body transmitter benefits PASL by allowing a larger region for arterial inversion but necessitates a more elaborate approach for CASL, termed pseudo-continuous labeling [20].

In clinical neuroscience, while the application of ASL perfusion MRI to the diagnosis and management of acute stroke is both obvious and feasible, the clinical utility of ASL is likely much broader since only a minority of acute stroke patients undergo MRI. ASL perfusion MRI could greatly enhance the evaluation of both TIA (Transient Ischemic Attack) and chronic cerebrovascular disease by quantifying regional CBF in specific vascular territories where interventions may be planned, or by allowing the effects of pharmacological therapies on CBF to be evaluated. Several approaches now also exist for selective arterial labeling, allowing the perfusion distribution of specific arteries to be assessed independently [21, 22]. A challenge in the application of ASL to cerebrovascular disorders is that sensitivity decreases in regions with very low CBF and the presence of prolonged arterial transit times that can create regions of apparent hyperperfusion when labeled spins remain in large vessels due to prolonged arterial transit times. This artifact is usually easy to recognize and can be verified by the addition of spoiler gradients that dephase coherently flowing spins. Arterial transit times can even be quantified by comparing ASL images with and without spoiler gradients [23], providing access to a novel physiological parameter that likely reflects the recruitment collateral flow sources. Another significant application of ASL is in degenerative diseases, where specific patterns of hypoperfusion may be used to aid in differential diagnosis of disorders such as Alzheimer's disease [24] and frontotemporal dementia [25]. Finally, as noted above, perfusion of brain tumors typically correlates with their grade and potentially their response to therapies [26]. Undoubtedly, the clinical availability of noninvasive and quantitative CBF imaging will lead to numerous additional applications as further experience with this modality develops.

In basic neuroscience, ASL perfusion MRI can be used to localize task activation in a manner similar to BOLD fMRI (Blood Oxygen Level Dependent functional MR Imaging). Indeed, ASL based contrast derived from inversion recovery imaging of task activation was included in one of the earliest reports of fMRI in human brain [28]. Although relative CBF can be inferred from ASL images acquired without control labeling, acquisition of both labeled and control pairs are required for quantification of CBF. While this reduces the temporal resolution of ASL perfusion fMRI as compared to BOLD fMRI, it also

dramatically changes the noise properties of the data, providing sensitivity over much longer timescales [29]. ASL perfusion fMRI can also be used as a measure of brain function at rest, independent of any sensorimotor or cognitive task, and reveals regional changes in brain function associated with development [30], behavioral states [31], or genetic traits [32]. Because ASL measures a purely biological parameter, it should also be particularly valuable for multisite studies examining brain function on a variety of scanner platforms or longitudinally.

A limitation in the widespread use and dissemination of ASL perfusion MRI has been the absence of product sequences provided by vendors. The recent development of an ASL product by Siemens should help alleviate this limitation, at least for Siemens users. Other vendors will hopefully follow suit. The Siemens ASL product provides a robust PASL sequence with echoplanar readout and online calculation of CBF maps from the acquired data. Many of us involved in the early development and validation of ASL perfusion MRI are eager to see it translated to routine clinical use.

Dr. Detre is an inventor of ASL technology and has received royalties from the University of Pennsylvania for its licensure.

References

1 Eleff, S.M., M.D. Schnall, L. Ligetti, M. Osbakken, V.H. Subramanian, B. Chance and J.S.J. Leigh, Concurrent measurement of cerebral blood flow, sodium, lactate, and high-energy phosphate metabolism using 19F, 23Na, 1H, and 31P nuclear magnetic resonance spectroscopy. Magn. Reson. Med., 1988. 7: p. 412-24.

2 Ackerman, J.J., C.S. Ewy, N.N. Becker and R.A. Shalwitz, Deuterium nuclear magnetic resonance measurements of blood flow and tissue perfusion employing 2H2O as a freely diffusible tracer. Proc Natl Acad Sci U S A, 1987. 84(12): p. 4099-102.

3 Detre, J.A., V.H. Subramanian, M.D. Mitchell, D.S. Smith, A. Kobayashi, A. Zaman and J.S. Leigh, Measurement of regional cerebral blood flow in cat brain using intracarotid 2H2O and 2H NMR imaging. Magn. Reson. Med., 1990. 14: p. 389-395.

4 Pekar, J., L. Ligeti, Z. Ruttner, R.C. Lyon, T.M. Sinnwell, P. van Gelderen, D. Fiat, C.T. Moonen and A.C. McLaughlin, In vivo measurement of cerebral oxygen consumption and blood flow using 17O magnetic resonance imaging. Magn Reson Med, 1991. 21(2): p. 313-9.

5 Alsop, D.C. and J.A. Detre, Reduced transit-time sensitivity in noninvasive magnetic resonance imaging of human cerebral blood flow. J. Cereb. Blood Flow Metab., 1996. 16: p. 1236-1249.

6 Buxton, R.B., L.R. Frank, E.C. Wong, B. Siewert, S. Warach and R.R. Edelman, A general kinetic model for quantitative perfusion imaging with arterial spin labeling. Magn Reson Med, 1998. 40(3): p. 383-96.

7 Wong, E.C., R.B. Buxton and L.R. Frank, Implementation of quantitative perfusion imaging techniques for functional brain mapping using pulsed arterial spin labeling. NMR Biomed, 1997. 10(4-5): p. 237-49.

8 Williams, D.S., J.A. Detre, J.S. Leigh and A.P. Koretsky, Magnetic resonance imaging of perfusion using spin inversion of arterial water. Proc. Natl. Acad. Sci. USA, 1992. 89: p. 212-216.

9 Kim, S.G., Quantification of relative cerebral blood flow change by flow-sensitive alternating inversion recovery (FAIR) technique: application to functional mapping. Magn. Reson. Med., 1995. 34: p. 293-301.

10 Wong, E.C., M. Cronin, W.C. Wu, B. Inglis, L.R. Frank and T.T. Liu, Velocity-selective arterial spin labeling. Magn Reson Med, 2006. 55(6): p. 1334-41.

11 Detre, J.A., J.S. Leigh, D.S. Williams and A.P. Koretsky, Perfusion imaging. Magn. Reson. Med., 1992. 23: p. 37-45.

12 Sardashti, M., D.G. Schwartzberg, G.P. Stomp and W.T. Dixon, Spin labeling angiography of the carotids by presaturation and simplified adiabatic inversion. Magn. Reson. Med., 1990. 15: p. 192-200.

13 Singer, J.R. and L.E. Crooks, Nuclear magnetic resonance blood flow measurements in the human brain. Science, 1983. 221(4611): p. 654-6.

14 Wong, E.C., R.B. Buxton and L.R. Frank, A theoretical and experimental comparison of continuous and pulsed arterial spin labeling techniques for quantitative perfusion imaging. Magn Reson Med, 1998. 40(3): p. 348-55.

15 Zaharchuk, G., P.J. Ledden, K.K. Kwong, T.G. Reese, B.R. Rosen and L.L. Wald, Multislice perfusion and perfusion territory imaging in humans with separate label and image coils. Magn. Reson. Med., 1999. 41: p. 1093-8.

16 Alsop, D.C. and J.A. Detre, Multisection cerebral blood flow MR imaging with continuous arterial spin labeling. Radiology, 1998. 208: p. 410-16.

17 Wang, J., D.C. Alsop, L. Li, J. Listerud, J.B. Gonzalez-At, M.D. Schnall and J.A. Detre, Comparison of quantitative perfusion imaging using arterial spin labeling at 1.5 and 4.0 Tesla. Magn Reson Med, 2002. 48(2): p. 242-54.

18 Wang, J., Y. Zhang, R.L. Wolf, A.C. Roc, D.C. Alsop and J.A. Detre, Amplitude-modulated Continuous Arterial Spin-labeling 3.0-T Perfusion MR Imaging with a Single Coil: Feasibility Study. Radiology, 2005. 235: p. 218-28.

19 Wang, Z., J. Wang, T.J. Connick, G.S. Wetmore and J.A. Detre, Continuous ASL perfusion MRI with an array coil and parallel imaging at 3T. Magn Reson Med, 2005. 54(3): p. 732-7.

20 Garcia, D.M., C. de Bazelaire and D. Alsop, Pseudo-continuous Flow Driven Adiabatic Inversion for Arterial Spin Labeling. ISMRM 13th Scientific Meeting Proceedings, 2005: p. 37.

21 Hendrikse, J., J. van der Grond, H. Lu, P.C. van Zijl and X. Golay, Flow territory mapping of the cerebral arteries with regional perfusion MRI. Stroke, 2004. 35(4): p. 882-7.

22 Werner, R., K. Alfke, T. Schaeffter, A. Nabavi, H.M. Mehdorn and O. Jansen, Brain perfusion territory imaging applying oblique-plane arterial spin labeling with a standard send/receive head coil. Magn Reson Med, 2004. 52(6): p. 1443-7.

23 Wang, J., D.C. Alsop, H.K. Song, J.A. Maldjian, K. Tang, A.E. Salvucci and J.A. Detre, Arterial transit time imaging with flow encoding arterial spin tagging (FEAST). Magn Reson Med, 2003. 50(3): p. 599-607.

24 Alsop, D.C., J.A. Detre and M. Grossman, Assessment of cerebral blood flow in Alzheimer's disease by spin-labeled magnetic resonance imaging. Ann Neurol, 2000. 47(1): p. 93-100.

25 Du, A.T., G.H. Jahng, S. Hayasaka, J.H. Kramer, H.J. Rosen, M.L. Gorno-Tempini, K.P. Rankin, B.L. Miller, M.W. Weiner and N. Schuff, Hypoperfusion in frontotemporal dementia and Alzheimer disease by arterial spin labeling MRI. Neurology, 2006. 67(7): p. 1215-20.

26 Wolf, R.L., J. Wang, S. Wang, E.R. Melhem, M. O'Rourke D, K.D. Judy and J.A. Detre, Grading of CNS neoplasms using continuous arterial spin labeled perfusion MR imaging at 3 Tesla. J Magn Reson Imaging, 2005. 22(4): p. 475-482.

27 Wolf, R.L. and J.A. Detre, Clinical neuroimaging using arterial spin-labeled perfusion magnetic resonance imaging. Neurotherapeutics, 2007. 4(3): p. 346-59.

28 Kwong, K.K., J.W. Belliveau, D.A. Chesler, I.E. Goldberg, R.M. Weisskoff, B.P. Poncelet, D.N. Kennedy, B.E. Hoppel, M.S. Cohen and R. Turner, Dynamic magnetic resonance imaging of human brain activity during primary sensory stimulation. Proc. Natl. Acad. Sci. USA, 1992. 89: p. 5675-5679.

29 Aguirre, G.K., J.A. Detre and D.C. Alsop, Experimental design and the relative sensitivity of BOLD and perfusion fMRI. Neuroimage, 2002. 15: p. 488-500.

30 Wang, Z., M. Fernandez-Seara, D.C. Alsop, W.C. Liu, J.F. Flax, A.A. Benasich and J.A. Detre, Assessment of functional development in normal infant brain using arterial spin labeled perfusion MRI. Neuroimage, 2008. 39(3): p. 973-8.

31 Wang, J., H. Rao, G.S. Wetmore, P.M. Furlan, M. Korczykowski, D.F. Dinges and J.A. Detre, Perfusion functional MRI reveals cerebral blood flow pattern under psychological stress. Proc Natl Acad Sci U S A, 2005. 102(49): p. 17804-9.

32 Rao, H., S.J. Gillihan, J. Wang, M. Korczykowski, G.M. Sankoorikal, K.A. Kaercher, E.S. Brodkin, J.A. Detre and M.J. Farah, Genetic variation in serotonin transporter alters resting brain function in healthy individuals. Biol Psychiatry, 2007. 62(6): p. 600-6.

Arterial Spin Labeling (*syngo* ASL) Case Reports from Geneva University

Viallon Magalie, Ph.D.; Karl-Olof Lovblad, M.D., Ph.D.

Hopitaux, Universitaire de Genève, Switzerland

Case 1: Pediatric 1

Patient history

15-year-old female patient with known epilepsy.

Image findings / Results

On the T2-weighted images there are multiple bilateral hemispheric cortical and subcortical hyperintensities that are much more visible on the corresponding FLAIR images. On the ASL perfusion maps we have hypoperfusion in these areas.

Discussion

The multiple cortical and subcortical lesions correspond to tubera in a case of Tuberous Sclerosis of Bourneville.

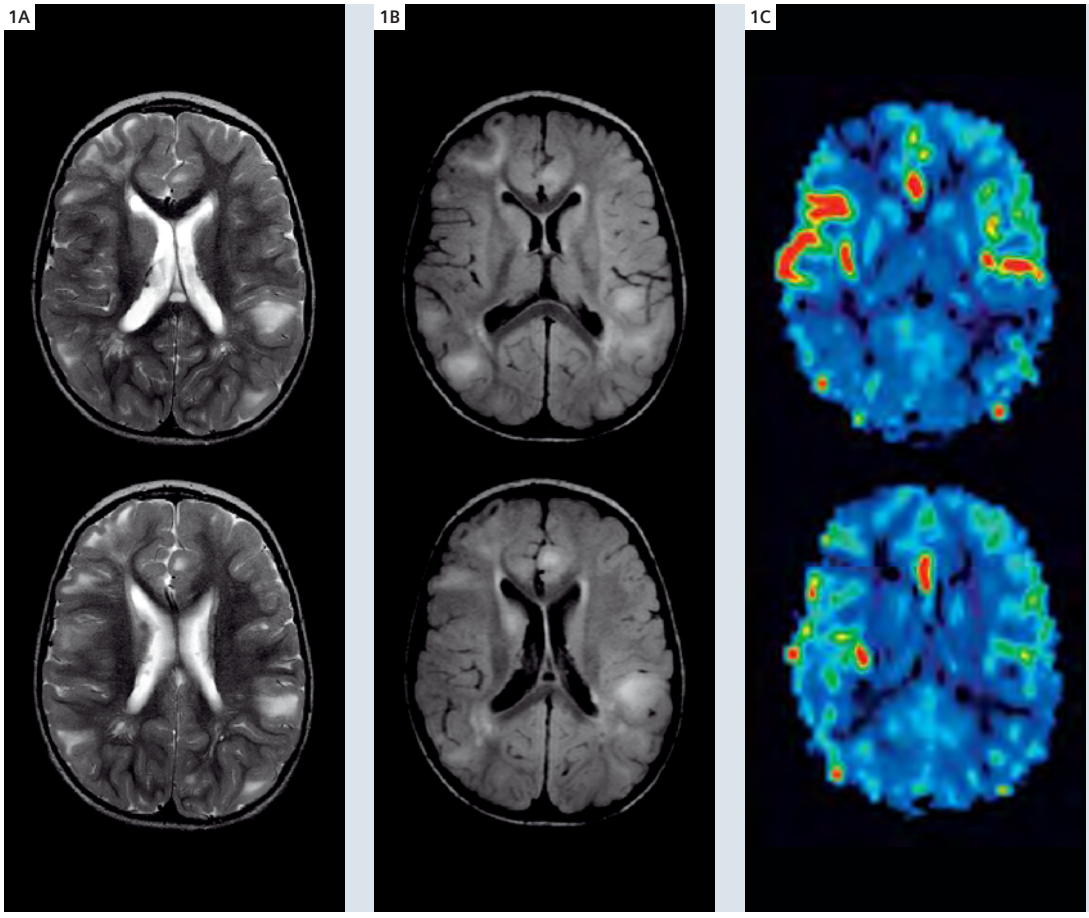

1A T2-weighted axial Turbo Spin Echo (TSE) image. Slice thickness 4 mm, TE/TR 101/4000 ms, BW 170 Hz/px, PAT factor 2, TF 19, FoV 150 x 200 mm, matrix 288 x 512, flip angle 145°.
1B Multiplanar reconstruction (MPR) Flair 3D sagittal 1 mm, TE/TR/TI 411/6000/2100 ms, BW 780 Hz/px, PAT factor 2, TF 266, FoV 234 x 250 mm, matrix 242 x 256, MPR slice thickness 4 mm, 176 slices.
1C Fair-QUIPSII arterial spin labeling sequence: TE/TR 13/5000 ms, BW 2230 Hz/px, matrix 64 x 64, FoV 220 mm, FatSat, slice thickness 6 mm, 14 slices, TI1 700 ms, TI2 1800 ms, T1 1496.5 ms, Partial Fourier 6/8, Lambda 0.9 mL/g, inversion efficiency 95%, flow compensation with flow limit 50 cm/sec, inferior Sat. Thk 100 mm, inferior sat gap 0 mm.

Case 2: Pediatric 2

Patient history

5-months-old* female with intractable epilepsy with 15 episodes per day.

*The safety of imaging infants under two years old has not been established.

Image findings / Results

Polymicrogyria of the left hemisphere on the T2-weighted images. On the ASL perfusion maps there is hypoperfusion in the left occipital lobe, which was also seen on FDG-PET (FluoroDeoxyGlucose-Positron Emission Tomography).

Discussion

Left-sided Hemimegalencephaly with polymicrogyria. The ASL data confirm the PET data which shows ictal hyperperfusion in the left occipital lobe.

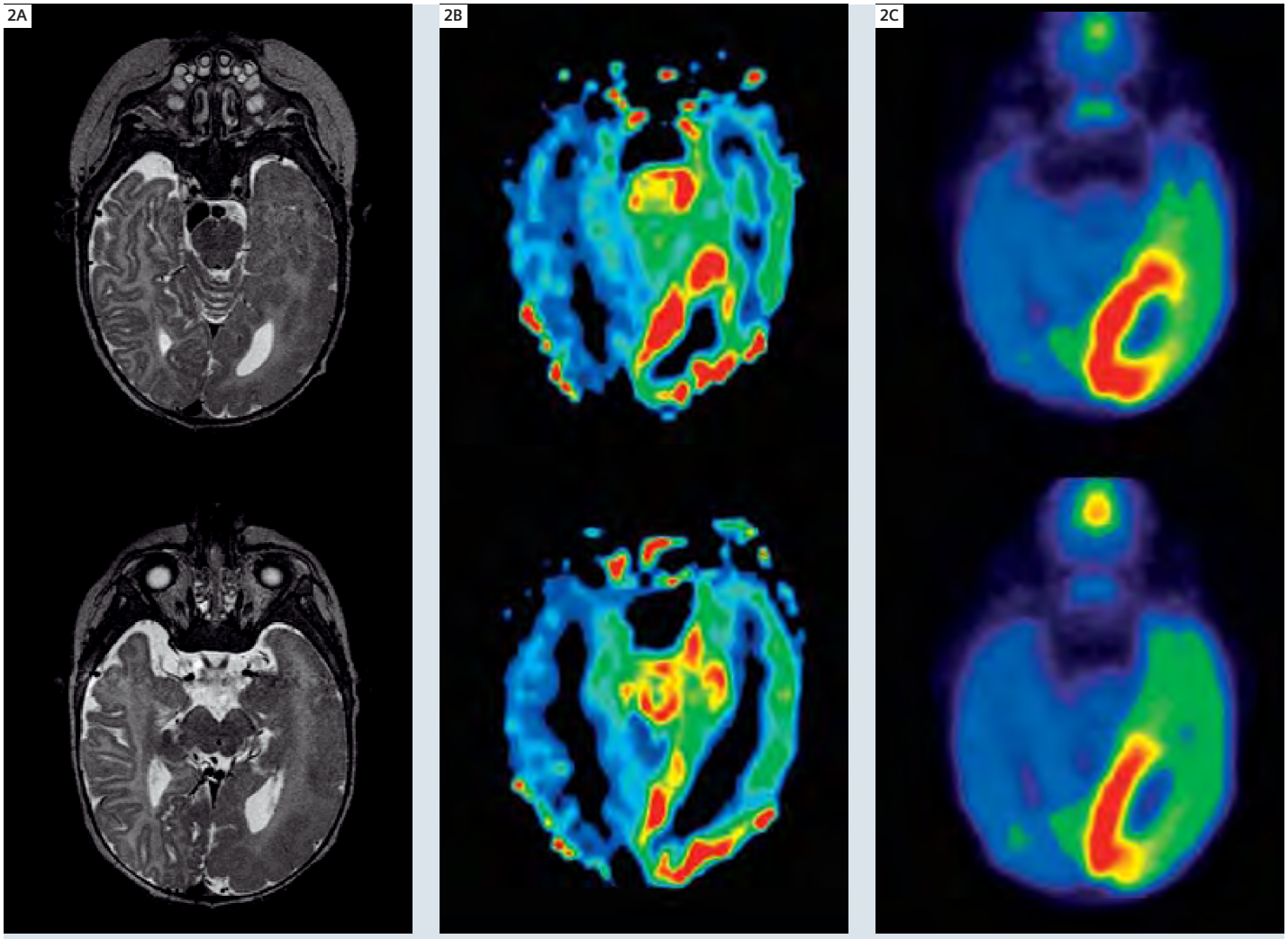

2A T2-weighted axial Turbo Spin Echo (TSE) image, slice thickness mm, TE/TR 101/4000 ms, BW 170 Hz/px, PAT factor 2, TF 19, FoV 150 x 200 mm, matrix 288 x 512, flip angle 145°. **2B** Fair-QUIPSII arterial spin labeling sequence: TE/TR 13/5000 ms, BW 2230 Hz/px, matrix 64 x 64, FoV 220 mm, FatSat, slice thickness 6 mm, 14 slices, TI1 700 ms, TI2 1800 ms, T1 1496.5, Partial Fourier 6/8, Lambda 0.9 mL/g, inversion efficiency 95%, flow compensation with flow limit 50 cm/sec, inferior Sat. Thk 100 mm, inferior sat gap 0 mm. **2C** F18-FDG PET-CT image with attenuation correction from CT data (Siemens Biograph Sensation 16), 80 MBq, 30 min post injection. These images show glucose metabolization which is linked to perfusion even though not being directly an image of CBF.

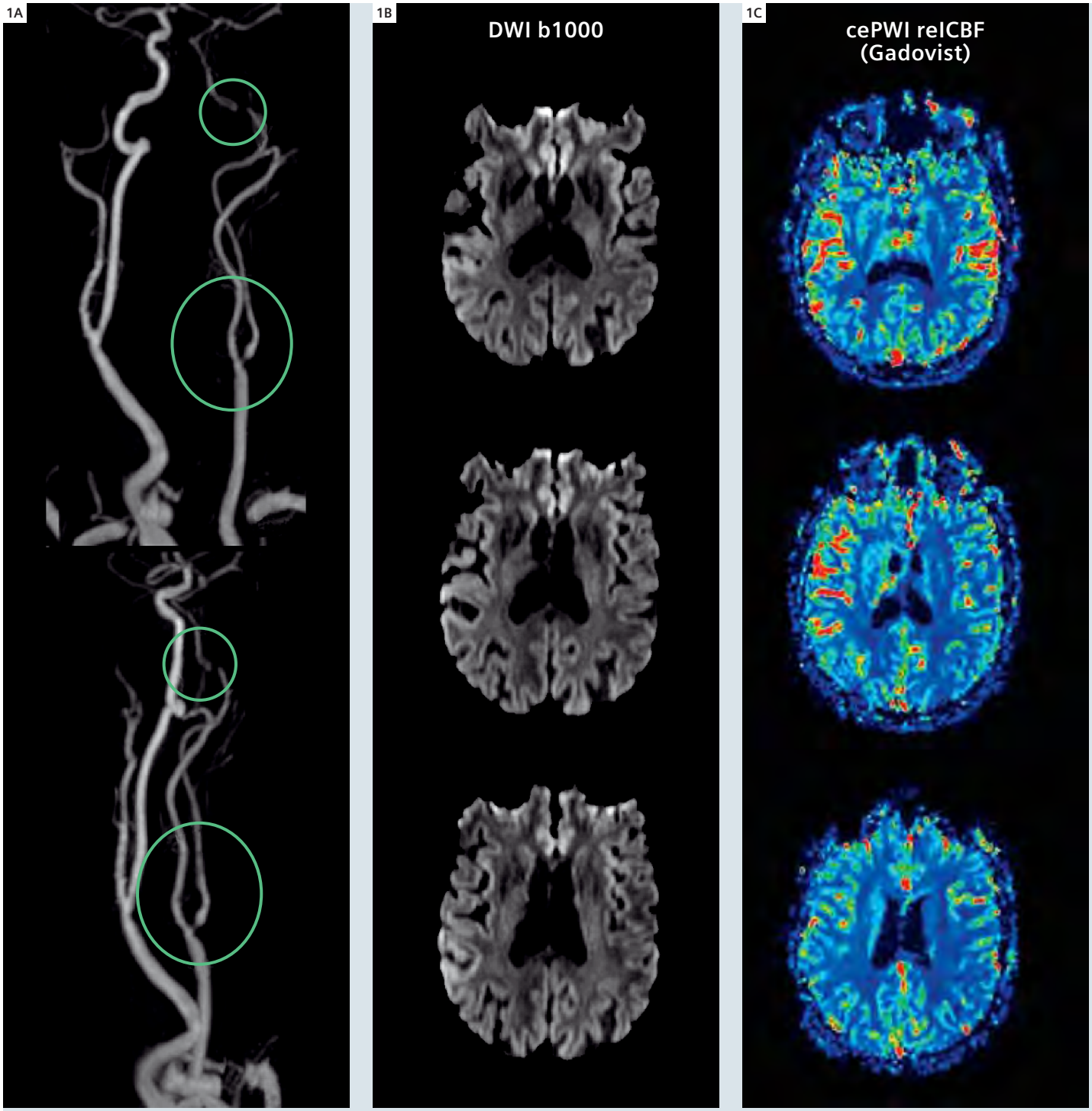

1A Contrast enhanced MR Angiography (ce-MRA): angiogram obtained from Flash3d-ce, voxel 0.8 x 0.8 x 0.8 mm, PAT factor 2, FoV= 263 x 300 mm, matrix 314 x 512, BW 650 Hz/px, flip angle 25°, 88 slices, centric reordering.

1B Diffusion-weighted imaging (DWI) b=1000, slice thickness 4 mm, TE/TR 92/5300 ms, BW 1240 Hz/px, PAT factor 2, FoV 208 x 230 mm, codage AP, matrix 157 x 192, flip angle 90°, 4 averages.

1C Contrast enhanced perfusion-weighed imaging (cePWI)*, relative cerebral blood flow (relCBF)*: relCBF parametric map calculated using *syngo* MR perfusion*, slice thickness 4 mm, TE/TR 92/4000 ms, BW 1370 Hz/px, PAT factor 2, FoV 200 x 200 mm, matrix 128 x 128, flip angle 90°.

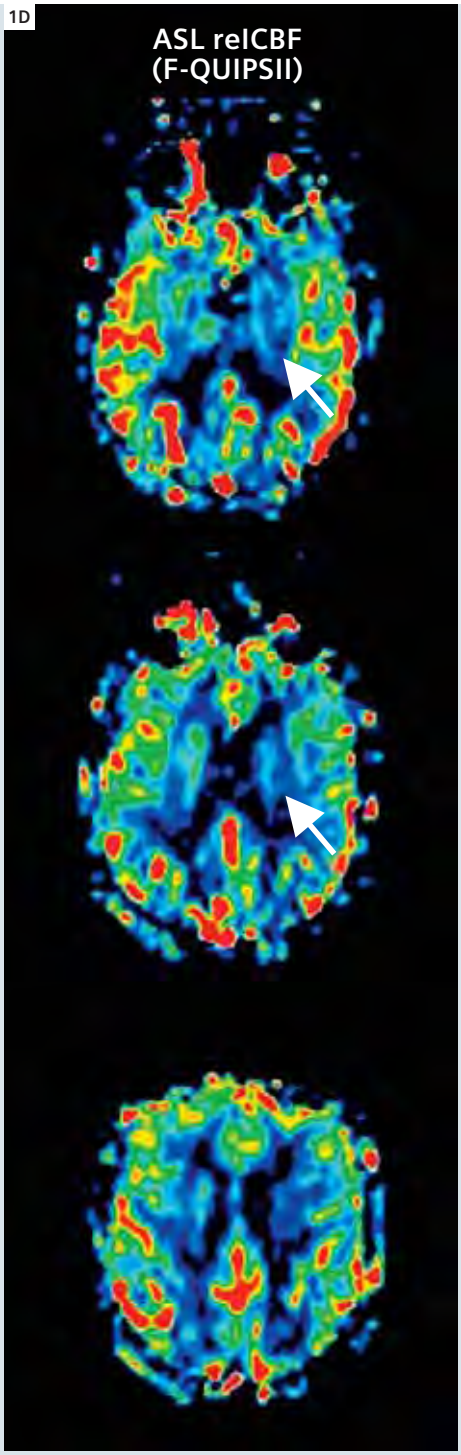

1D Arterial Spin Labeling (ASL) relCBF: Fair-QUIPSII ASL sequence: TE/TR 13/5000 ms, BW 2230 Hz/px, matrix 64 x 64, FoV 220 mm, FatSat, slice thickness 6 mm, 14 slices, TI1 700 ms, TI2 1800 ms, T1 1496.5 ms , Partial Fourier 6/8, Lambda 0.9 mL/g, inversion efficiency 95%, flow compensation with flow limit 50 cm/sec, inferior Sat. Thk 100 mm, inferior sat gap 0 mm.

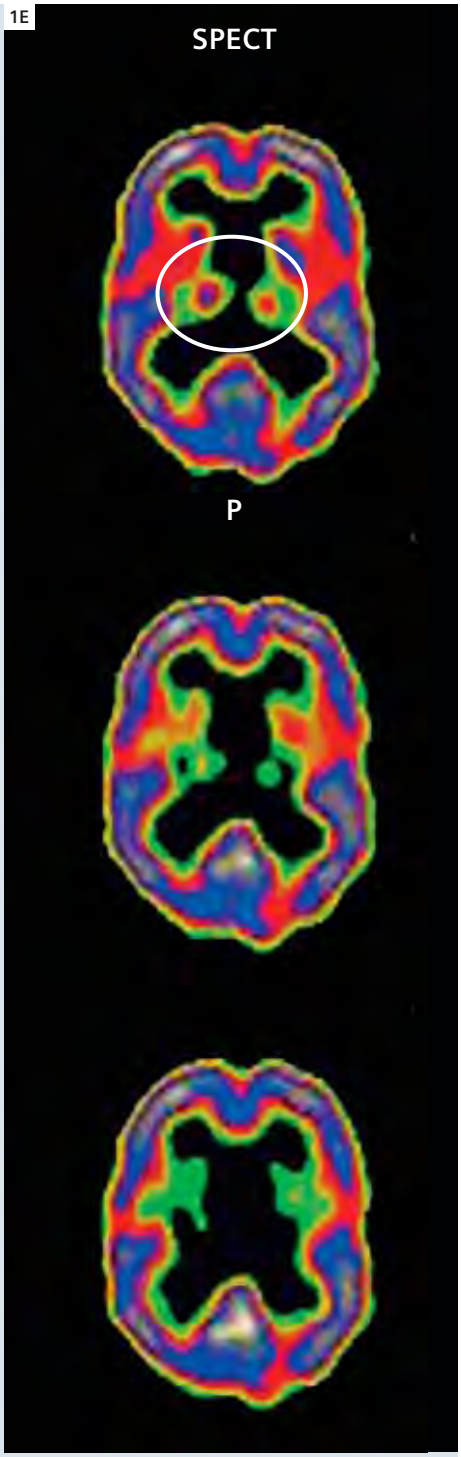

1E SPECT acquisition (Toshiba 3-heads) after injection of 369 MBq of 99 mTc-ECD. Post DIAMOX we observe an equalization of the perfusion of both hemisphere, pre DIAMOX, we have an increase perfusion on the right hemisphere.

Case 3: High grade stenosis on the left ICA

Patient history

Patient with left-sided carotid stenosis

Image findings / Results

High-grade left-sided carotid stenosis visible on contrast-enhanced MRA of the carotids. On DWI there are no ischemic lesions. On contrast-enhanced Perfusion* maps there is hypoperfusion in the left basal ganglia and internal capsule, which can be seen both on ASL maps and SPECT.

Discussion

The ASL findings correspond quite well to those identified on both SPECT and contrast-enhanced perfusion in a case of tight carotid stenosis. The enormous advantages of ASL in such a protocol is that it allows to both study perfusion prior to an injection of contrast agent dedicated to ceMRA.

Case 4: Stroke

Patient history

67-year-old male patient with dysphasia and right-sided hemiparesis.
The examination was performed on a MAGNETOM Trio, A Tim system, using a 12-channel head coil.

Image findings / Results

The DWI images show restricted diffusion in the left MCA territory, these changes can be seen on FLAIR and T2. On the ASL there is slight hyperperfusion* due to collateral flow, which cannot be seen on conventional contrast-enhanced perfusion imaging and SPECT images.

Discussion

In addition to the diffusion and standard MR sequences, ASL shows reperfusion in acute stroke* that cannot be seen on conventional MR perfusion images. Areas of cortical reperfusion due to collaterals were better assessed by ASL that seems to demonstrate hyperperfusion that might signal recanalization and/or collaterals. Moreover ASL correctly measures CBF even when BBB breaks down, which commonly occurs after a few days in stroke. Thus performing a protocol including ASL may allows one to better include/exclude patients for treatment: impacting on prevention by demonstrating hypoperfusion in carotid stenosis and improving treatment of ischemia by showing hemodynamic compromise.

The examinations were performed on a MAGNETOM Trio, using a 12-channel head coil.

Contact
Magalie Viallon, Ph.D.
Hopitaux Universitaire de Genève
Switzerland
Magalie.viallon@hcuge.ch

Karl-Olof Lovblad, M.D., Ph.D.
Hopitaux Universitaire de Genève
Switzerland
Karl-olof.lovblad@hcuge.ch

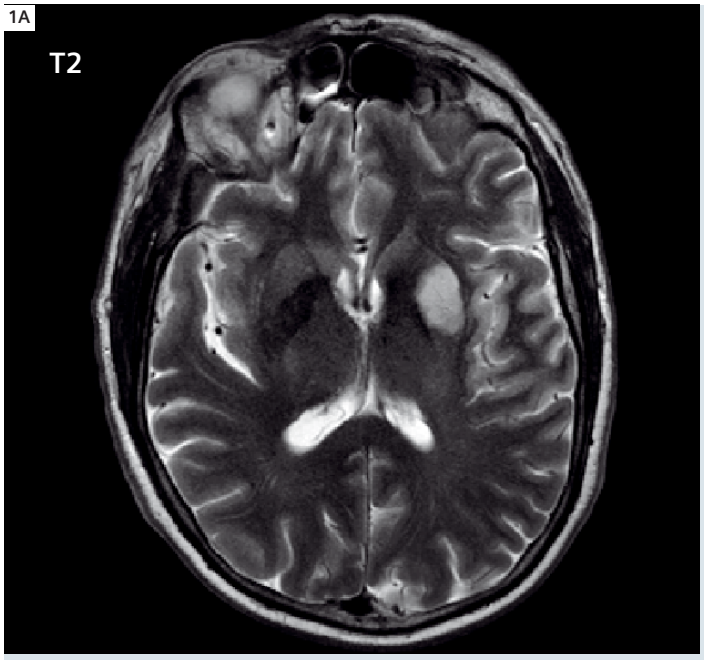

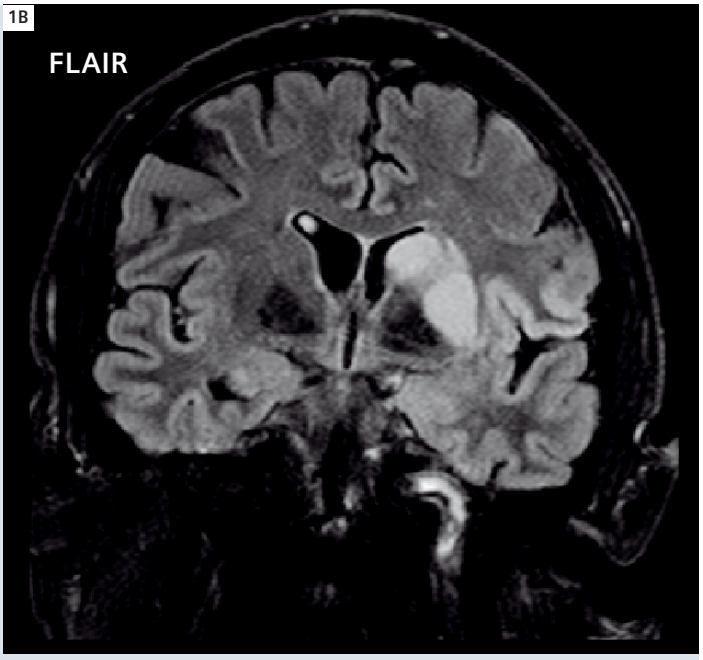

1A T2-weighted axial Turbo Spin Echo image: slice thickness 4 mm, TE/TR 101/4000 ms, BW 170 Hz/px, PAT factor 2, TF 19, FoV 150 x 200 mm, matrix 288 x 512, flip angle 145°. **1B** T2-weighted coronal FLAIR image: slice thickness 4 mm, TE/TR/TI 122/8500/2500 ms, BW 130 Hz/px, PAT factor 2, TF 13, FoV 200 x 230 mm, matrix 190 x 256, flip angle 150°.

*Works in progress (WIP). The information about this product is preliminary. The product is under development and not commercially available in the U.S., and its future availability cannot be ensured.

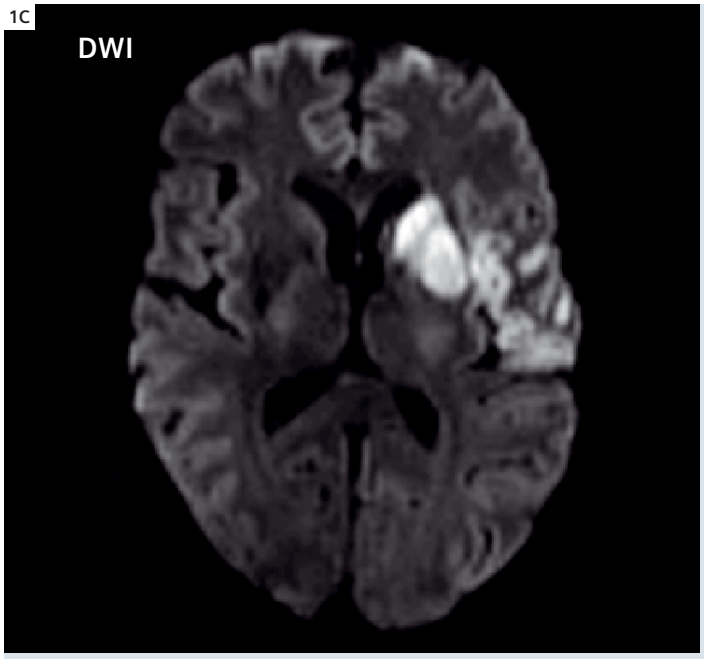

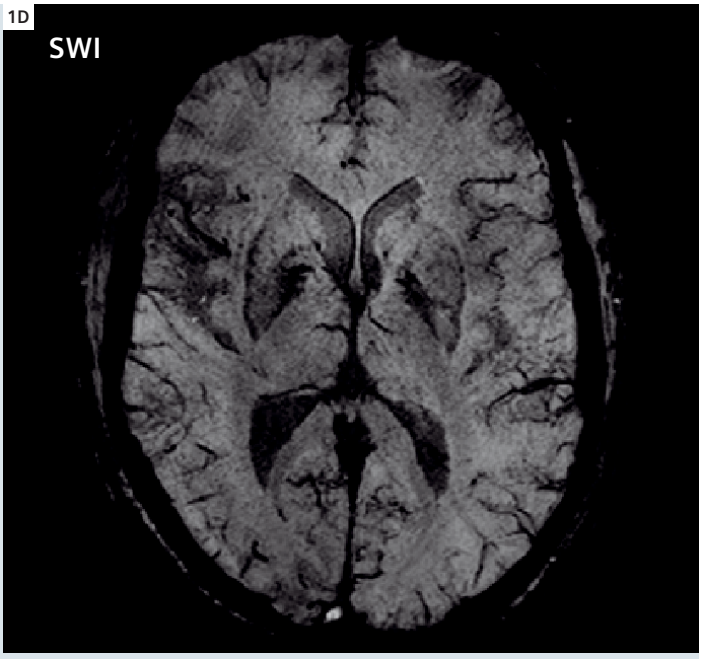

1C Diffusion-weighted image (DWI): b=1000, slice thickness 4 mm, TE/TR 92/5300 ms, BW 1240 Hz/px, PAT factor 2, FoV 208 x 230 mm, codage AP, matrix 157 x 192, flip angle 90°, 4 averages. **1D** Susceptibility-weighted image (SWI): slice thickness 1.2 mm, TE/TR 20/34 ms, BW 110 Hz/px, PAT factor 2, FoV 175 x 200 mm, matrix 224 x 256, flip angle 15°, flow compensation, thin MinIP (minimum intensity projection) axial 8 mm, 60 slices.

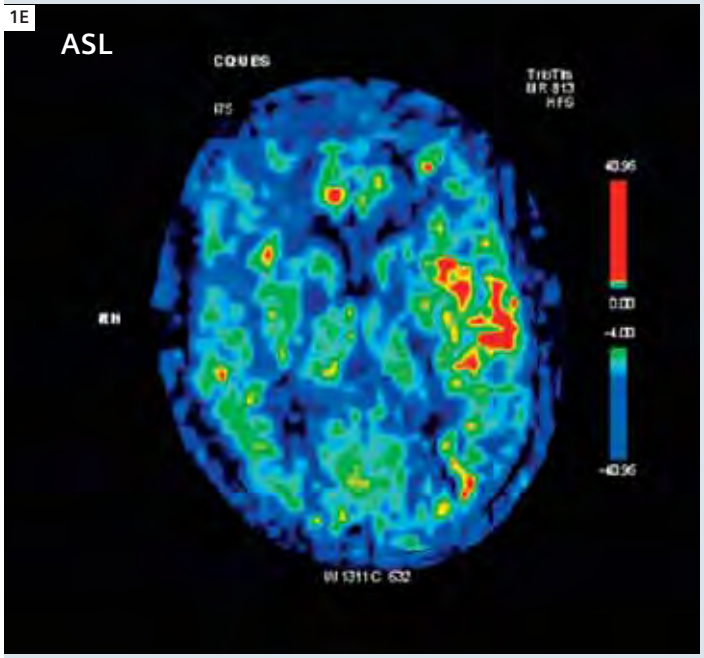

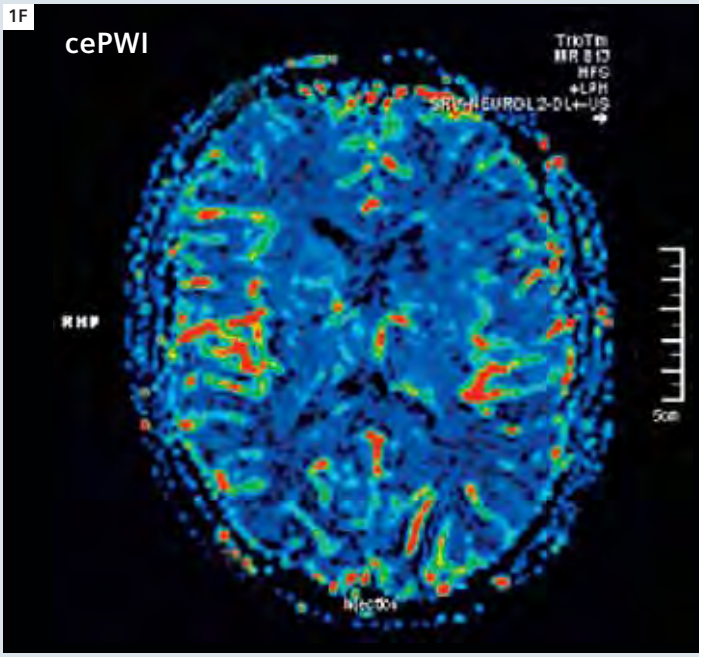

1E Arterial Spin Labeling (ASL) relCBF: Fair-QUIPSII arterial spin labeling sequence: TE/TR 13/5000 ms, BW 2230 Hz/px, matrix 64 x 64, FoV 220 mm, FatSat, slice thickness 6 mm, 14 slices, TI1 700 ms, TI2 1800 ms, T1 1496.5 ms, Partial Fourier 6/8, Lambda 0.9 mL/g, inversion efficiency 95%, flow compensation with flow limit 50 cm/s, inferior Sat. Thk 100 mm, inferior sat gap 0 mm.
1F Contrast enhanced perfustion-weighted image (cePWI)* relCBF: relCBF* parametric map calculated using *syngo* MR perfusion, slice thickness 4 mm, TE/TR 92/4000 ms, BW 1370 Hz/px, PAT factor 2, FoV 200 x 200 mm, matrix 128 x 128, flip angle 90°.

Arterial Spin Labeling (*syngo* ASL) Case Reports from Düsseldorf University

Hans-Jörg Wittsack, Ph.D.

University of Düsseldorf, Inst. of Diagnostic Radiology, Germany

Case 1
Patient history

Patient with metastasis of colon carcinoma.

Image findings / Results

PASL shows hypervascularization in the left parietal region confirming the diagnosis of metastasis.
PASL is helpful in differential diagnosis of metastasis.

The examinations were performed on a MAGNETOM Trio, A Tim system, using an 8-channel head coil.

Case 2
Patient history

Patient with stroke, stenosis of internal carotid artery.

Image findings / Results

The comparison of PASL and contrast enhanced perfusion imaging is showing the same areas of hypoperfusion.
PASL may be helpful in patients with acute stroke without the administration of contrast agent.

Case 3
Patient history

Pregnant patient with glioma in region of hippocamus.
No application of contrast agent because of pregnancy!

Image findings / Results

Hypervascularization is clearly depicted in glioma.
In this patient no contrast agent should be administered due to pregnancy.
Therefore, PASL was helpful in differential diagnosis of brain tumor.

1

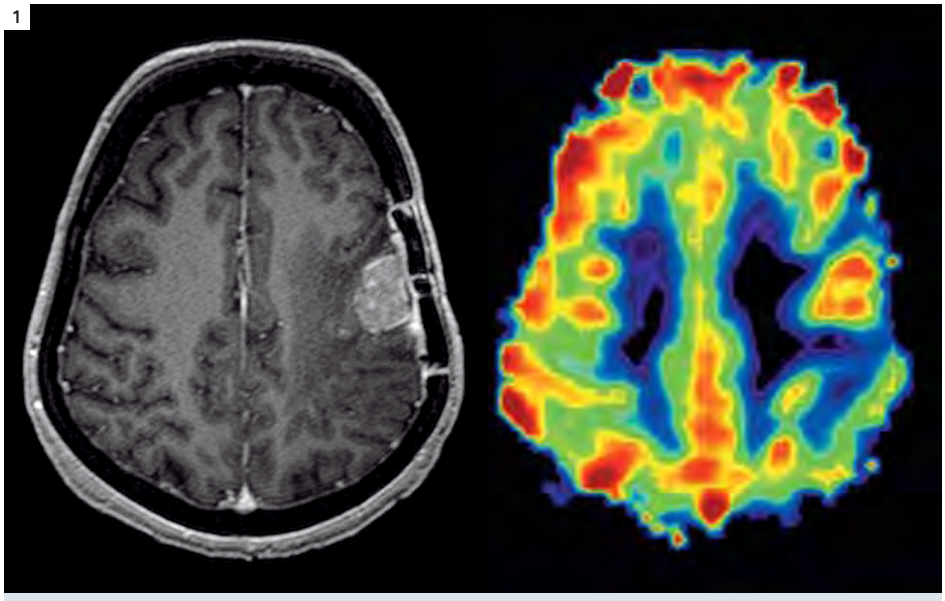

1 Case 1: PASL, FAIR, EPI, 16 slices, 5 mm slice thickness, 1 mm gap, TR 3800 ms, TE 18 ms, matrix 64 x 64, FoV 240 mm, 1 acquisition, Bandwidth 3005, Flipangle 90°.

Contact
Hans-Jörg Wittsack, Ph. D.
Inst. of Diagnostic Radiology
University of Düsseldorf, Germany
wittsack@uni-duesseldorf.de

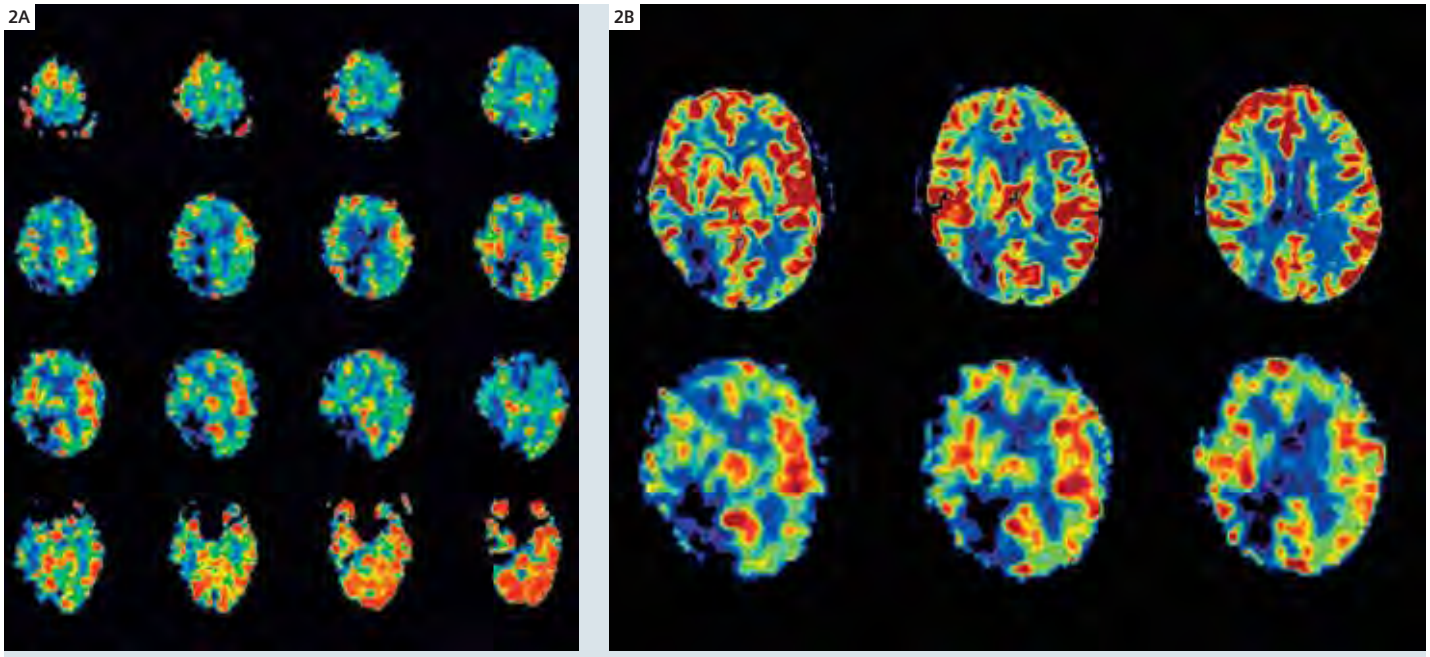

2 **Case 2:** PPASL, FAIR, EPI, 16 slices, 5 mm slice thickness, 1 mm gap, TR 3800 ms, TE 18 ms, matrix 64 x 64, FoV 240 mm, 1 acquisition, Bandwidth 3005, Flipangle 90°.

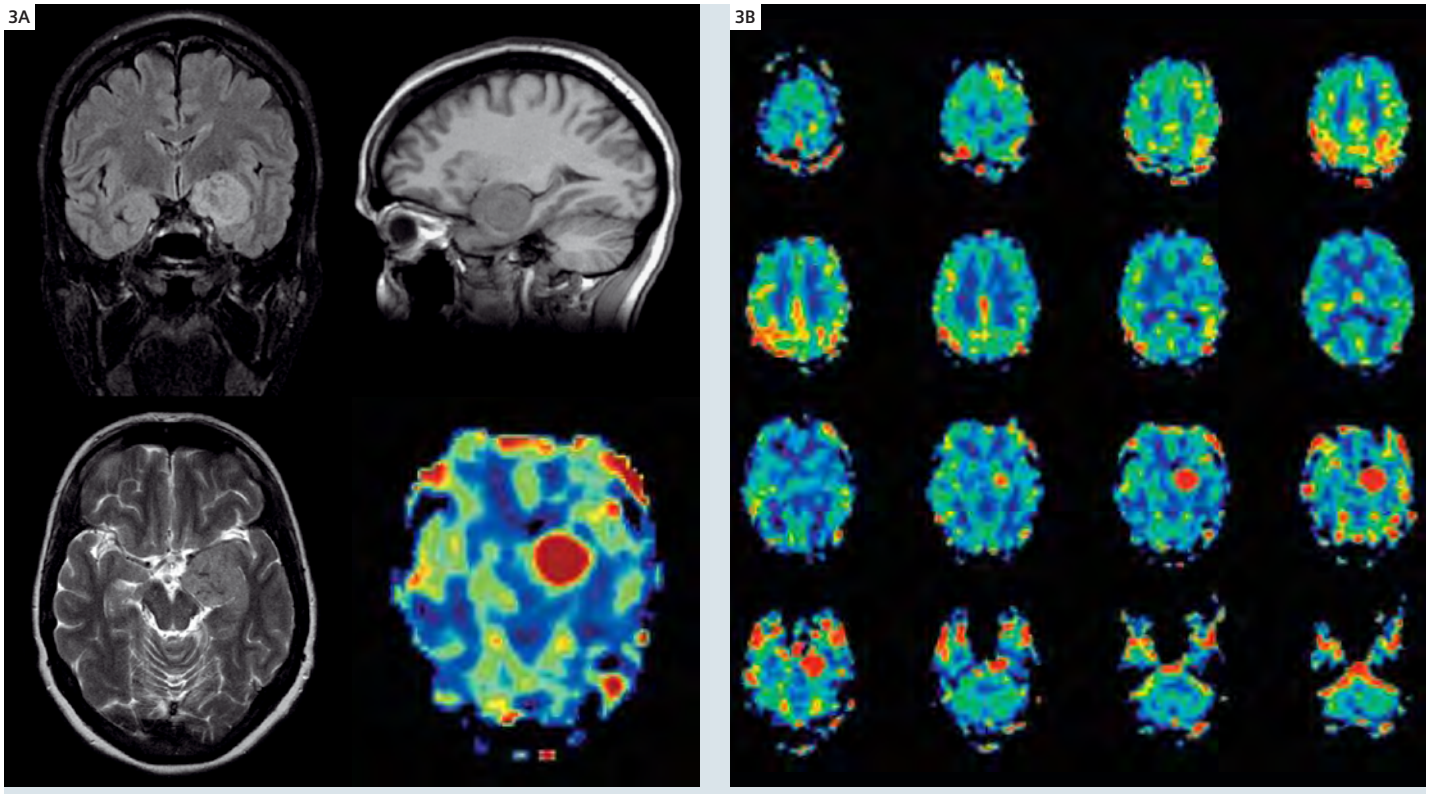

3 **Case 3:** PASL, FAIR, EPI, 16 slices, 5 mm slice thickness, 1 mm gap, TR = 3800 ms, TE = 18 ms, matrix 64 x 64, FoV 240 mm, 1 acquisition, Bandwidth 3005, Flipangle 90°.

Arterial Spin Labeling (*syngo* ASL) Case Reports from Xijing Hospital

Geng Chen; Yi Huan

Radiology department of Xijing Hospital, Xi 'an, Shannxi, China

Case 1

A 74-year-old woman presented with a history of aphasia for the last nine hours. Diffusion-weighted imaging (DWI) showed that there were acute cerebral infarctions in the left occipital, external capsule, adjacent to the lateral ventricle and centrum semiovale. Arterial Spin Labeling (ASL) showed a much larger region of potential ischemia. This perfusion/diffusion mismatch showed an indication for acute thrombolytic therapy.

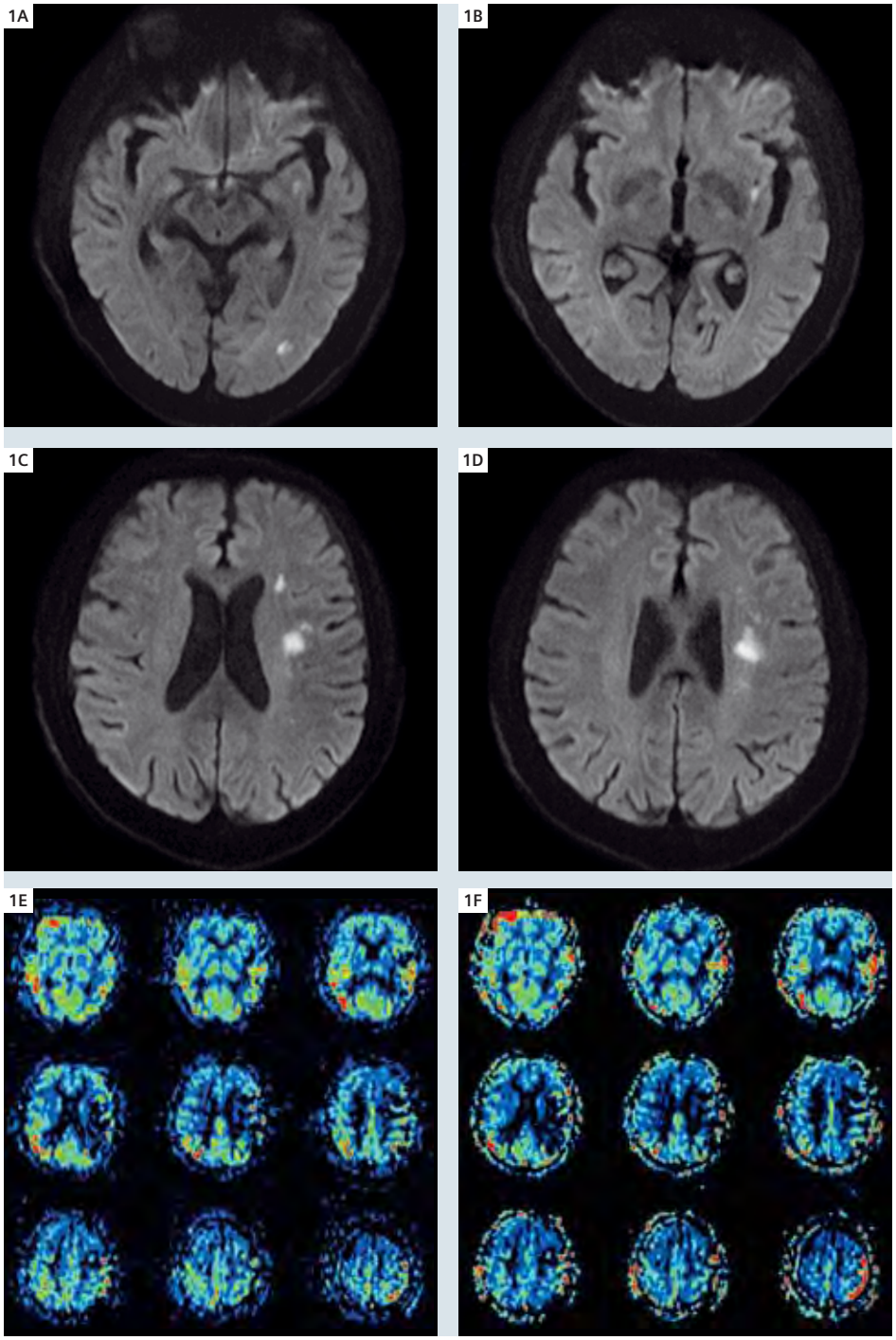

Case 2

A 42-year-old man complained for paroxysmal speech disorder and right hand disturbance since 3 days, the clinical diagnosis was transit ischemic attack (TIA). Conventional MR imaging and diffusion-weighted imaging (DWI) showed no obvious ischemic lesions. MR angiography (MRA) showed stenosis of the left middle cerebral artery. Arterial Spin Labeling (ASL) showed obvious hypoperfusion and hyperperfusion in the left temporal lobe.

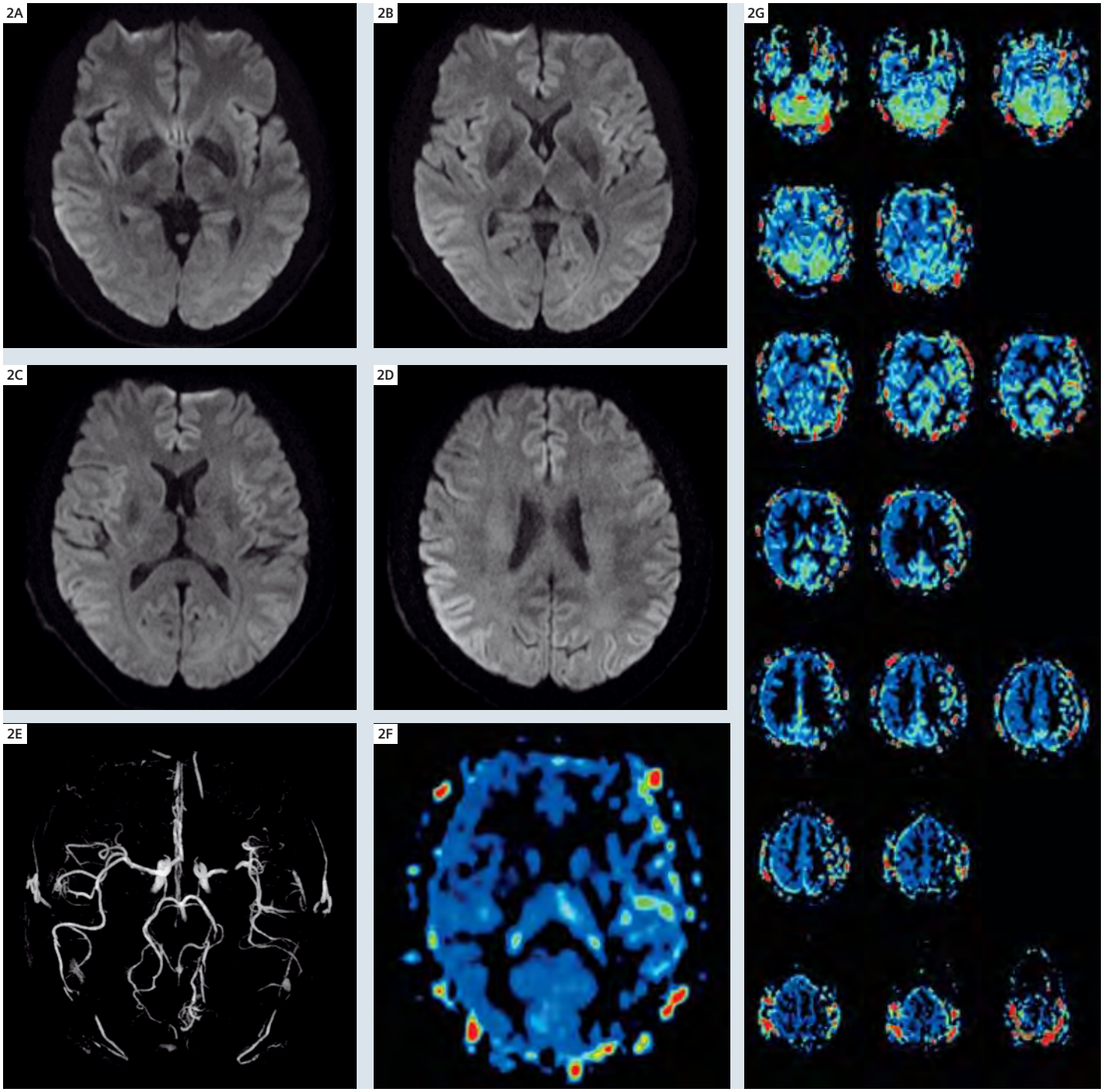

ASL Image Gallery from Tiantan Hospital

Jianping Dai, M.D., Ph.D.

Department of Radiology, Tiantan Hospital, Capital Medical University, Beijing, China

Case 1
Infarct

Diffusion-weighted image (DWI) shows high signal in the right occipital lobe and adjacent to the right lateral ventricle. Arterial Spin Labeling (ASL) shows significantly decreased perfusion in the occipital lobe.

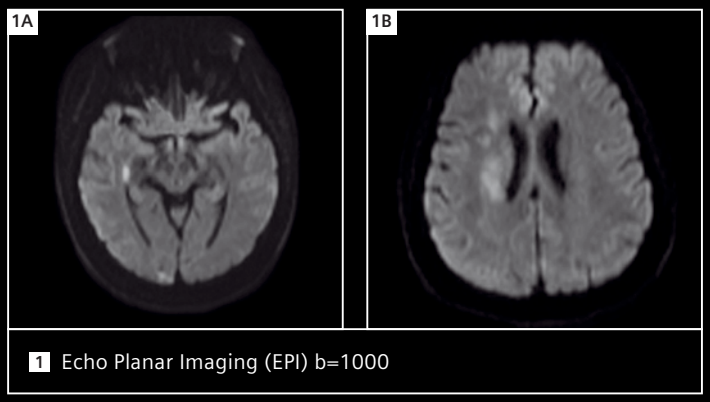

1 Echo Planar Imaging (EPI) b=1000

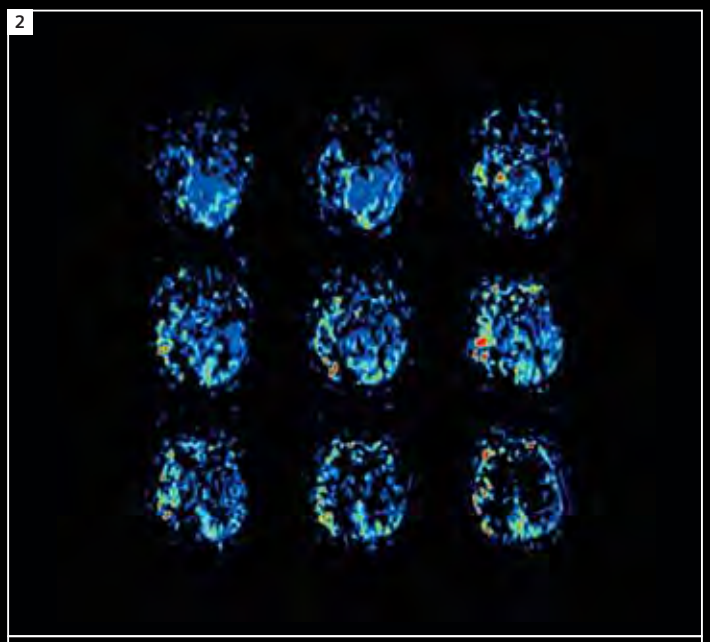

2 Arterial Spin Labeling (ASL)

Case 2
Meningioma

Right frontal lobe mass with high CBF.

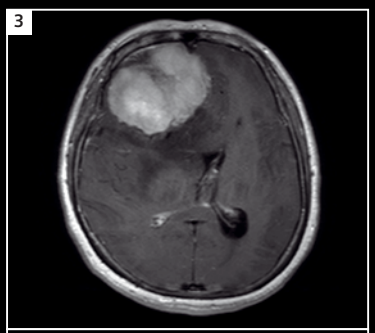

3 T1-weighted DarkFluid image.

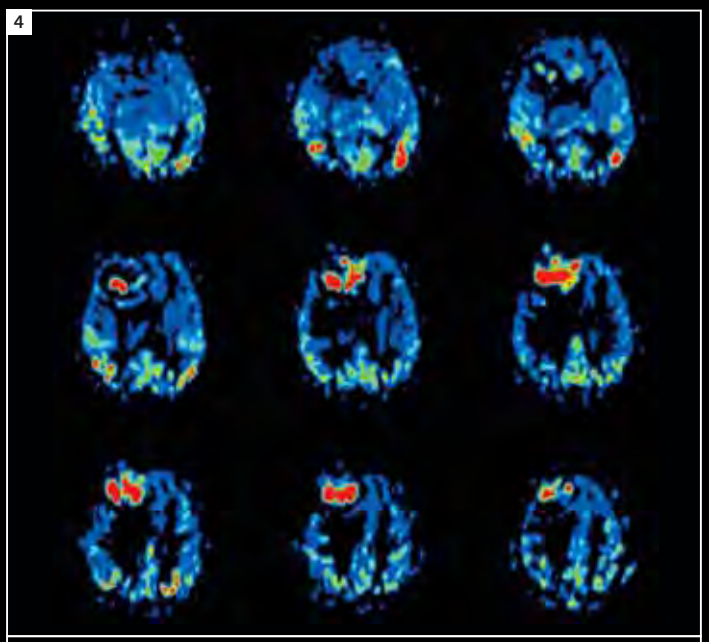

4 Arterial Spin Labeling (ASL)

ASL Image Gallery from Xuanwu Hospital

Kun Cheng Li, M.D

Department of Radiology, Xuanwu Hospital, Capital Medical University, Beijing, China

Case 1
Subacute infarct in the right basal ganglia area and right frontal lobe

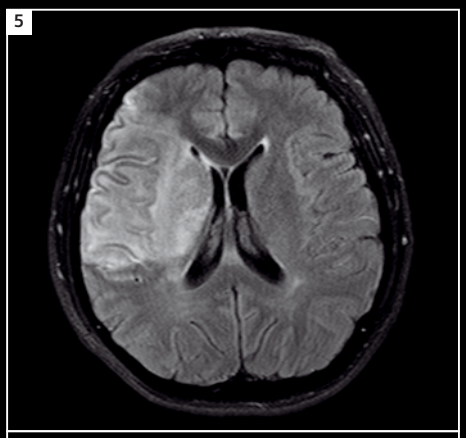

5 DarkFluid image.

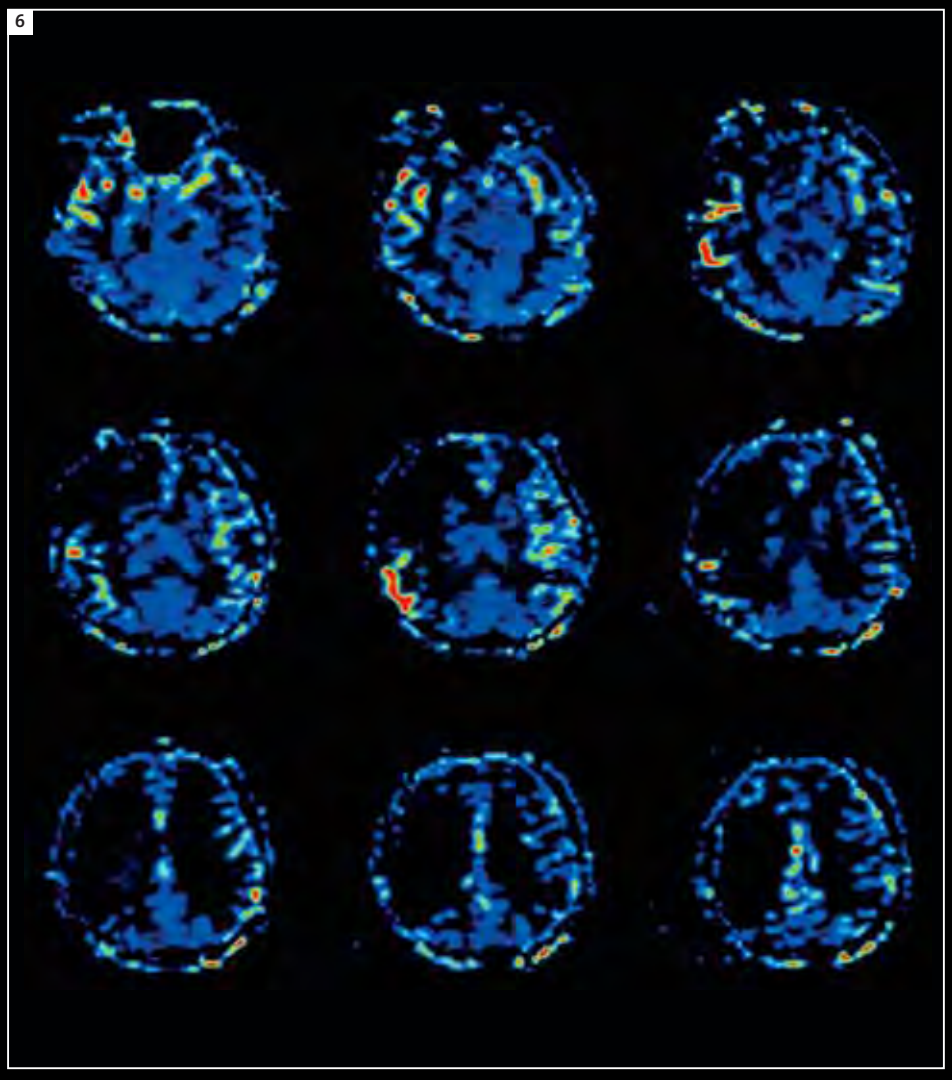

6 Arterial Spin Labeling (ASL)

Case 2
Meningioma in the right ventricle

7

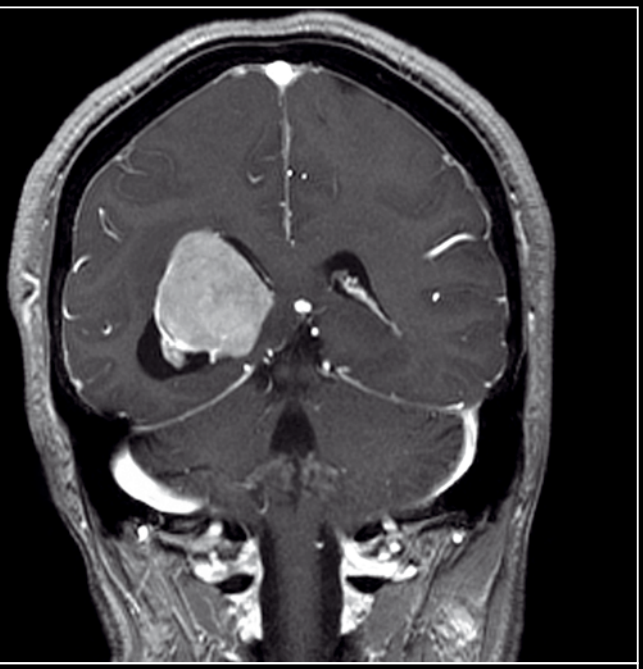

7 T1-weighted FLASH image.

8A

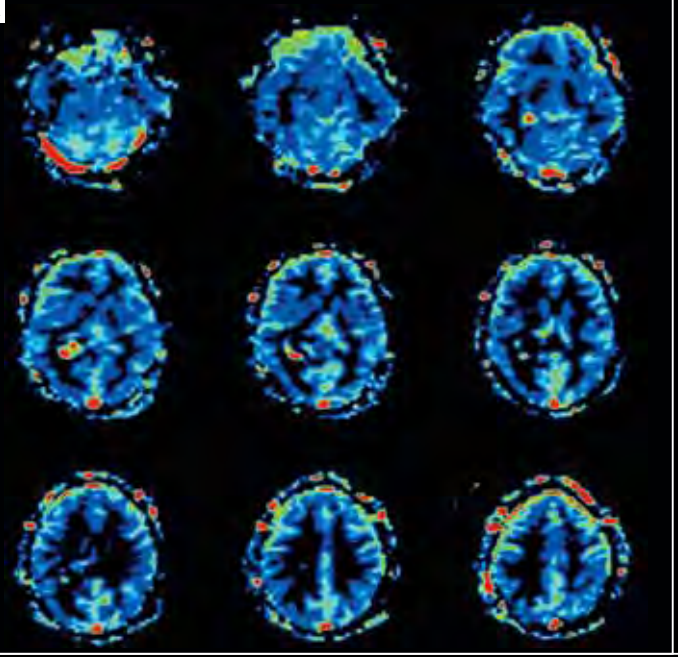

8A

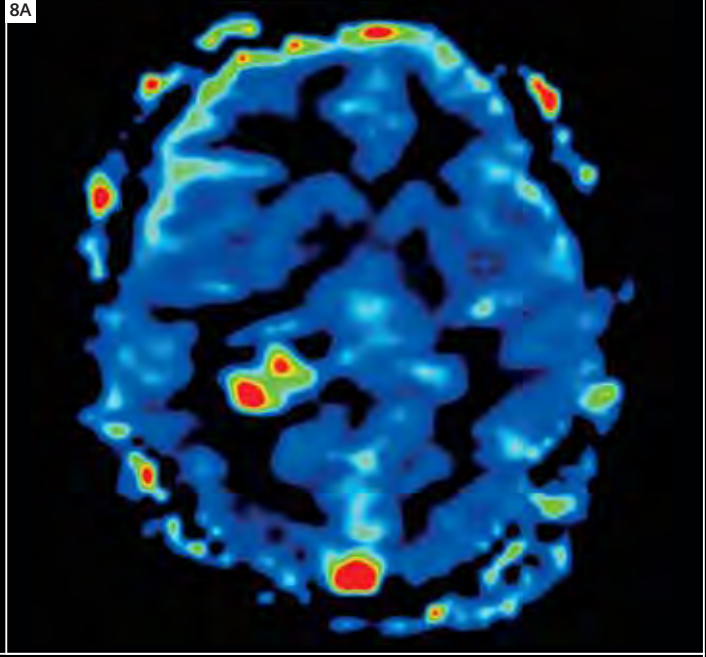

8 Arterial Spin Labeling (ASL), relCBF

Case 3
Glioblastoma

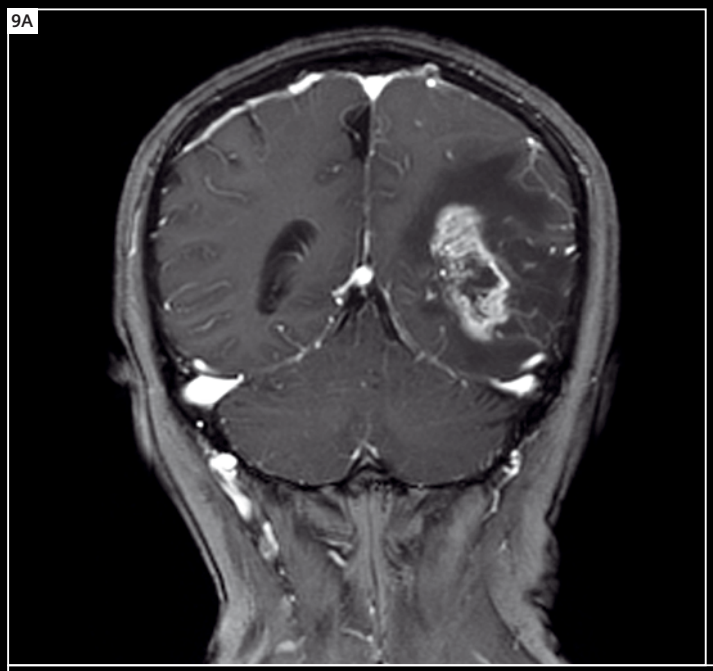

9 Arterial Spin Labeling (ASL)

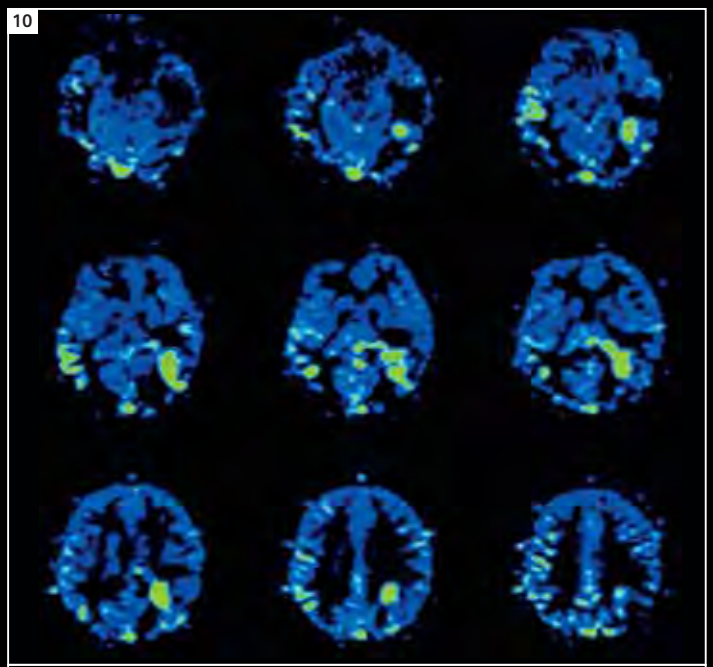

10 T1-weighed FLASH images.

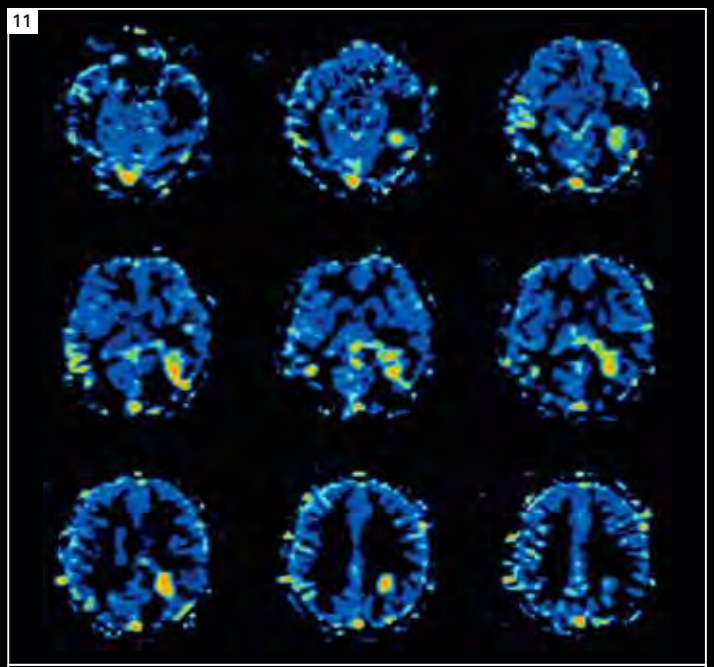

11 relative CBF

Case 4
Infarction

12A

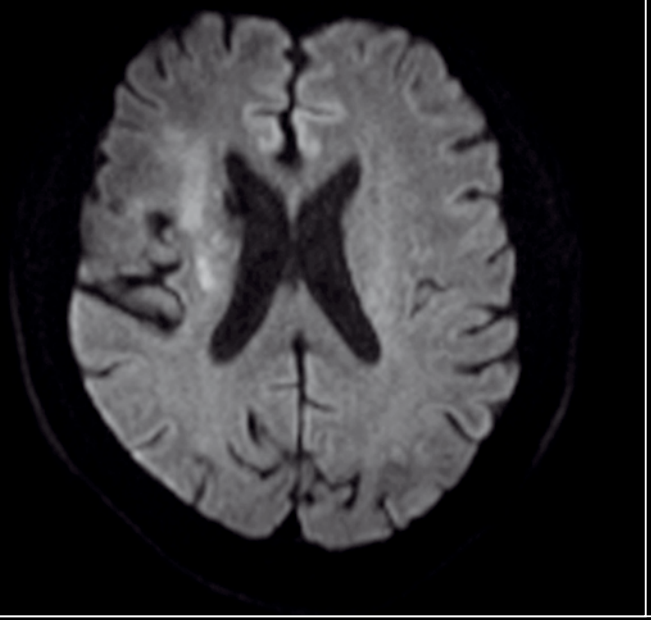

12B

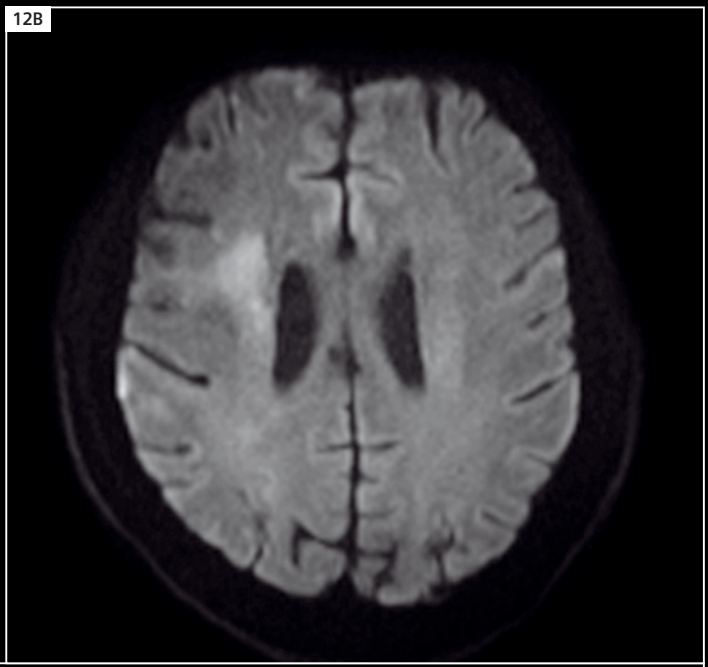

12 Echo Planar Imaging (EPI) b=1000

13A

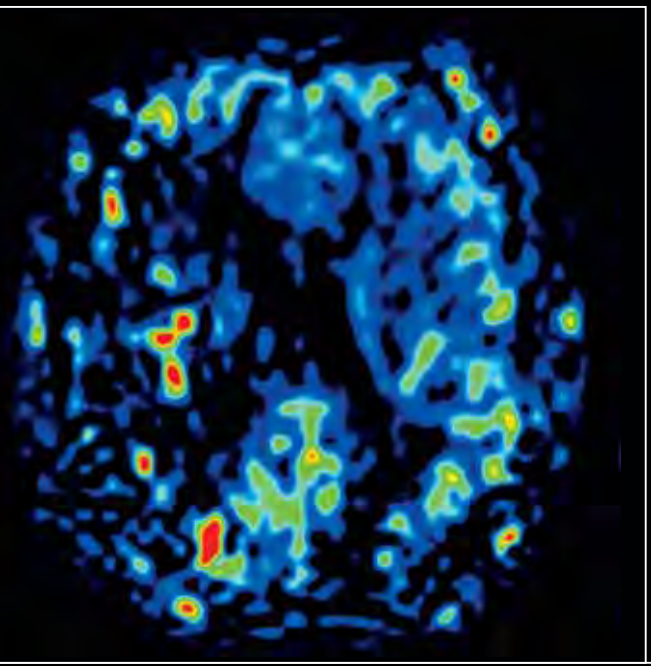

13B

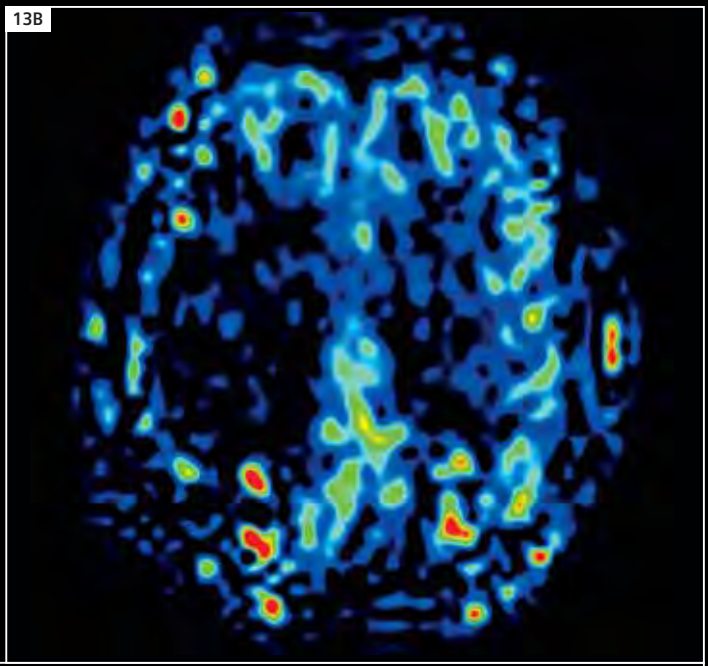

13 Arterial Spin Labeling (ASL)

Case 5
Right hemisphere low perfusion, right MCA lost flow signal

14A

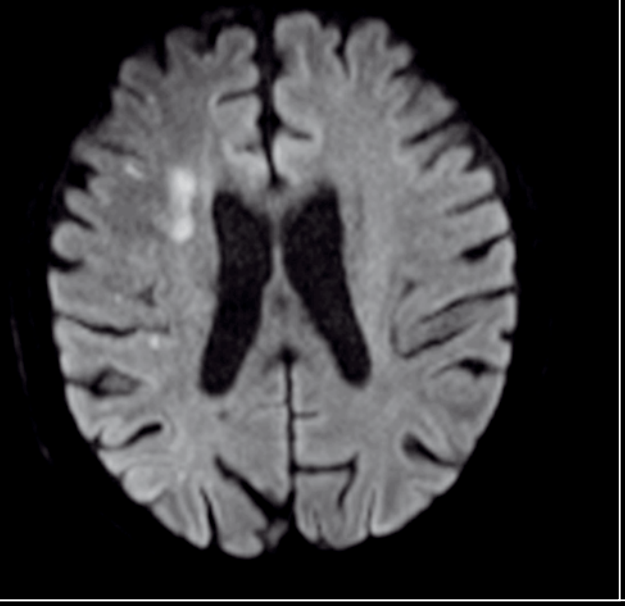

14B

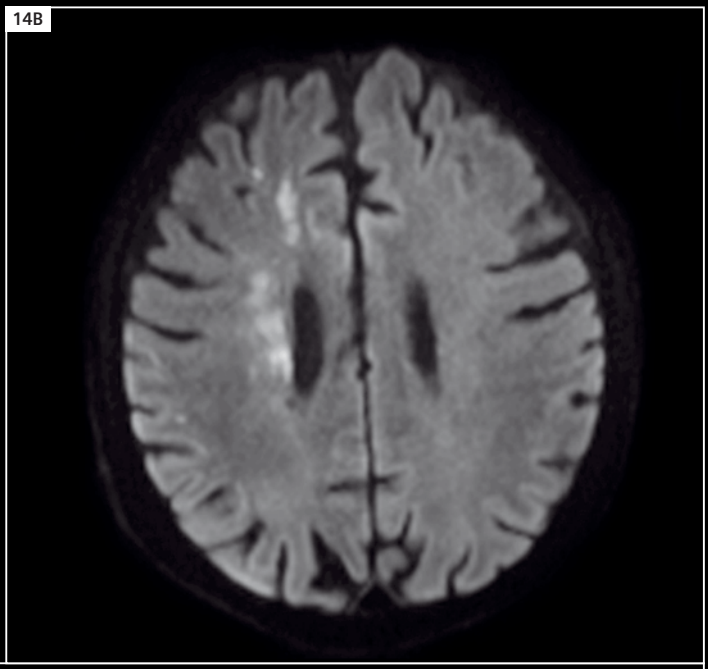

14 Echo Planar Imaging (EPI) b=1000

15A

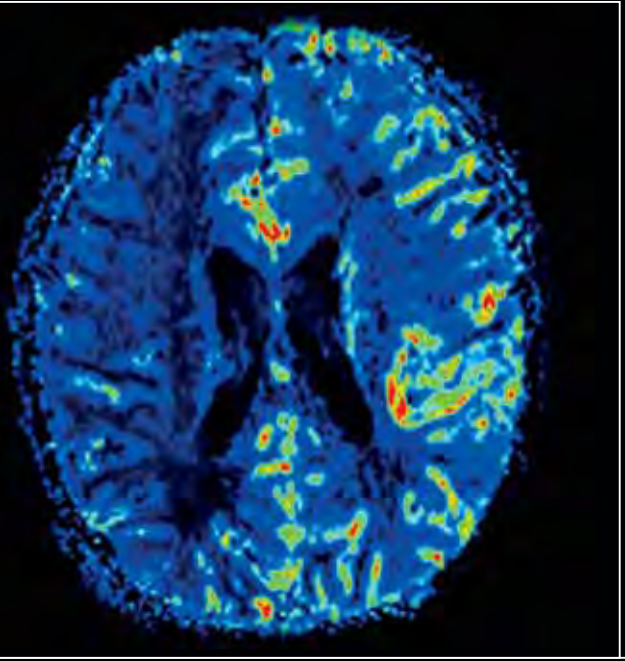

15B

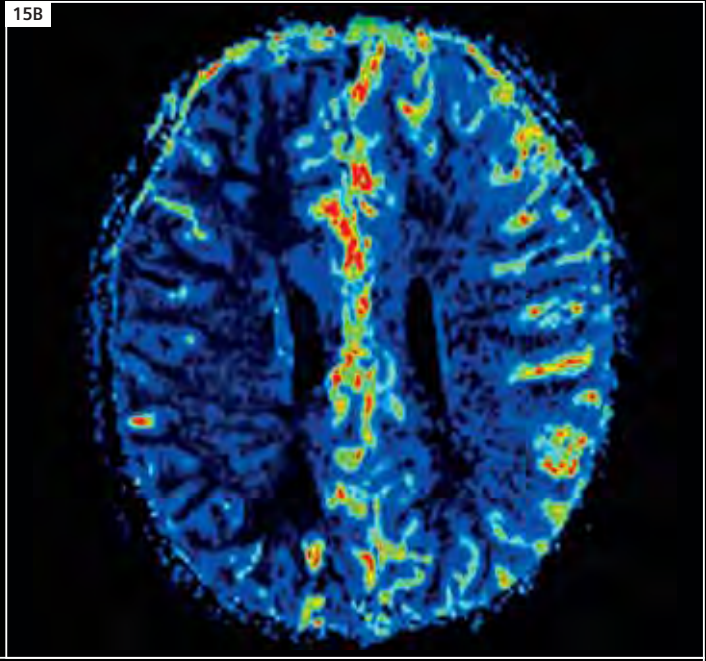

15 Arterial Spin Labeling (ASL)

Arterial Spin Labeling (*syngo* ASL) Case Reports from Nagoya University

Shinji Naganawa, M.D., Ph.D.

Department of Radiology, Nagoya University Graduate School of Medicine, Nagoya, Japan

Case 1
Patient history

40-year-old man had been operated because of a brain tumor in the left frontal lobe. After the operation, chemotherapy was applied. Recently, the patient showed focal seizure at his right upper limb.
Based on the MRI images we suspected the recurrence of brain tumor.
A second operation was performed to remove the brain tumor at left frontal lobe.The pathological diagnosis was a glioma grade 3.

Image findings / Results

The T2-weighted axial image shows that the abnormal signal intensity of the medial part of the left frontal lobe near the first operative surgical defect is enlarged compared with the MRI image of two months ago, and corresponding contrast-enhancement is not observed inside this tumor. Relative cerebral blood flow (rCBF) was increased in this tumor.
By these findings, we could not diagnose that this tumor was only grade 2, and suspected this tumor contained grade 3.

With ASL there was no significant difference between 3T and 1.5T. It takes 4:40 min and 1:02 min* to obtain 25 slices and 9 slices of ASL with 3T MAGNETOM Trio. And it takes 4:22 min* to obtain 9 slices of ASL with 1.5T MAGNETOM Avanto.
The Siemens unique multi-slice ASL sequence has Inline perfusion-weighted imaging (PWI) and regional cerebral blood flow (rCBF) processing.

1A T2-weighted ASL PICORE Q2TIPS. TR 2500, TE 13, TI 2 = 1800, TI 1 = 700, TI 1s = 1600, TA 1:02 min., matrix 64 x 64, FoV 240, Bandwidth 2230, Flip angle 90°. **1B** T1-weighted ASL PICORE Q2TIPS. TR 2500, TE 13, TI 2 = 1800, TI 1 = 700, TI 1s = 1600, TA 1:02 min., matrix 64 x 64, FoV 240, Bandwidth 2230, Flip angle 90°.

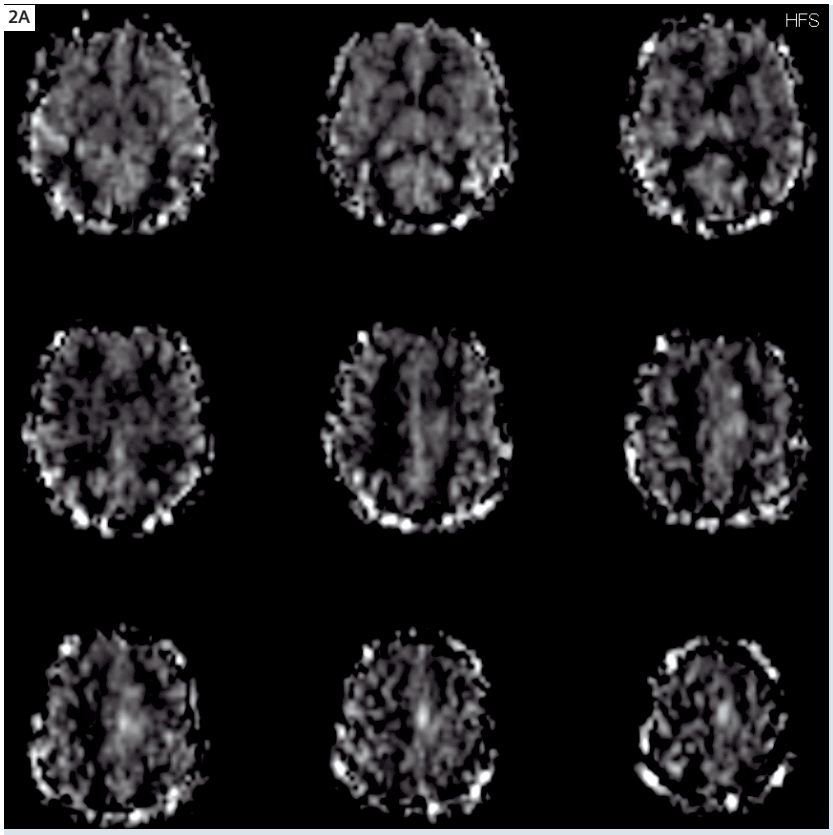

2A rCBF with 1.5T MAGNETOM Avanto.
2B rCBF with 3T MAGNETOM Trio.
For ASL there was no significant difference between 3T and 1.5T.

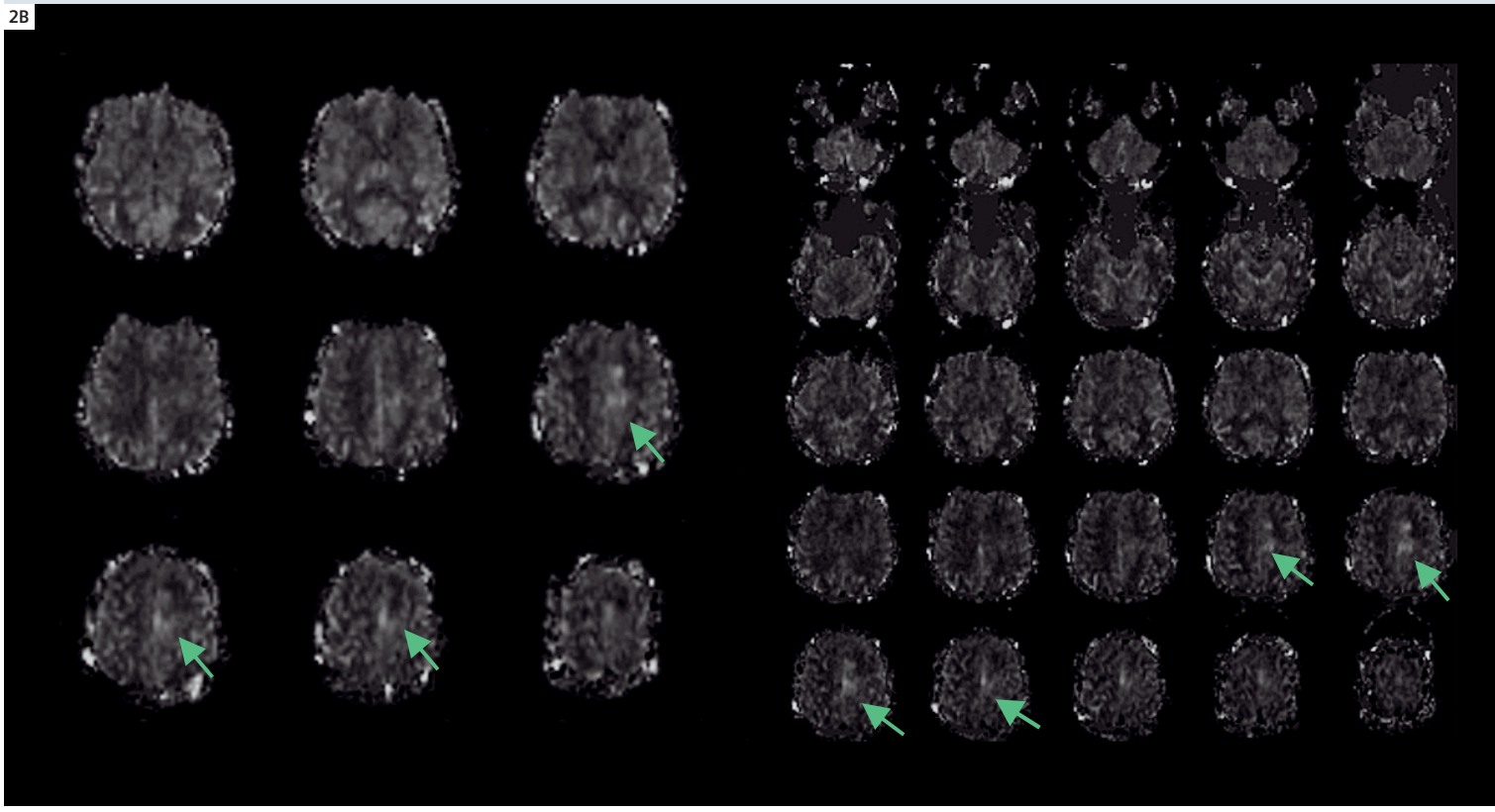

Case 2
Patient history

59-year-old man recently noticed dysarthria and motor weakness of right mouth angle. MRI revealed that a brain tumor was located in the fold just before the central sulcus in the left hemisphere, that is, the face area of the primary motor cortex. The patient's condition gradually deteriorated; therefore, the removal of this tumor was planned. Glioma G3 is predicted by preoperative findings by MRS, FDG and methionine PET.

Image findings / Results

The T2-weighted axial image shows the abnormal signal intensity of the dorsal part of left frontal lobe.
Corresponding contrast-enhancement is partly observed inside this tumor. rCBF is increased in this tumor. MR Spectroscopy (MRS) showed the pattern of malignant glioma.
By these findings, we suspected that this tumor was a grade 3 glioma.
The lesion could be clearly recognized at 3T. Not so clearly at 1.5T.

It takes 4:40 min and 1:02 min* to obtain 25 slices and 9 slices of ASL with 3T MAGNETOM Trio. And it takes 4:22 min* to obtain 9 slices of ASL with 1.5T MAGNETOM Avanto.

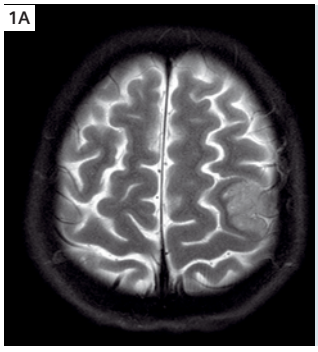

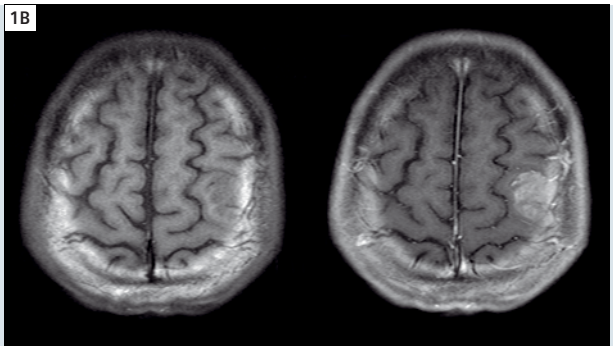

1A T2-weighted image. Brain tumor located in pre central gyrus, that is primary motor cortex (from the lateral part of hand area to the face area). ASL PICORE Q2TIPS. TR 2500, TE 13, TI 2 = 1800, TI 1 = 700, TI 1s = 1600, TA 1:02 min., matrix 64 x 64, FoV 240, Bandwidth 2230, Flip angle 90°.
1B T1-weighted images.

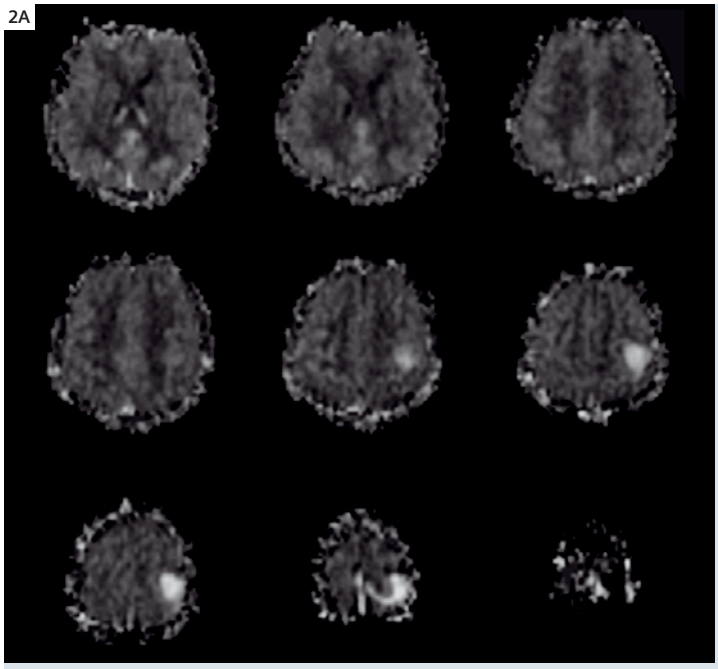

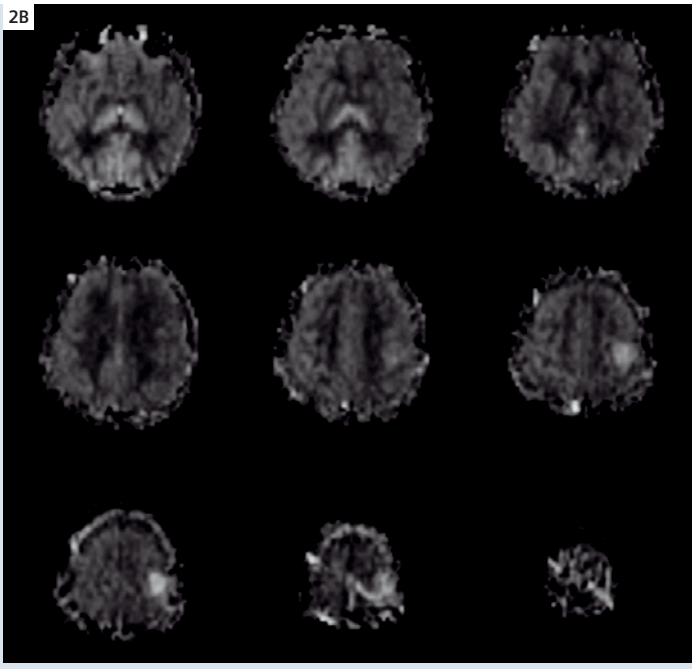

2A ASL with 3T MAGNETOM Trio rCBF was increased in the brain tumor.

2B ASL with 1.5T MAGNETOM Avanto The lesion could be more clearly recognized at 3T than at 1.5T.

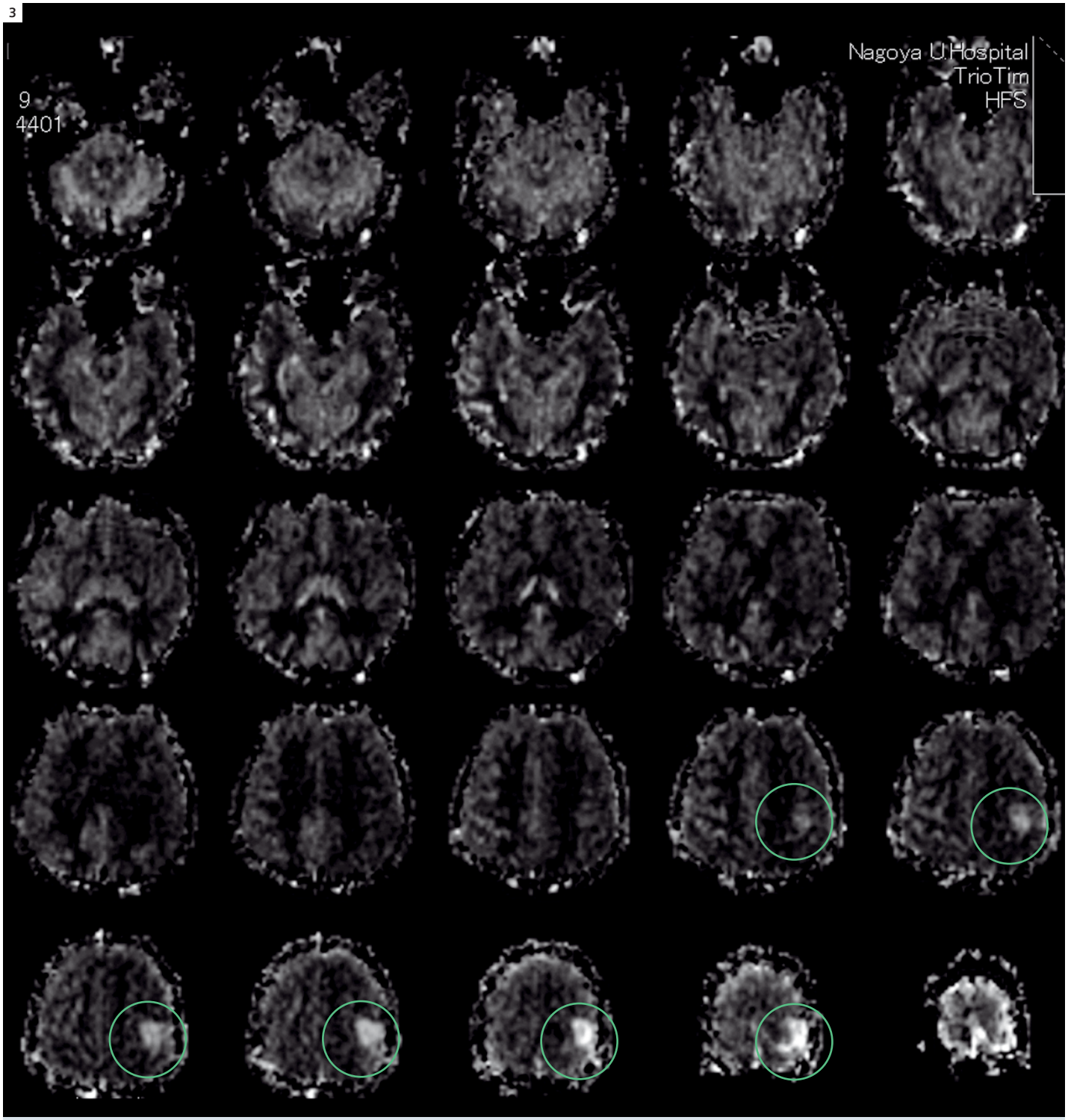

3 ASL with 3T MAGNETOM Trio, whole brain scan.

Case 3
Patient history

66-year-old male recently noticed motor weakness of left hand, and this symptom gradually deteriorated. An MRI showed mass lesion located in the right parietal lobe with ring enhancement and brain edema was widely observed.
Malignant tumor, that is, Glioblastoma or metastasis was suspected by MRI findings. The pathological diagnosis was glioblastoma at WHO grade 4.

Image findings / Results

Ring enhanced mass was found in the right parietal lobe with apparent brain edema. Spotty enhanced areas were also found. rCBF is considered to be partly increased in this tumor.
By these findings, we suspected that this lesion was a glioblastoma, metastasis and brain abscess.
Diffusion-weighted imaging did not show very high signal, therefore, brain abscess was unlikely. Open biopsy was performed and revealed glioblastoma at WHO grade 4. It takes 4:40 min and 1:02 min* to obtain 25slices and 9 slices of ASL with MAGNETOM Trio. And it takes 4:22 min* to obtain 9 slices of ASL with MAGNETOM Avanto.
The reslults of ASL do not differ between 3T and 1.5T. There is, however, a great difference in acquisition times.

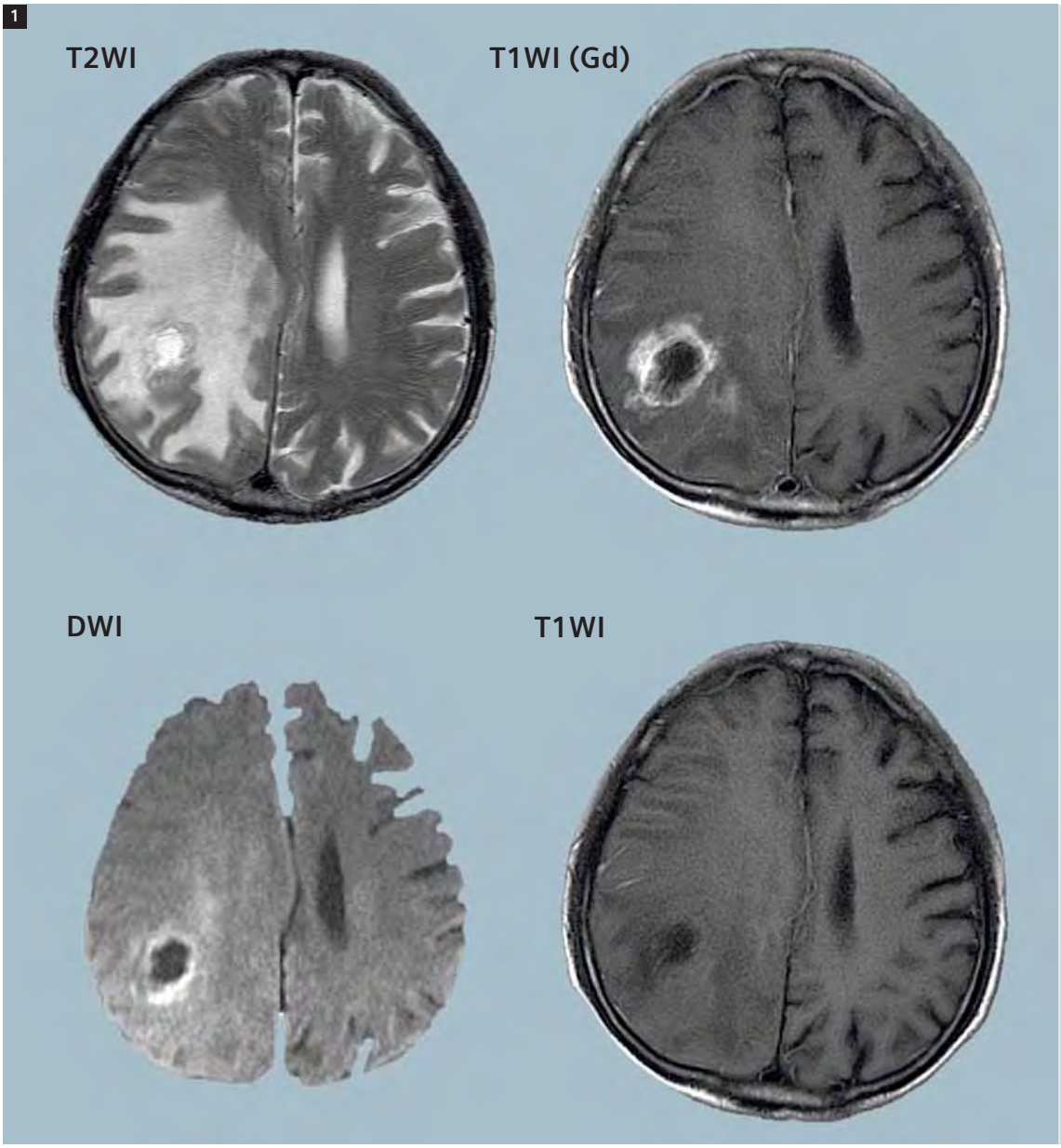

1 Ring enhanced mass was found in the right parietal lobe with apparent brain edema. Spotty enhanced areas were also found. By these findings, we suspected that this lesion was glioblastoma, metastasis and brain abscess.

2

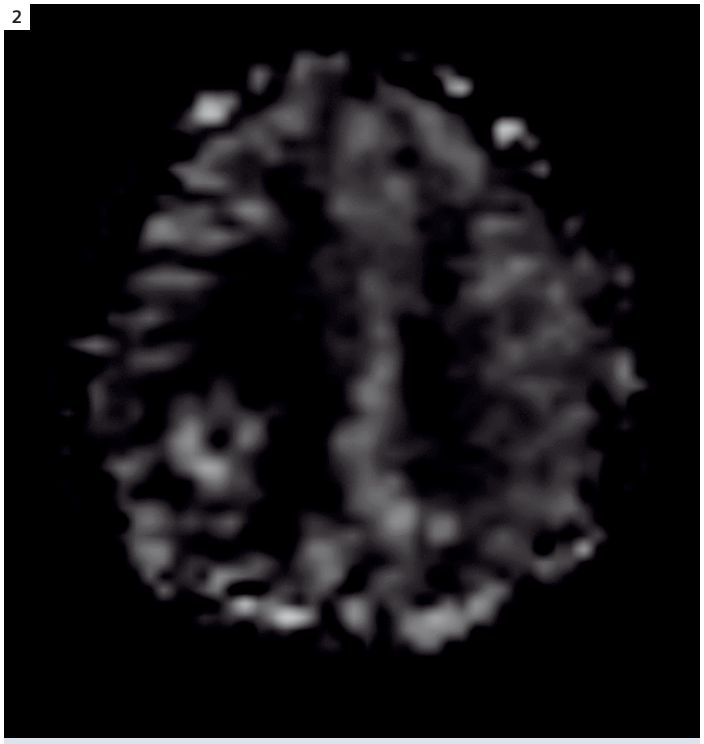

2 Diffusion weighted imaging did not show very high signal, therefore, brain abscess was unlikely. rCBF is partly increased in this tumor.

3

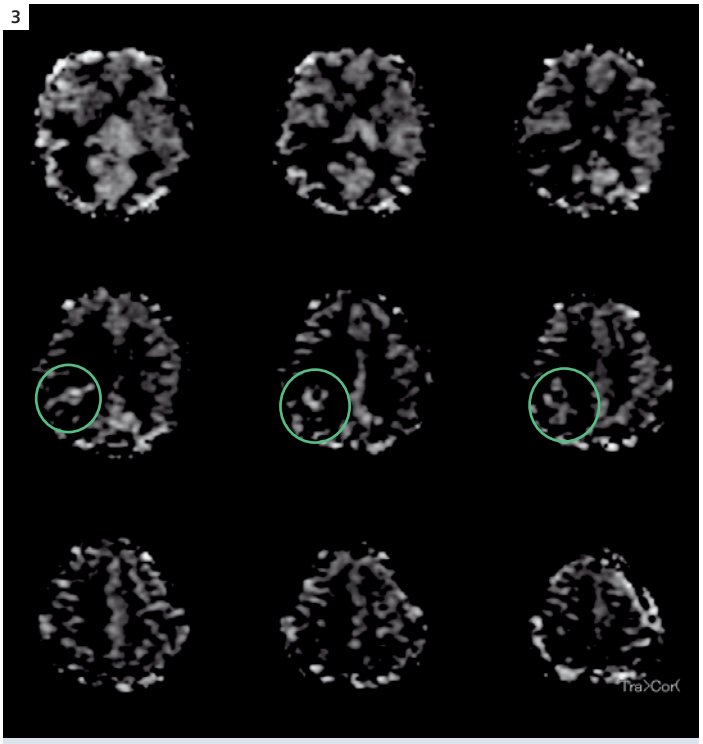

3 ASL with 1.5T MAGNETOM Avanto.

4

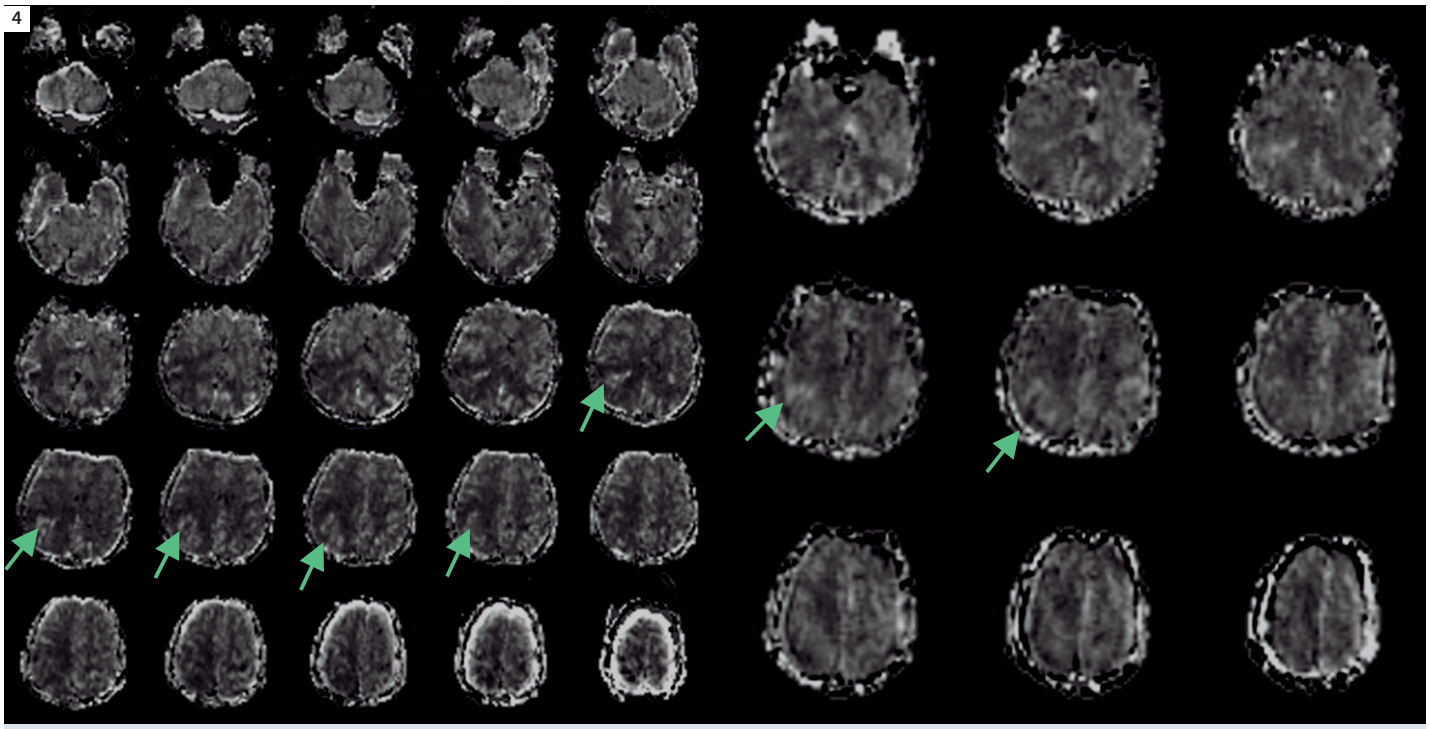

4 ASL with 3T MAGNETOM Trio. The image on the right is blurred because of motion artifacts. We found significant difference between 3T and 1.5T.

1A T2-weighted image.
1B Susceptibility-weighted image (*syngo* SWI). Subcortical hemorrhage was observed in the right parieto-occipital lobe. Brain edema was confirmed near hemorrhage, but mass sign was not so severe. We could not find apparent ischemic lesion in the left hemisphere.

Case 4
Patient history

65-year-old female presented in the emergency room with disturbance of consciousness and suddenly occurring left hemiparesis. Head CT showed subcortical hemorrhage in the right parieto-occipital lobe. She was admitted to the intensive care unit (ICU). The patient was managed conservatively and follow up MRI was performed.

Image findings / Results

MR imaging showed the subcortical hemorrhage in right parietal lobe. MR angiography (MRA) showed no vascular abnormality in the right hemisphere and accidentally disclosed left M1 occlusion. rCBF is decreased in the area of left main coronary artery (MCA).

Contact
Shinji Naganawa, M.D., Ph.D.
Professor and Chairman
Department of Radiology
Nagoya University Graduate School of Medicine
65 Tsurumai-cho, Showa-ku,
Nagoya, 466-8550
Japan
naganawa@med.nagoya-u.ac.jp

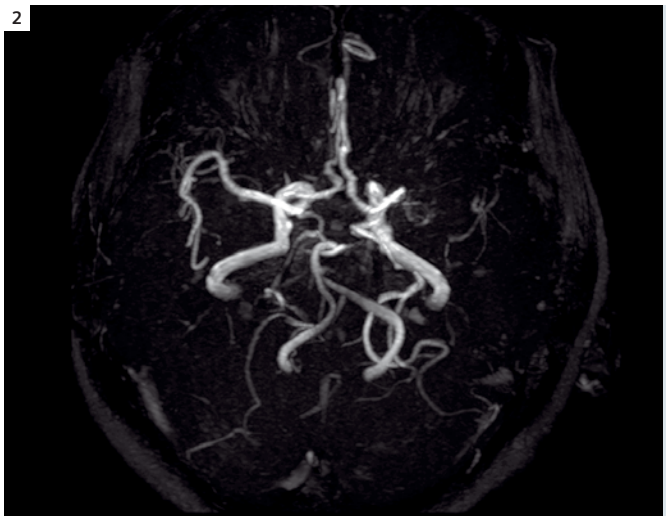

2 MR Angiography: left M1 occlusion was suspected. This patient did not complain of motor weakness of the right hand.

*Results may vary. Data on file.

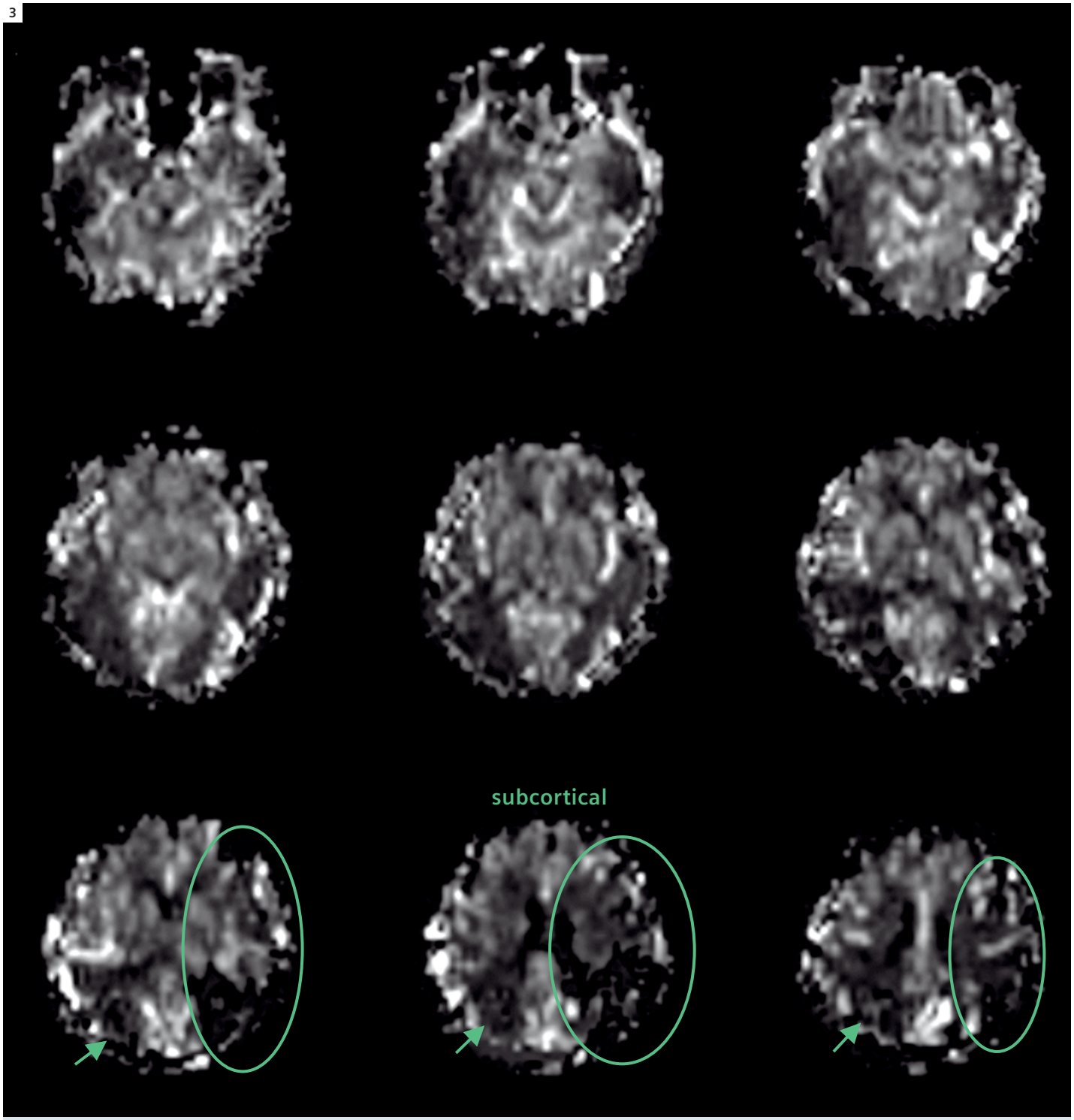

3 Arterial Spin Labeling (ASL): rCBF is decreased in the area of the left middle cerebral artery (MCA).

Highly Parallel Detection for MRI

Lawrence L. Wald[1, 2]; Graham Wiggins[1]

[1]Athinoula A. Martinos Center for Biomedical Imaging, Department of Radiology, Massachusetts General Hospital and Harvard Medical School, Boston, MA, USA
[2]Harvard-MIT Division of Health Sciences and Technology, Cambridge, MA, USA

Introduction

Over the past two decades, phased array detection of the MR signal has benefited from a focused and sustained engineering effort. From the introduction of the first local coils on the MAGENTOM platform in 1983, the advantages of surface coil detection could be seen. The inception of array technology in the early 1990's, where a few coils were used to extend surface coil coverage and sensitivity, clearly demonstrated the power of extending the surface coil concept with arrays. The important clinical benefit of being able to match the reception strategy to individual clinical targets was not achieved until the introduction of the Integrated Panoramic Array (IPA) on the MAGNETOM Symphony in 1997. Here, the user controls the selection of the array elements from a larger array placed on the patient. While a seemingly simple and obvious extension in flexibility, the engineering challenge of seamlessly integrating the IPA methodology is belied by its continued lack of repetition within the industry.

The final step in extending array technology came from the recognition that optimal linear combinations of the coil elements could preserve much of the sensitivity and iPAT (integrated Parallel Acquisition Technique) capability of a larger array and provide a tradeoff between signal homogeneity, sensitivity and iPAT performance. Thus, while preserving the flexibility of the IPA concept, Tim (Total imaging matrix) significantly extended performance, leading to today's state-of-the-art in array technology where the practitioner has the ability to place over a hundred receive elements on the patient and combine them into up to 32 independent receive channels with a sophisticated mode-mixing matrix designed to optimize coverage, sensitivity and iPAT acceleration.

So, what is left to improve upon? Past success drives future development, and Tim technology has done much to fuel speculation about what the ultimate limits of array detection technology are for sensitivity and iPAT capability. In this article we examine theoretical limitations in parallel imaging technology: the so-called "ultimate SNR (signal-to-noise ratio)" and "ultimate g-factor (geometry-factor)", a measure for coil efficiency regarding its iPAT performance. Finally, we try to identify future directions for parallel RF hardware based on the conclusion that there are still significant gains possible. In particular, we wish to explore how parallel imaging technology might benefit if the coil designer was unconstrained by the number of RF channels available on the instrument. Toward this goal, the introduction of a prototype MAGNETOM Trio, A Tim System with 128 independent receive channels has given us the opportunity to move beyond theory and try to realize the potential benefits of highly parallel array detection.

> "While preserving the flexibility of the IPA concept, Tim significantly extended performance."

In these "highly parallel detectors", the role of the image encoding is no less important than the role of signal detection. While we continue to think of the gradient coil as the principal "encoder" of the MR image, this view is becoming outdated. With iPAT squared (iPAT^2) methodology – iPAT in 2 dimensions, acceleration rates above 10-fold can be achieved with Tim technology. Thus, the gradients account for as little as 10% of the encoding; the rest of the burden being placed on the receive array. In this scenario, the role of the MR detector array begins to more resemble the electroencephalography (EEG) or magnetoencephalography (MEG) detector. In these devices all of the spatial information is derived from the detector geometry. Although there appears to be limits on the ability of the array to encode spatial information distant from the coils, the MEG/EEG case can serve to educate us on the extraction of useful spatial information when faced with an ill-conditioned inverse problem. We are only beginning to explore the potential of these methods much less the hardware needs of this unusual regime.

Basic signal and noise considerations

A principal design goal is to inductively tightly-couple the receive coil to the pre-

cessing nuclear magnetization. Because the spins in the body lie in an ionic bath (salt water), the coil is also tightly coupled to randomly fluctuating fields produced by ionic currents. The currents that happen to have frequencies within the bandwidth of the RF receiver appear as spatially uniform Gaussian distributed noise in the complex image. An equivalent picture is produced by a reciprocity argument. Here, the effectiveness of the receive coil is proportional to its efficiency as a transmit coil. The receive noise power is proportional to the power dissipated in the conductive tissue through eddy current damping (driving the ions with the electric field associated with the changing transmit field.) In either picture, the same basic rules of thumb arise. The more effective the receive coil is at detecting the spins, the more effective it will be at receiving the noise. Thus, once "body noise dominance" has been achieved, gains in SNR can only be achieved by limiting the volume of tissue contributing the noise. For example, the coil should only interact with tissue that is of interest; tissue outside of the imaging field of view (FoV) but within the region of coil sensitivity produces only unwanted noise. Arrays take advantage of this principle by their "divide and conquer" method, where each individual array element sees only a limited "noise" region.

Three related sensitivity figures of merit for the array coil are of interest:

a) the SNR as a function of position for un-accelerated scans,

b) a similar SNR map for accelerated scans and

c) the maximum acceleration achievable with an acceptable g-factor penalty. The g-factor penalty is the ratio of the unaccelerated to accelerated SNR corrected for the reduced scan time (which contributes a factor of the square root of the acceleration rate). General simulations of array coils are challenging since there are a near infinite number of design choices. Nevertheless, analyzing arrays of identical coil elements arranged to cover simple sample geometries (such as spherical or planar regions) can provide insight into more complicated variations. One particularly illuminating approach for understanding the future benefits of larger array configurations is to analyze how the SNR is affected by a larger and larger number of array elements covering the same area [1, 2]. Studies of this kind have analyzed planar [1] and spherical arrays [2].

"The quest for higher sensitivity and improved encoding acceleration both drive exploration of the logical expansion of the array approach: increasing the number of elements and reducing the size of the receive coils."

In the planar case [1], a square region was tiled with N = 1, 4, 16 and 64 square array elements in a 1x1, 2x2, 4x4 and 8x8 configuration. The coils were overlapped by the width of the conductor and were modeled as being 1 cm above an infinite half-space of lossy salt water (σ = 0.72 S/m). The coils were assumed to have no inductive coupling (e.g. from perfect preamplifier decoupling or decoupling networks) but the noise correlation from their shared view of the sample noise was calculated using a full-wave analysis. The SNR was then calculated as a function of depth from the center of the array. The SNR near the array was found to scale approximately with the number of array elements per side (i.e. with $\sqrt{}$ where N is the total element count). Thus, a 4-fold potential sensitivity gain can be expected for tissue near the array by moving from a modest number of array elements (N = 4) to a "large-N" array (N = 64). This gain is, however, lost for deeper tissue (depths approximately equal to the lateral size of the overall array). On the other hand, there is no depth at which an array of fewer elements outperforms the arrays with more elements. Thus large gains near the surface are potentially achievable at the cost of an added number of receive channels and a less homogeneous sensitivity profile. The reception inhomogeniety has become increasingly less problematic with the arrival of robust normalization algorithms, such as the Normalize and Prescan Normalize features on *syngo*.

In a separate modeling study, circular coils were uniformly distributed in both a gapped and overlapped configuration around a 22 cm diameter sphere of conductive dielectric material modeling biological tissue [2]. N = 8, 12, 16, 20, 26, 32 and 64 circular coils were tiled on the sphere. In addition to the noise from body loading, the coils were assigned a non-body noise level determined from typical copper and preamplifier noise contributions. In addition to modeling SNR for un-accelerated scans, this work modeled the additional g-factor penalty incurred in accelerated imaging and examined the SNR as a function of B_0 and compared the model results to that expected from the so-called "ultimate" SNR; the highest achievable SNR obtainable with an arbitrarily large array whose individual sensitivity basis set satisfying Maxwell's equations [3–5].

In the spherical case, the results were qualitatively similar to the planar case. The largest gains achieved by increasing the number of array elements (N) occurred near the coil elements. At a radius of

*Works in progress (WIP). The information about this product is preliminary. The product is under development and not commercially available in the U.S., and its future availability cannot be ensured.

9 cm in the 22 cm diameter sphere, the SNR of the unaccelerated image at 1.5T increased 3.5-fold when the number of loops was increased from 8 to 32. In this case, the dependence on N was observed to be closer to linear with N compared with the $\sqrt{}$ seen near the planar array. Like the planar case, however, the benefits were considerably smaller more distant from the array elements. At the center of the sphere the unaccelerated 1.5T SNR increased only ~5% with the 4-fold increase in N. At higher field strength, there was more room for improvement at the center of the object. At 7.5T for example, only a very small region in the center of the phantom was within 10% of the ultimate SNR levels for a 64-channel array [6].

Accelerated imaging showed even larger gains as coil elements were added, especially for high acceleration rates. For example at Rate = 3, the g-factor penalty was 1.4-fold larger for the 8-channel array compared to the 32-channel. At Rate = 4, this widened to a factor of 2. The final accelerated image benefits from both the intrinsic sensitivity improvements as well as the g-factor gains. An additional finding of this study was an improved SNR for the overlapping array configuration compared to the gapped configuration for the largest N coils for both unaccelerated and accelerated scans. For the smaller array, the gapped array was beneficial for accelerated scans; a result seen by other studies [7, 8].

"Ultimate" SNR of arrays

Several studies have examined the upper bound on sensitivity and spatial encoding capabilities of coil arrays. The concept of the "ultimate" SNR achievable by an RF coil was introduced by Ocali and Atalar [5]. An arbitrary coil sensitivity profile outside a sample was generated from a complete set of basis functions satisfying Maxwell's equations (either plane waves or spherical harmonics) and a linear combination was found that maximized the SNR at a given location in the sample. This work was expanded to include the SNR of accelerated imaging [3, 4]. The ultimate SNR for accelerated imaging is found by analyzing the performance of the complete basis set.

The first interesting conclusion of this analysis is that the sensitivity of MR detection is intrinsically limited. The significance of this for future array designs, of course, hinges on how close current array designs are to this theoretical ceiling. Comparing actual designs (such has the arrays of circular coils tiling a spherical phantom reviewed above), suggest that a 32-channel array is close to the theoretical limit at the center of the phantom [2]. Happily for the employment prospects of array designers, there is substantial room for improvement towards the periphery. At a radial location equal to 80% of the coil radius, there is still a factor of 7 to go before the theoretical limit is achieved [2].

The ultimate limitation of the ability of the array for spatial encoding (iPAT) is likely imposed by a fundamental smoothness to the coil sensitivity patterns in regions free of current sources. This fact of nature derives from Maxwell's equations. Both studies examining the ultimate acceleration limits point out a steep drop in the SNR for accelerations above about R = 4 or 5 [3, 4]. For example, after this rate, the g-factor penalty was seen to rise exponentially with acceleration rate for locations near the center of the spherical sample [3]. Both studies found that moving to higher B_0 field strength postponed the rapid deterioration of SNR for rates above 4x. As with the unaccelerated SNR, the situation improves as you move closer to the array elements. Here the proximity to the wires provides more rapidly varying spatial profiles. This proximity effect allowed the 64-element array of McDougall and Wright [9] to achieve credible images with an acceleration rates of 64-fold; considerably higher than the 4 to 5-fold limit suggested by the ultimate sensitivity analysis which focused on regions far from the array.

Highly parallel arrays in practice

Historical experience with array coils quickly showed that signal detection efficiency improved with even a modest number of surface coils and that the reception uniformity and reconstruction burden could be handled with simple post-processing algorithms such as the Normalize and Prescan Normalize feature. The use of surface coils was thus able to expand into the traditional role of volume coil structures. The quest for higher sensitivity and improved encoding acceleration both drive exploration of the logical expansion of the array approach: increasing the number of elements and reducing the size of the receive coils (to cover a fixed anatomical territory). With other manufacturer's likely to follow the Tim system's technology, at least in channel count, 32 receive channels is becoming the new standard, and multiple groups are developing torso / cardiac [10, 11], and brain [12] [13, 14] arrays for these instruments.

Although exploring arrays of N > 32 channels clearly risks hitting the limits identified by the studies of the ultimate sensitivity for MR, the theory suggests there is room for improvement and such important limitations must be extensively explored experimentally. We have therefore gone on to build such arrays explicitly to determine the potential capabilities and practical limitations of even larger-N arrays (96 and 128 channels). The overall picture of these two efforts has been to support the case that parallel imaging strategies can receive expanding benefits from these "large-N" arrays.

Close fitting brain arrays with 32 and 90 and 96 channels

Preliminary experience in highly parallel acquisition strategies using helmet shaped geometries of circular receive coils has concentrated on building and testing brain array prototypes for 1.5T, 3T, and 7T. Tests so far include 23 and 90-channel arrays for 1.5T [15] and 32 and 96-channel

arrays for 3T [12] and 32-channel arrays for 7T. All of the arrays were built onto a helmet shaped former that conforms closely to the head. The tiling strategy for the individual circular surface coils was based on the combination of hexagonal and pentagonal symmetry of the soccer ball or the Buckminister-Fullerene molecule. Coil elements are circular, receive-only loop coils.

Figure 2 shows sensitivity maps from the 32 and 96-channel brain arrays and compares them to the standard 12-channel coil. While the 32 and 96-channel arrays are matched in size, the 12-channel coil employs a larger shell, likely exchanging the ability to accommodate a wider variety of patients with sensitivity. The larger arrays show considerable gains in the cortex with much smaller gains in the center of the head. Nonetheless, the gains in the cortex are substantial, with nearly 10-fold increases in peripheral regions allowing the images of Figs. 3 and 4 which show brain MR images acquired with voxel volumes about 5-fold smaller than conventional acquisitions.

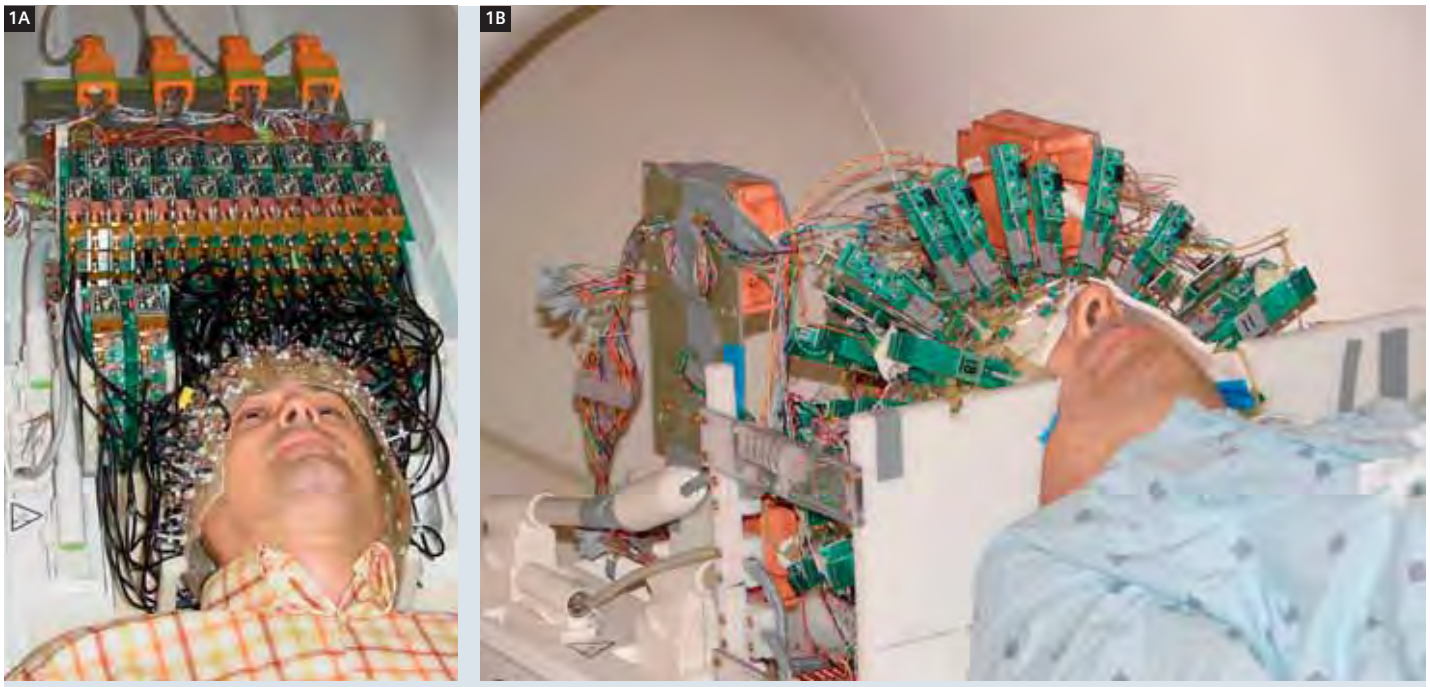

1 Graham Wiggins, one of the authors, tests the 90-channel 1.5T brain array prototype (left) and the 96-channel 3T array prototype (right). The system is a prototype 128-channel MAGNETOM Trio, A Tim System.

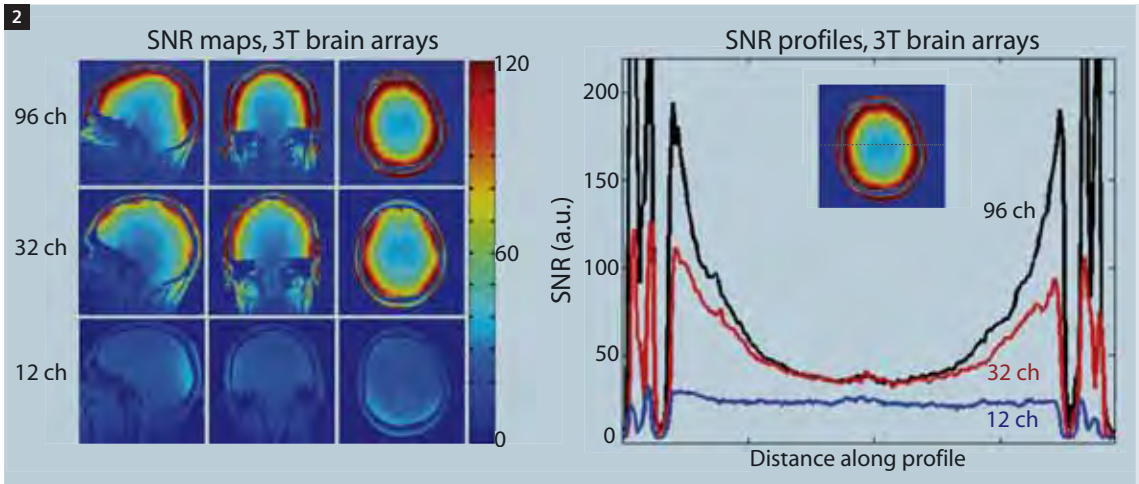

2 Sensitivity comparison of 12, 32 and 96-channel brain arrays at 3T. In the distal cortex, substantial sensitivity improvements are seen as the number of channels is increased.

*Works in progress (WIP). The information about this product is preliminary. The product is under development and not commercially available in the U.S., and its future availability cannot be ensured.

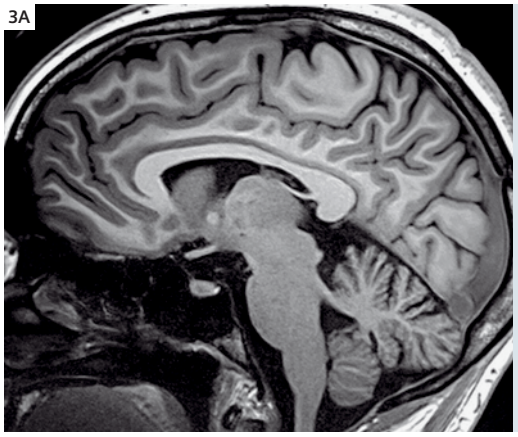

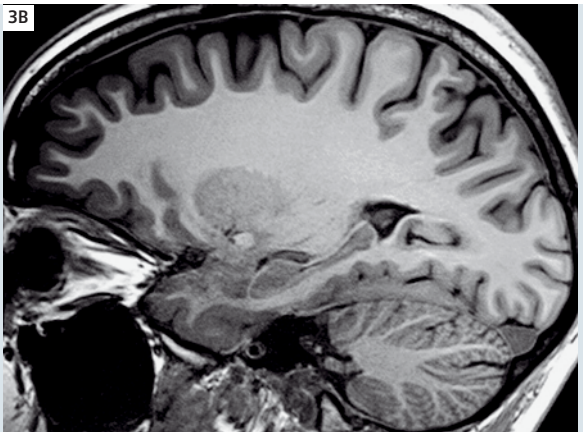

3 3 Tesla MPRAGE with a 32-channel coil (left). 500 µm in-plane resolution with a 1 mm partition thickness.
8 minutes acquisition time.

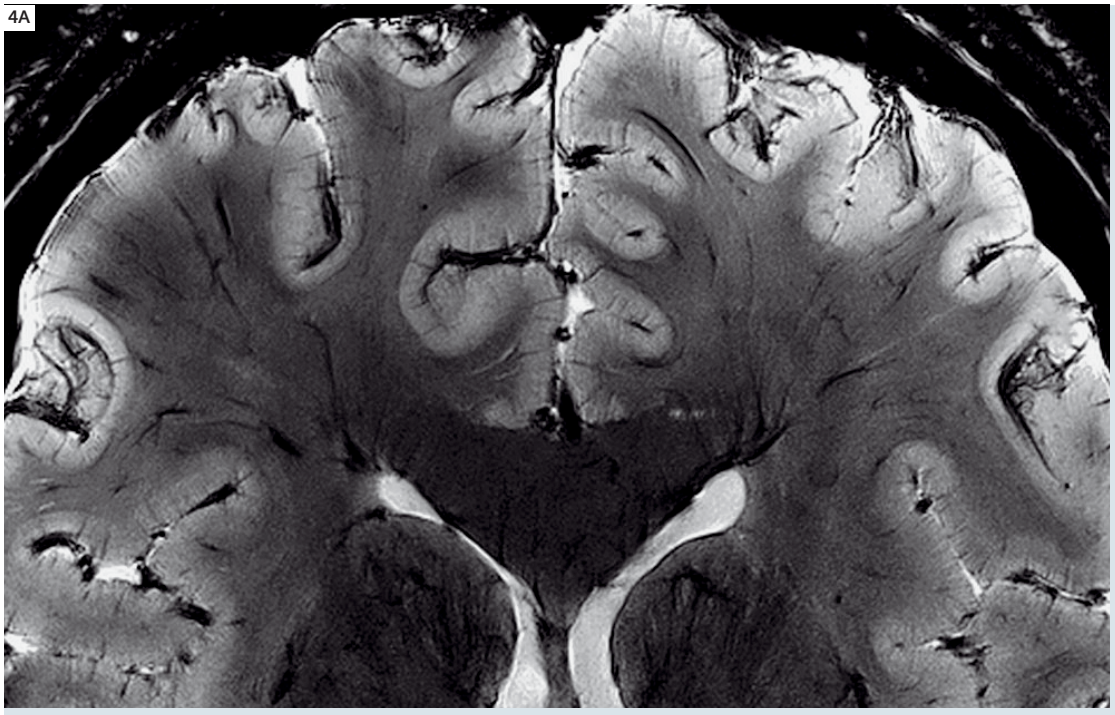

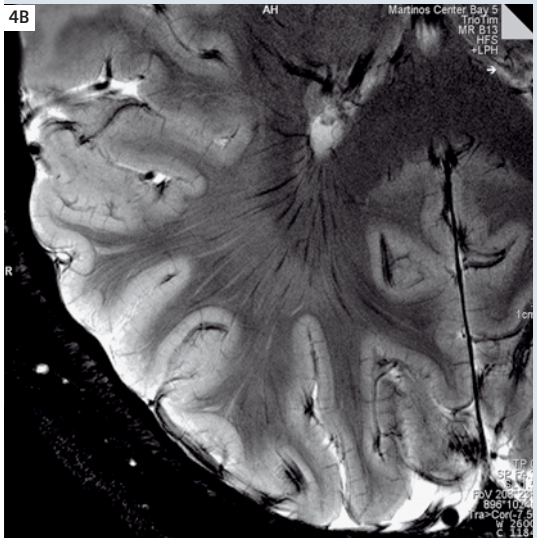

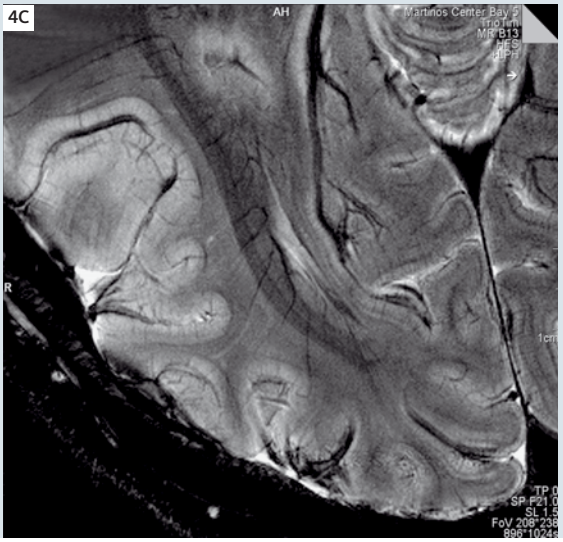

4 7 Tesla T2*-weighted imaging with a 32-channel coil. 220 µm in-plane resolution (1024 matrix) with a 1 mm slice thickness, TR/TE = 500 ms / 25 ms.
8 minutes acquisition time.

g-factor noise penalties for a given acceleration are obtained by measuring the noise correlation matrix (using a noise image acquired with no RF excitation) and coil sensitivity maps in a head shaped phantom [16]. Figure 5 shows the improved ability of the arrays for accelerated imaging. Shown is the percentage of the maximum achievable SNR, a measure related to the g-factor penalty (% SNR = 1/g) for 2 through 6-fold acceleration (conventional iPAT) as well as PAT^2 (acceleration in two phase encode directions) with accelerations up to 20-fold. For the higher acceleration factors, sensitivity gains up to 3-fold are seen (e.g. the R = 5 with 96 channels compared to 12 channels.) For 2-fold accelerations, extremely high accelerations (e.g. R = 4x4) are possible with the 96-channel coil. While the 32-channel coil performs significantly better with acceleration than the 12-channel coils, it still does not appear to truly push the 6x intrinsic limit identified in the ultimate g-factor calculations [3, 4]. The 96-channel array, however, appears to be close to achieving this limit.

5

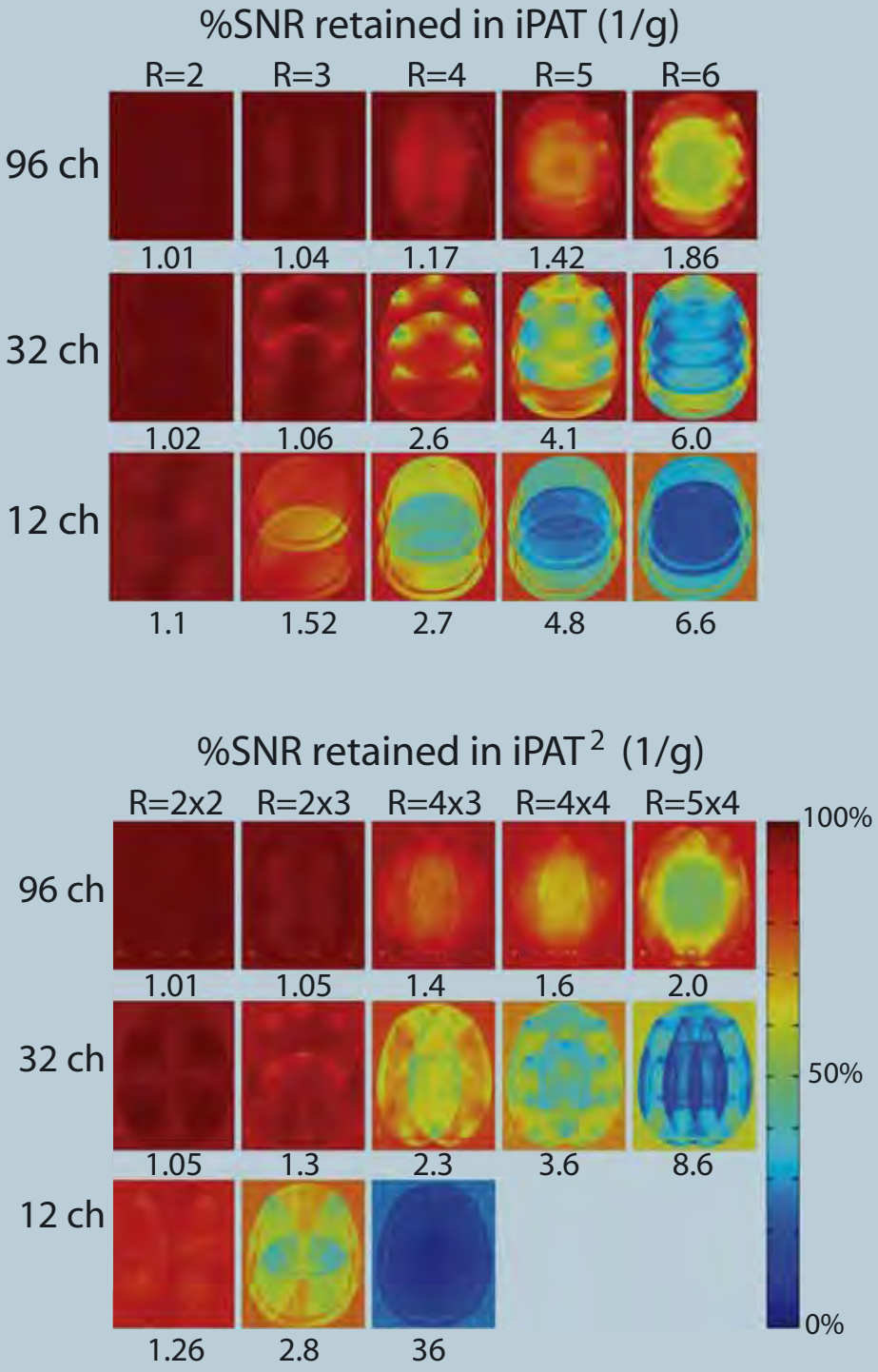

5 g-factor results for 2 thru 6x acceleration for iPAT imaging and R = 2 x 2 thru R = 5 x 4 acceleration for PAT^2. Maps are displayed as 1/g to allow visualization on the same scale. The maximum g-factor in the slice is given below each map. Each increase in the number of elements suggests the potential for an additional step in iPAT acceleration.

* Works in progress (WIP). The information about this product is preliminary. The product is under development and not commercially available in the U.S., and its future availability cannot be ensured.

Figure 6 shows a section of a high resolution 3D FLASH image accelerated 12-fold (3x in one direction and 4x in the other) with the 32-channel 3T coil. The 1 mm spatial resolution volume acquisition was acquired in 1:20 min. Figure 7 shows spin echo EPI (echo planar imaging) acquired at millimeter resolution with single shot encoding to freeze motion. The high acceleration rates which shorten the duration of the EPI readout train help prevent geometric distortion from the susceptibility effects in the frontal lobes as well as preventing significant T2* filtering of the image during the readout.

128-channel array for cardiac MRI

Perhaps no other application has more intrinsic need for improved accelerated imaging than 3D breathhold coronary angiograms. This motivated the extension of the "large N" array concept from brain arrays to cardiac imaging. Our prototype coil (Fig. 8) is closely contoured to the body with a "clam-shell" geometry with 68 posterior and 60 anterior elements of 75 mm diameter and arranged in a continuous overlapped array of hexagonal symmetry to minimize nearest neighbor coupling. The array was designed around accelerated imaging. For example, retaining only a subset of the elements near the heart would have likely produced similar sensitivity for non-accelerated imaging since coil elements distant from the heart contribute little to the SNR. But the accelerated image requires localized coil elements in these areas to assist with unaliasing the accelerated image.

6

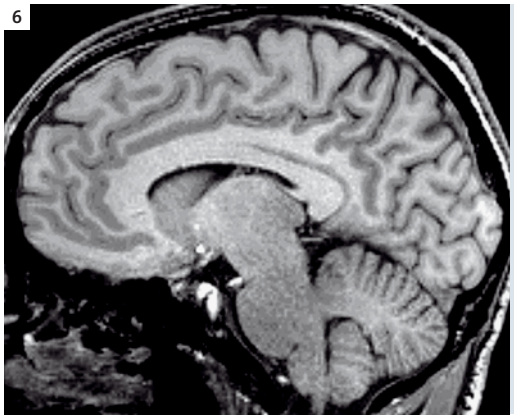

6 A highly accelerated 3D FLASH scan acquired with the 32-channel 3T helmet array. Image was accelerated 12-fold, 4-fold in the in-plane phase encode direction and 3-fold in the thru plane phase encode direction. Image time 1:20 min, image resolution 1 mm isotropic.

7

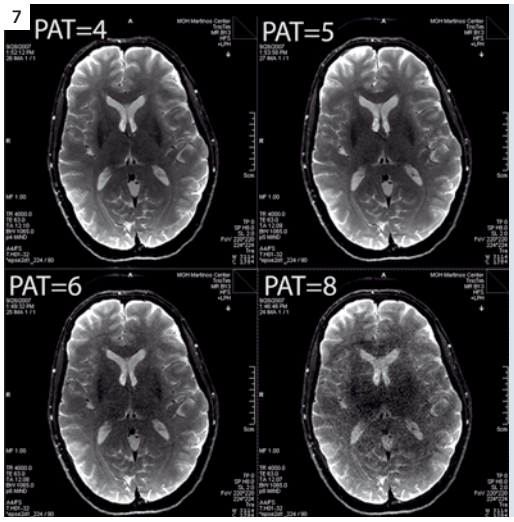

7 Highly accelerated, high resolution single shot spin echo EPI acquired with the 96-channel 3T array. Tolerable artifact and noise amplification for PAT factor up to 6x. SE-EPI, 224 x 224 matrix, 220 mm, 2 mm slice thickness, TR/TE = 4 s/63 ms. Single shot encoding, with but 4 averages.

8

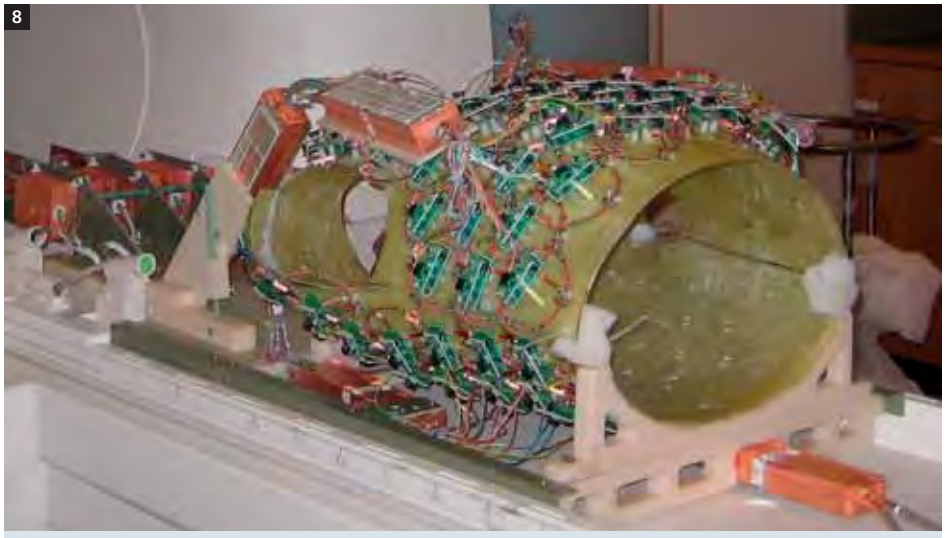

8 Prototype of a 128-channel cardiac coil. Coil is built on a fiberglass former molded to the chest shape of a 180 lbs male. The coil opens "clam-shell" style for patient access. PAT factor up to 6x. SE-EPI, 224 x 224 matrix, 220 mm, 2 mm slice thickness, TR/TE = 4 s/63 ms. Single shot encoding, with but 4 averages.

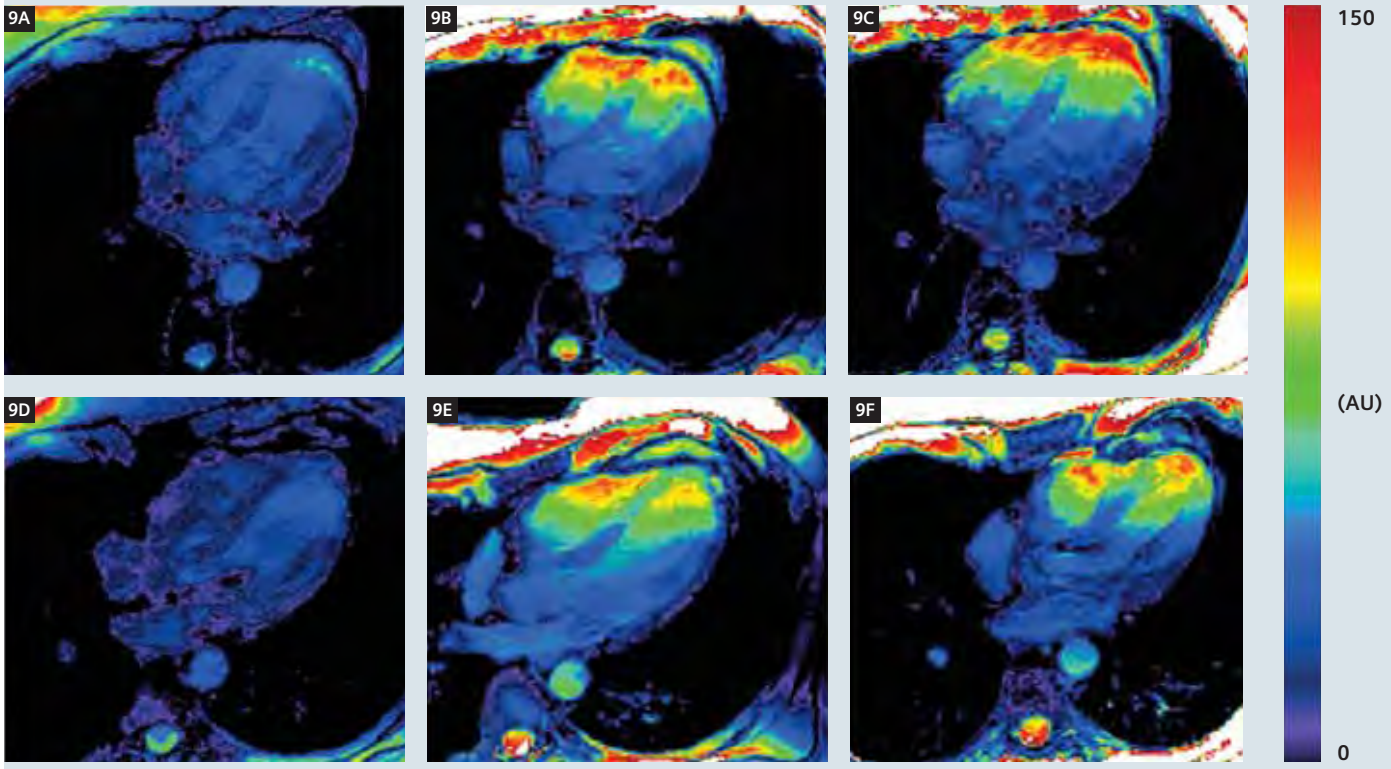

9 SNR in the heart for 24, 32 and 128-channel arrays. The 24 and 128-channel arrays have similar spatial coverage, and the 32 and 128-channel arrays have similar element sizes (and thus similar sensitivity for unaccelerated imaging).

Figure 9 shows SNR maps in the heart with this coil as well as two commercial arrays. Only modest sensitivity improvements are seen relative to the 32-channel coil, which uses similar sized elements (but only covers areas near the heart.) The 128-channel coil distinguishes itself for highly accelerated imaging with maximum g-factor values at higher acceleration factors improved by a factor of 2 or more over that of the 32-channel coil. For example, at rate 5 acceleration in the head-foot direction, the maximum g-factor of the 128-channel coil reached only 1.2, and was 2.5 for the 32-channel coil. Rate 7 acceleration in the left-right direction produced a maximum g-factor value of 1.7 (128-channel array) compared to 3.4 (32-channel array).

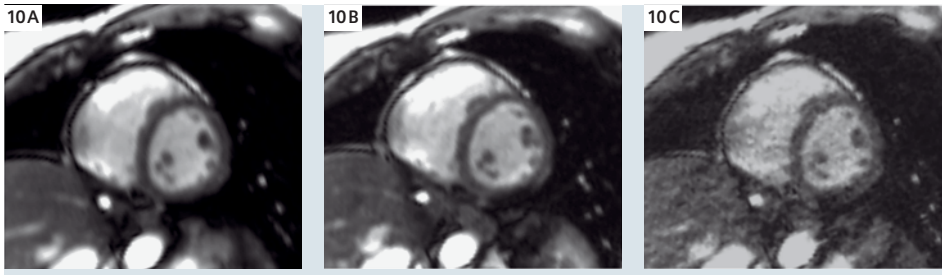

10 High-resolution, highly accelerated 2D cine imaging performed in a female volunteer with the 128-channel cardiac coil. The SSFP cine images shown were acquired with a slice thickness of 6 mm and an in-plane resolution of 1.9 x 2.9 mm. The following acceleration factors were used: **(A)** rate 1, **(B)** rate 4, **(C)** rate 7. The rate 1 and rate 4 images remain almost identical **(A, B)**, and the rate 7 images remain fully diagnostic with well-preserved blood tissue contrast and well-defined fine anatomical features.

* Works in progress (WIP). The information about this product is preliminary. The product is under development and not commercially available in the U.S., and its future availability cannot be ensured.

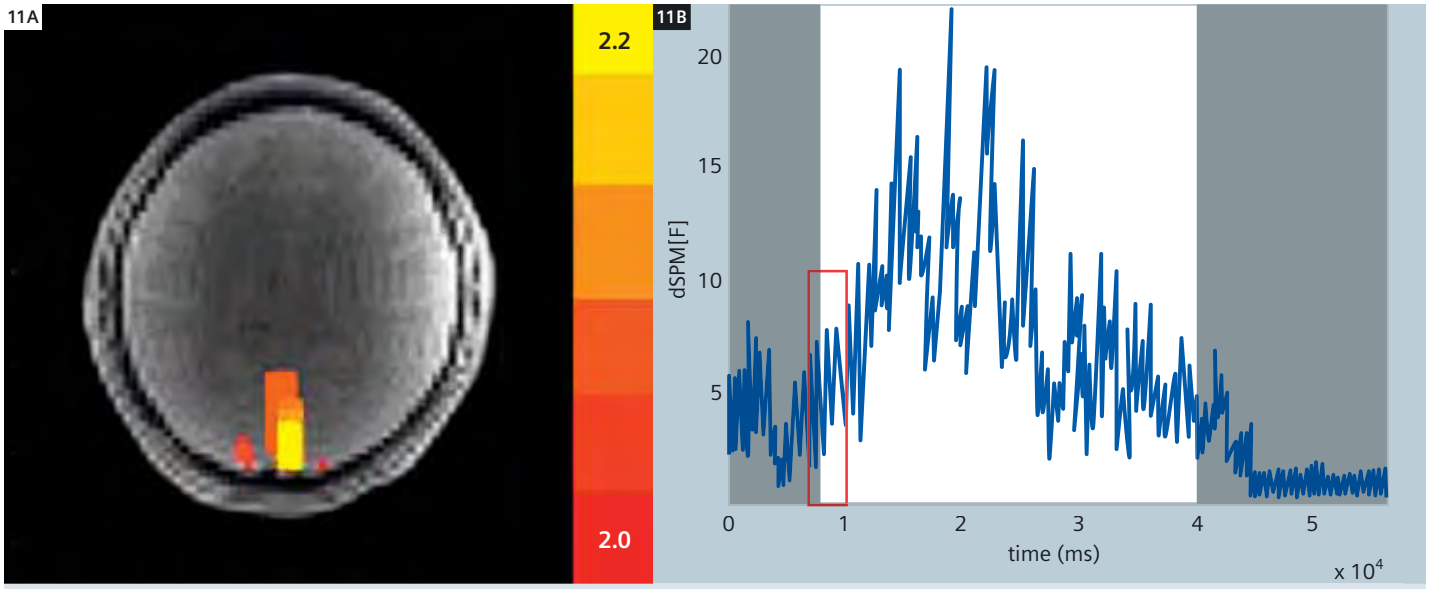

11 InI (MR Inverse Imaging) reconstructed statistical estimates of BOLD visual activation acquired with the 90-channel brain array. Spatial maps (left) and time series of one epoch. Temporal resolution of 20 ms was achieved with a PRESTO sequence and no phase encoding. Modulation at frequencies corresponding to the respiratory and cardiac rates are clearly visible in the time-course.

Result courtesy of FaHsuan Lin, MGH, Boston, USA.

Extreme encoding with large arrays

With current clinical systems (e.g. 32-channel), the reduction of a 10 minute volume scan to less than 1 minute with 12-fold acceleration is possible with modest increase in noise beyond the standard tradeoff between SNR and acquisition time. With even more channels (64 and 96), credible imaging can take place with truly minimal use of the gradients (for example a single readout to form an image). McDougall and Wright constructed a specialized 64-element planar array to demonstrate the potential for very high frame rate imaging acquired with no phase encode steps (e.g. all the information in this direction provided by array localization). Since the imaging is performed in a single readout, they refer to the resulting highly accelerated image as a Single Echo Acquisition (SEA) [9, 17]. Because the readout can be performed in a few milliseconds, frame rates of up to 200 fps were achievable, providing the ability to stop-motion in a paddle wheel phantom rotating at 60 rpm. In addition to illustrating the excellent image quality (considering the 64-fold acceleration and total acquisition time of 8 ms!), their images show the potential for extreme robustness to motion.

MR Inverse Imaging (MR InI)

Using a completely different reconstruction strategy, SEA imaging was acquired in the brain using the 32 and 90-channel brain array described above. The goal was not to detect images per se, but localize the source regions of dynamic change within the brain during functional activation. In this case the goal of the MR image reconstruction resembles MEG/EEG source localization. Here, we seek statistical best estimates of the source locations and associated time courses given the spatial and temporal information available by applying the inverse solution methods used in MEG/EEG source localization. In the example shown in Fig. 8, the temporal information comes from a 50 fps PRESTO sequence acquired with no phase encoding. PRESTO was used at achieve the long TE needed for BOLD fMRI (blood oxygen level dependent functional MR imaging). The spatial information was provided by the readout gradient (L-R direction) and the 90-channel array (A-P direction). Because of the similarity of the reconstruction to the MEG/EEG inverse problem, this approach was called MR Inverse Imaging (MR InI) [18].

Unlike conventional parallel imaging where lack of sufficient spatial information from the array manifests itself as noise amplification (g-factor), the same problem in InI produces reduced ability to spatially localize the changes; namely, a greatly reduced spatial resolution. Here, "sources" refers to the areas of the brain with dynamically altered signal with respect to user defined baseline condition. Since spatial localization is provided in one direction by the array and in the other by conventional frequency encoding, the InI method as implemented is a 1D method with slice select and standard frequency encoding providing the other spatial dimensions. It could potentially be expanded to 2D or even 3D. The 2D case is thus a Single Echo Acquisition, and the 3D case is potentially a single sample of the signal with no use of gradients. For the 90-channel array, the spatial resolution of

the activation localization in the 2D case was 3 mm in the readout direction and estimated to vary from just over 1 cm near the array to about 3 cm deep within the head.

Thus, in the MEG-like inverse problem, the reduced ability of the array to provide spatial information in the center of the head (where the coil profiles are too smooth to provide high spatial resolution information) translates to a deteriorated spatial resolution in these regions. Since the SNR of MR imaging scales as the cube of the voxel dimensions, a small increase in voxel dimensions may make up for reduced spatial encoding accuracy since statistical estimates will be more robust due to the higher signal levels in the larger voxels. Thus the InI method can be viewed as coping with the encoding limitations in the center of the head by adjusting the spatial resolution accordingly. Figure 11 shows the InI reconstructed statistical estimates of the stimulus correlated changes associated with a block design visual stimulus. Also shown is the reconstructed time-course for the activated area. A temporal resolution of 50 frames per second was achieved. At this temporal resolution, many physiological modulations such as the cardiac and respiratory modulations are not temporally aliased (as they normally are) and thus potentially easily removable from the data. Figure 12 shows the extension of the InI method to 3D imaging, here the InI reconstruction is done in the right-left direction and the other spatial directions are encoded with conventional 2D EPI. Thus, in the time it takes to acquire a conventional EPI slice (about 80 ms), the 3D InI method can do whole-head fMRI, improving temporal resolutions as much as 30-fold.

Figure 12 shows visual fMRI acquired at a whole-brain temporal resolution of 10 frames per second. The ability to significantly improve the temporal resolution of fMRI using these extreme parallel acceleration methods offers several exciting possibilities. Firstly, this will be a necessary technology for future attempts to image direct neuronal manifestations of neuronal activation (as opposed to relatively slow and more indirect hemodynamic

12

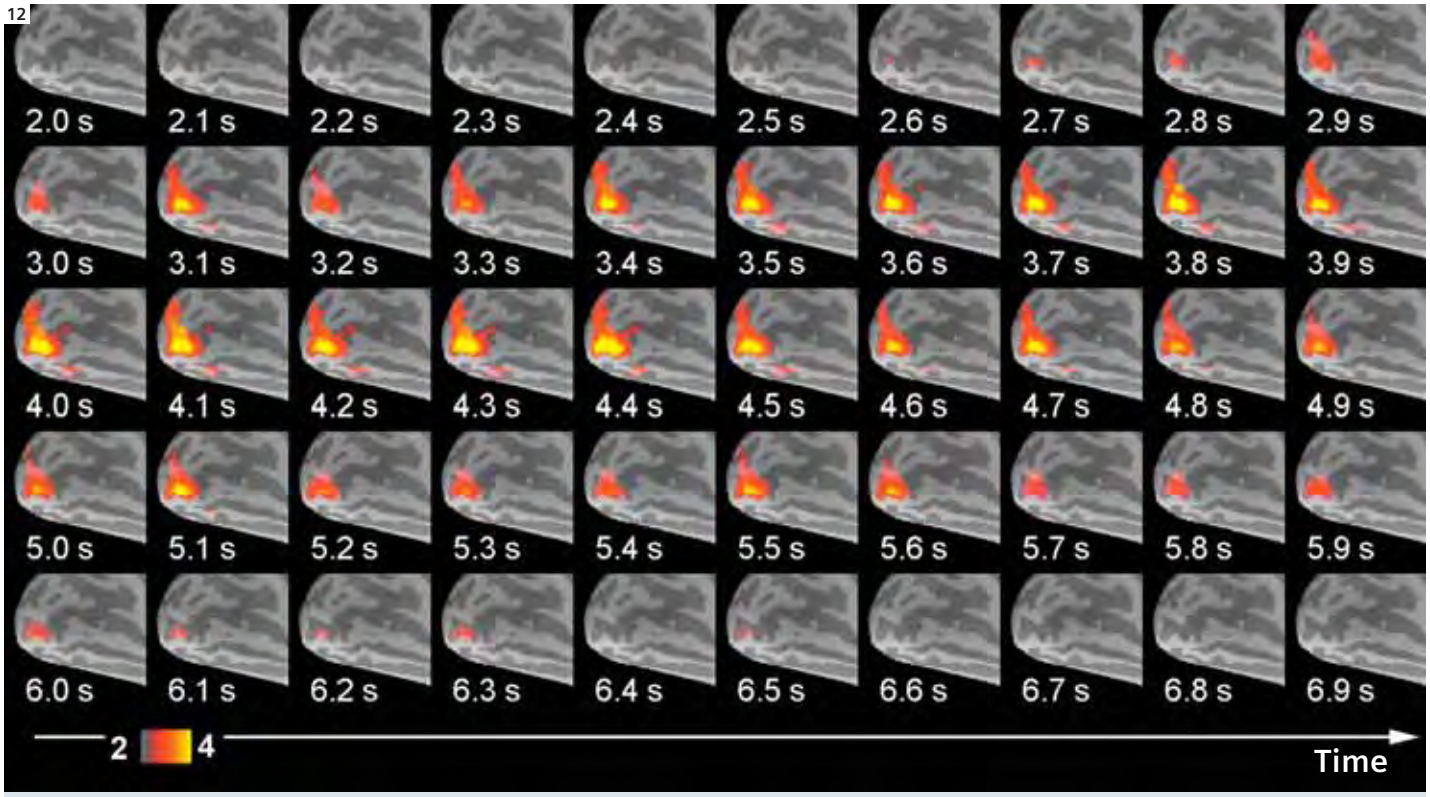

12 3D InI reconstructed statistical estimates of BOLD visual activation across the whole brain at 10 fps. Activation averaged across 5 subjects is shown on a representation of the inflated occipital pole.

Result courtesy of FaHsuan Lin, MGH, Boston, USA.

* Works in progress (WIP). The information about this product is preliminary. The product is under development and not commercially available in the U.S., and its future availability cannot be ensured.

effects.) MEG and EEG show these evoked responses are typically bipolar and of a duration of 30 ms or less. Thus, imaging strategies with order of magnitude improvements in the temporal resolution are needed to unambiguously resolve these events. The ability to temporally resolve significant sources of physiological modulation in the data, such as respiratory and cardiac cycle effects will also improve statistical inference in BOLD fMRI. Finally, with 3D InI there is the potential for truly silent fMRI studies of the auditory system since all gradient waveforms can be eliminated.

Conclusion

While the technical issues of building arrays with large numbers of receive elements are challenging, both the theoretical simulations and the experimental prototypes suggest the potential for substantial benefits, especially for accelerated image encoding. The synergy between large receive arrays, higher field strength systems, and the Tim methodology also suggest that these methods will continue to evolve together in a productive way. This is seen on the theoretical side where the sensitivity gains for accelerated imaging as a function of the number of array elements were seen to improve at higher field and also on the practical side where constructing a small receive coil which is body noise dominated is easier at higher field strength.

Perhaps even more intriguing than being able to substantially improve conventional imaging, is the ability to perform new types of imaging. Realization of this potential is in its infancy but will likely have its first and largest implications for encoding-limited imaging such as high resolution 3D imaging, spectroscopic imaging, and dynamic imaging such as functional imaging.

Acknowledgements

We would like to thank Andreas Potthast, Franz Hebrank and Franz Schmitt of Siemens Medical Systems for their contribution to the large-N brain array and receiver configurations, Melanie Schmitt of MGH who developed the cardiac array, Chris Wiggins of MGH (Currently of NeuroSpin, CEA Saclay France) for his contribution to high resolution 7T studies, and FaHsuan Lin of MGH for results from the inverse imaging reconstruction method. We would like to acknowledge support from the NCRR of the NIH, grant 5P41RR014075-05, the NIH grants 1RO1EB000790 and 1R01EB006847 and the MIND Institute for Mental Illness and Neuroscience Discovery.

References

1 Wright, S.M. and L.L. Wald, Theory and application of array coils in MR spectroscopy. NMR Biomed, 1997. 10(8): p. 394-410.
2 Wiesinger, F., N. DeZanche, and K.P. Pruessmann. Approaching Ultimate SNR with Finite Coil Arrays. in Proceedings of the ISMRM. 2005. Miami FL.
3 Wiesinger, F., P. Boesiger, and K.P. Pruessmann, Electrodynamics and ultimate SNR in parallel MR imaging. Magn Reson Med, 2004. 52(2): p. 376-90.
4 Ohliger, M.A., A.K. Grant, and D.K. Sodickson, Ultimate intrinsic signal-to-noise ratio for parallel MRI: electromagnetic field considerations. Magn Reson Med, 2003. 50(5): p. 1018-30.
5 Ocali, O. and E. Atalar, Ultimate intrinsic signal-to-noise ratio in MRI. Magn Reson Med, 1998. 39(3): p. 462-73.
6 Wiesinger, F., N. DeZanche, and K.P. Pruessmann, Approaching Ultimate SNR with Finite Coil Arrays, in ISMRM 13th Annual Scientific Meeting, presentation 672. 2005: Miami FL.
7 Weiger, M., et al., Specific coil design for SENSE: a six-element cardiac array. Magn Reson Med, 2001. 45(3): p. 495-504.
8 de Zwart, J.A., et al., Design of a SENSE-optimized high-sensitivity MRI receive coil for brain imaging. Magn Reson Med, 2002. 47(6): p. 1218-27.
9 McDougall, M.P. and S.M. Wright, 64-channel array coil for single echo acquisition magnetic resonance imaging. Magn Reson Med, 2005. 54(2): p. 386-92.
10 Zhu, Y., et al., Highly parallel volumetric imaging with a 32-element RF coil array. Magn Reson Med, 2004. 52(4): p. 869-77.
11 Sodickson, D.K., et al., Rapid volumetric MRI using parallel imaging with order-of-magnitude accelerations and a 32-element RF coil array: feasibility and implications. Acad Radiol, 2005. 12(5): p. 626-35.
12 Wiggins, G., et al. A 32 Channel Receive-only Phased Array Head Coil for 3T with Novel Geodesic Tiling Geometry. in Proceed. International Soc. of Magnetic Resonance in Medicine. 2005. Miami FL.
13 Moeller, S., et al. Parallel Imaging Performance for Densely Spaced Coils in Phase Arrays at Ultra High Field Strength in Proceed of the 12th Annual ISMRM meeting. 2004. Kyoto Japan.
14 Cline, H., et al. 32 channel head array for highly accelerated parallel imaging. in Proceedings of the 12th annual meeting of ISMRM. 2004. Kyoto Japan.
15 Wiggins, G., et al. A 96-channel MRI System with 23- and 90-channel Phase Array Head Coils at 1.5 Tesla. in Proceed. International Soc. of Magnetic Resonance in Medicine. 2005. Miami FL.
16 Pruessmann, K.P., et al., SENSE: sensitivity encoding for fast MRI. Magn Reson Med, 1999. 42(5): p. 952-62.
17 McDougall, M.P. and S.M. Wright, Phase compensation in single echo acquisition imaging. Phase effects of voxel-sized coils in planar and cylindrical arrays. IEEE Eng Med Biol Mag, 2005. 24(6): p. 17-22.
18 Lin, F.H., et al., Dynamic magnetic resonance inverse imaging of human brain function. Magn Reson Med, 2006. submitted.

32-Channel Phased-Array Head Coil for 1.5T and 3T

Jörg Stapf

Siemens Medical Solutions, Erlangen, Germany

Introduction

The new 32-channel head coil comes with highly increased signal-to-noise-ratio (SNR) as well as an excellent performance of parallel imaging (iPAT).

New design

The head coil contains 32 elements with 32 integrated amplifiers which are close to the antenna loops in order to minimize signal loss and to achieve a compact design for 1.5T and 3T systems respectively. The housing is separable, the upper part is designed with 12 elements and can be removed for a stand-alone use of the 20 elements lower part, e.g. for highly claustrophobic patients. A comfortable open view has been established for monitoring the peripheral cortex and for visual stimulation experiments included in fMRI examinations.

New features

By reducing the coil size (sensitivity volume) and enlarging the number of coil elements (overlapping of sensitivity volumes) as well as the number of channels the SNR is strongly increased [1]. Compared to the standard 12-channel head coil the SNR of the 32-channel head coil is approx. 20% better at the center of the brain and at least 2-fold better at the cortex (Fig. 2). The 32-channel head coil usable for all kinds of head imaging also with iPAT, but it is especially designed for high resolution imaging, functional MR imaging (fMRI), MR angiography (Fig. 1) and Diffusion Tensor Imaging (DTI).

1

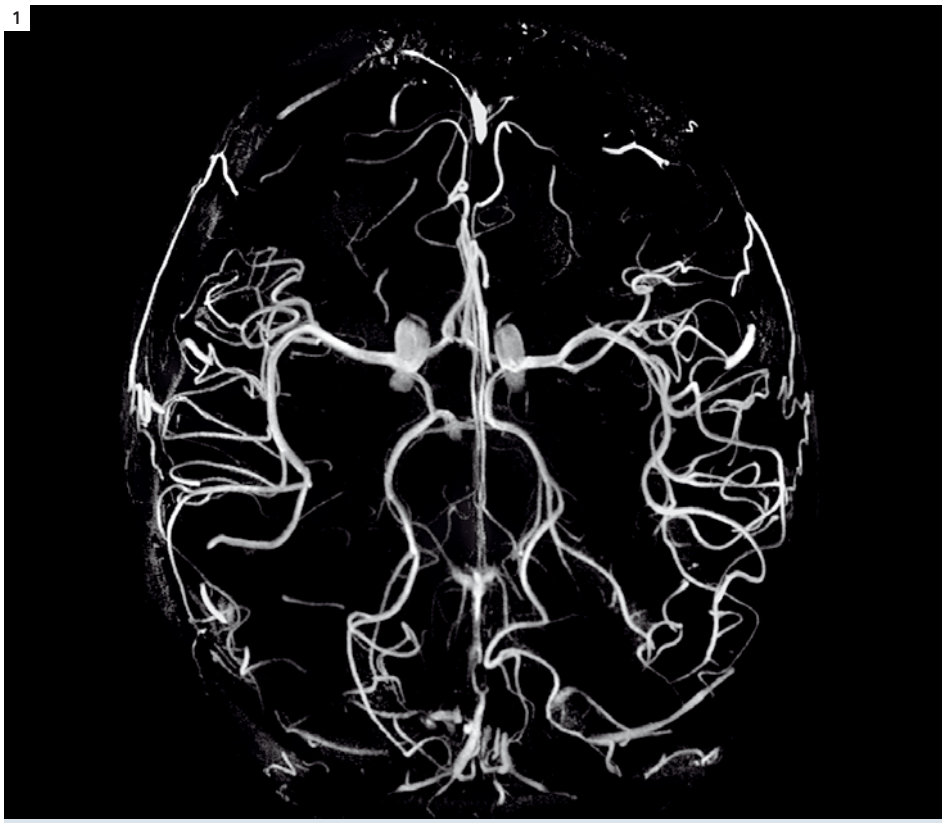

1 3T (MAGNETOM Verio) MR angiography with a 32-channel head coil.

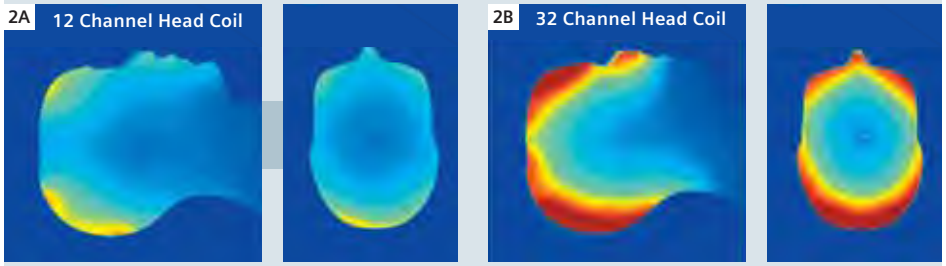

2 SNR distribution of a 1.5T system. **2A** Measurement of a head phantom transversal and sagittal with a 12-channel head coil. **2B** Measurement of a head phantom transversal and sagittal with a 32-channel head coil.

References 1 M.A. Bernstein et al.; Handbook of MRI Pulse Sequences, page 522, 2004, USA.

Open Bore 1.5 Tesla MAGNETOM Espree: Guidance and Monitoring of Radiofrequency Ablation at Liver and Kidney

H. Rempp[1]; S. Clasen[1]; J. Roland[2]; C. Schraml[1]; A. Boss[1]; C. Maier[2]; C. Thomas[1]; P. Martirosian[1]; C.D. Claussen[1]; P.L. Pereira[1]

[1] *University Hospital Tübingen, Department of Diagnostic Radiology, Tübingen, Germany*
[2] *Siemens Medical Solutions, Erlangen, Germany*

Introduction

Liver metastases are a frequent and – with regard to its treatment – complex issue. About 90 % of all hepatic malignancies are metastasis, most of them descending from gastrointestinal tumors, lung cancer and breast cancer [1]. The liver is the most frequent localization for metastases of the colon cancer. The fact that 20 % of patients dying from colon cancer do only have liver metastases shows its prognostic relevance [2-4]. Up to now, surgical resection has been the only curative therapy and is superior to chemotherapeutic treatment, even if chemotherapy is directly applied into the liver through catheters. However, surgical resections on the liver implicate a risk of further morbidity and a mortality rate up to 5 %. Most notably, only 25% of all liver metastases are treatable by surgery, as a predictable incomplete resectability and extrahepatic metastasis are contraindications for surgery. During the last decade, however, various minimally invasive alternative treatment options for non-resectable metastasis have emerged. These include, highly focused ultrasound, laser-induced thermotherapy, microwave, and radiofrequency (RF-) ablation using locally applied heat, aimed at destroying the tumor. Furthermore, these percutaneous thermal therapies may be performed in out-patient care, so patients can often leave hospital one day after the intervention, so that the procedure is less cost-intensive.

Radiofrequency ablation

Alternating electric current, moving with a frequency of 375–480 kHz between two electric poles at a tip of a needle, is the heat source for radiofrequency ablation. In the tissue, the heat is produced by the movement of ions under the influence of a focused electric field at the tip of the probe. RF-systems with one pole at the tip of the needle and the other electric pole at a larger grounding pad on the skin, so called monopolar systems, are distinguished from bipolar systems, where both poles are localized on the needle, only separated by a thin isolation zone. Electric conductivity of the tissue is only preserved, if overheating, drying and carbonization are effectively prevented. Most of the systems, therefore, use an internal water cooling circuit. Radiofrequency ablation produces spherically shaped zones of destroyed tissue which correspond histologically to coagulation necrosis. The necrotic zones remain in the liver, forming scarred tissue and contracting gradually. It must be the aim of a radiofrequency therapy not only including the tumor, but also generating a security zone of necrotic healthy tissue around it. Different strategies have been developed to increase the volume of the ablation zone: Various parallel needles being fixed on a common hand grip, called cluster applicators, achieve larger zones. In addition, extendable needles forming an umbrella-shaped probe configuration have been developed. Another approach was the invention of open perfused systems, which were designed to decrease the tendency of the adjacent tissue to desiccate. In practice, tumors are often larger than the zone that can be produced by a single needle. In this case, various applications have to be performed with the probe being repositioned between the individual application steps. By applying this strategy, several overlapping zones may form a larger, continuous necrotic area including the former tumor and a safety margin at the periphery. It is therefore obvious that imaging has a key function in optimal planning, performing, monitoring and controlling percutaneous radiofrequency ablation.

Imaging

Before an intervention for a cancer patient is planned, the patient should undergo the best imaging available. A precise clinical staging is necessary to choose an

optimally adapted treatment. If a limited number of organs are affected and the lesions are resectable, surgery may be the best option in numerous cases. In other cases irradiation therapy, systemic chemotherapy, a minimal invasive treatment option as the RF-ablation or a combination of these therapies may be optimal. Radiofrequency can be used to treat solid tumors in the lung, the liver and the kidneys or for symptomatic treatments in bone tumors. Best imaging for the ablation of lung and bone tumors allows computed tomography.

For percutaneous treatment of hepatic and renal tumors, different imaging methods are used in clinical practise.

Ultrasound is a cheap, easily available, flexible and fast imaging modality. It allows the visualization of a high number of tumors and can be used as a real-time modality for the placement of a RF-applicator. However, not all tumors can be detected by ultrasound. Especially small lesions, overlaying bowel structures as well as obese patients give a limit to the visualization of hepatic lesions by ultrasound. Beyond that, small gas bubbles, emerging during radiofrequency ablation with vaporization of water, will impede a satisfactory monitoring.

Computed tomography is the standard imaging modality for detailed lung examinations and has become even faster and less radiation intensive with new technologies such as multislice imaging. Nevertheless, the restricted soft tissue contrast may impede a sufficient visualization of the lesion to be treated. For these reasons, the use of magnetic resonance imaging guidance with low field open-architecture scanners was taken up [5, 6].

For interventions at liver and kidney, **MR imaging offers the major advantages** of multiplanar capabilities, high soft tissue contrast, no requirement of iodinated contrast media, and those without ionizing radiation [8]. Moreover, the effects of thermoablative therapies can be monitored and controlled by using T2 and T1-weighted imaging or at high field scanners by directly applying thermosensitive sequences such as the proton resonance frequency method [7], which allows the display of temperature evolution during the therapy.

Table 1: MR advantages

	Ultrasound	Computed Tomography	Magnetic Resonance Imaging
Availability	**easily available,** cheap	easily available	cost-intensive
Time factor	**fast**	**fast**	
Contrast media	not required	iodatet	optional
Visualization of tumor tissue	limited	may be limited to a time window after administration of a contrast agent	**high soft-tissue contras**
Limits	■ obese patients ■ steam bubbles during ablation ■ deep localisation of tumor	allergy to contrast agent	■ pacemaker ■ metallic implants
Thermal effects	not visible	not visible	■ sensitivity to thermal effects ■ monitoring of induced coagualation directly after ablation ■ precise overlapping of coagulation zones ■ control of end point of coagulation ■ prevention of tissue damage
Additional capabilities mapping			**Temperature/Perfusion/Diffusion**
Multiplanar capabilities	online imaging available in one plane	online imaging available in one plane	■ MR-fluoroscopy ■ **precise targeting in 3 planes** ■ 3D visualization of tumor and ablation zone
X-ray exposure	none	**X-ray exposure**	none

Different MR systems

The C-shaped configuration of open low-field MR systems, operating typically at a magnetic field strength in the order of 0.2T, offers easier patient access and surveillance for interventional treatment than classic closed-bore high-field MR systems at 1.5T. Applicator positioning can be monitored by almost real-time fast gradient echo sequences [5]. At low field strength, T2* decay is lower and susceptibility related artefacts are reduced compared to higher field strength, allowing for a better visualization of the tissue adjacent to the metallic applicator. However, low field MR scanners suffer from a low signal yield: As the signal-to-noise ratio (SNR) scales with the magnetic field strength, the signal-to-noise ratio at a 0.2T is less than the seventh part of the SNR at 1.5T. In practise, this effect is less pronounced as changes in the T1 and T2 relaxation time partially compensate for the signal loss. Nevertheless, longer acquisition times and more averages must be planned, without reaching the signal yield of 1.5T imaging. For coronal abdominal imaging which must be performed under breathhold condition to decrease breathing artefacts, reaching a satisfactory image quality is especially challenging. Another problem of low field systems is the decreased T1 relaxation time. For gadolinium based contrast enhanced imaging, the lower T1 contrast must be compensated with a higher dose of the injected gadolinium. Furthermore, at 0.2T, the difference between the resonance frequencies of water and fat is only 30 Hz, preventing the use of spectral fat saturation.

Another disadvantage of C-shaped low-field scanners is the relative temporal and spatial inhomogeneity of the magnetic field which may be a hindrance for the application of thermosensitive sequences. In case of the proton resonance frequency method, a high stability of the magnetic

1

1 Siemens MAGNETOM Espree during radiofrequency ablation of a liver metastasis.

field is required to detect small changes of the proton resonance frequency. Therefore, during abdominal interventions reliable temperature measurement is not feasible due to the combination of a low magnetic field strength, high inhomogeneity of the magnetic field and the presence of metallic applicators.

Interventions at the Open Bore MAGNETOM Espree

With its large bore of 70 cm, the 1.5T magnetic resonance tomograph MAGNETOM Espree facilitates patient access during interventions, performing at the same time faster imaging with a higher signal yield than low field scanners could offer. Instrument placement – e.g. RF-applicator, microwave or cryotherapy probe- and position control can be done fast and almost online by balanced gradient echo sequences (TrueFISP), while the patient can be surveyed during energy application outside or even inside the scanner. Magnetic field stability allows the application of thermosensitive sequences in order to monitor thermoablative intervention.

Planning

Before the decision for a radiofrequency ablation therapy is made, the patient undergoes a thorough staging examination, which not only provides a basis for a multidisciplinary oncological treatment decision but also for the evaluation of the technical feasibility. This includes parameters like the number of lesions to treat, the tumor size and shape, its vascularisation, the vicinity of delicate structures such as bowel, adrenal gland or gallbladder, as well as the planning for the access of the applicator. Multimodal strategies may be appropriate for large lesions, which may be down-sized by neoadjuvant chemotherapy or in the case of hepatocellular carcinoma, where a pre-interventional transcatheter arterial chemoembolisation offers synergistic effects. Size and shape of the tumor have influence on the RF-device chosen. Although therefore in most cases precise pre-interventional abdominal imaging already has been performed, every intervention starts with an integrated standardized planning examination. The selection of an eligible needle track for the applicator is assisted by a grid on the patient's abdomen. After labeling of the puncture site, placement of the biopsy loop coil, disinfection and sterile covering the patient can be placed back into the scanner.

Peri-interventional imaging

Imaging during an intervention has three main functions: targeting, monitoring and controlling. Targeting corresponds to the placement of the RF applicator into the tumor tissue. Monitoring describes the observation of therapy effects during the thermal ablation therapy. Controlling comprises the intraprocedural tools used to regulate the treatment.
The Siemens MAGNETOM Espree facilitates the interactive placement of the RF applicator into the target tissue. Due to the large bore, the placement of the RF probe can be directly performed under MR imaging. A direct viewing of images and a control of the MR scanner is enabled by MR compatible equipment such as a magnetically shielded liquid crystal monitor, an MR compatible mouse, and foot paddles, which can be placed beside the operator.

Targeting

A good visualization of the target tissue, the adjacent anatomic structures and needle tip are preconditions for a safe and effective therapy. MR imaging is capable of delineating delicate structures and tumor tissue without the application of contrast media due to its high soft-tissue contrast. This allows the needle placement without dependence on a short time window after the application of a contrast agent. During the positioning of the probe, two imaging strategies can be used: the position of not moving probes can be controlled by T1-weighted FLASH or T2-weighted HASTE-sequences under breathhold conditions. For sedated patients, these sequences can be applied with respiration triggering. Moving probes can be monitored by fast steady-state free precession gradient echo sequences (TrueFISP) allowing almost real-time imaging of the needle progress onto the target tissue. Due to the free choice of gradient fields, the plane of MR imaging can always be optimized containing the target tissue and the applicator simultaneously. The Interactive Front End (IFE) software integrates the visualization of three selectable planes onto a single screen [11]. It provides both 2D and 3D display and manipulation of images. The images are sequentially updated within 1–3 seconds with an interactive real time sequence. IFE also enables the operator to dislocate and angulate the selected plane interactively as well as to interactively switch between TrueFISP and FLASH sequences. Additionally acquired images can be recorded and used to recover their scan parameters for future scans.
By offering almost real-time spatial information in a condensed way, IFE helps make targeting more smooth and secure, as a time-consuming switching of the image planes is not necessary any more. While intersecting two TrueFISP imaging planes might create artifacts caused by the interferences on the magnetic steady state in areas located in the planes' intersection line, these artifacts can be reduced by an appropriate choice of the image planes and by selecting a repeated imaging of the same plane.

Monitoring

Depending on the size of the tumor to be treated and the number of applicators, targeting aims to place the applicator centrally into the lesion or, if two or more probes are used, beside it in order to inclose it. The challenge of the ablation therapy is to ensure that the entire tumor and a sufficient safety margin on its edges are thermally destroyed. For larger lesions, a strategy to achieve a complete ablation is to perform overlapping ablation zones

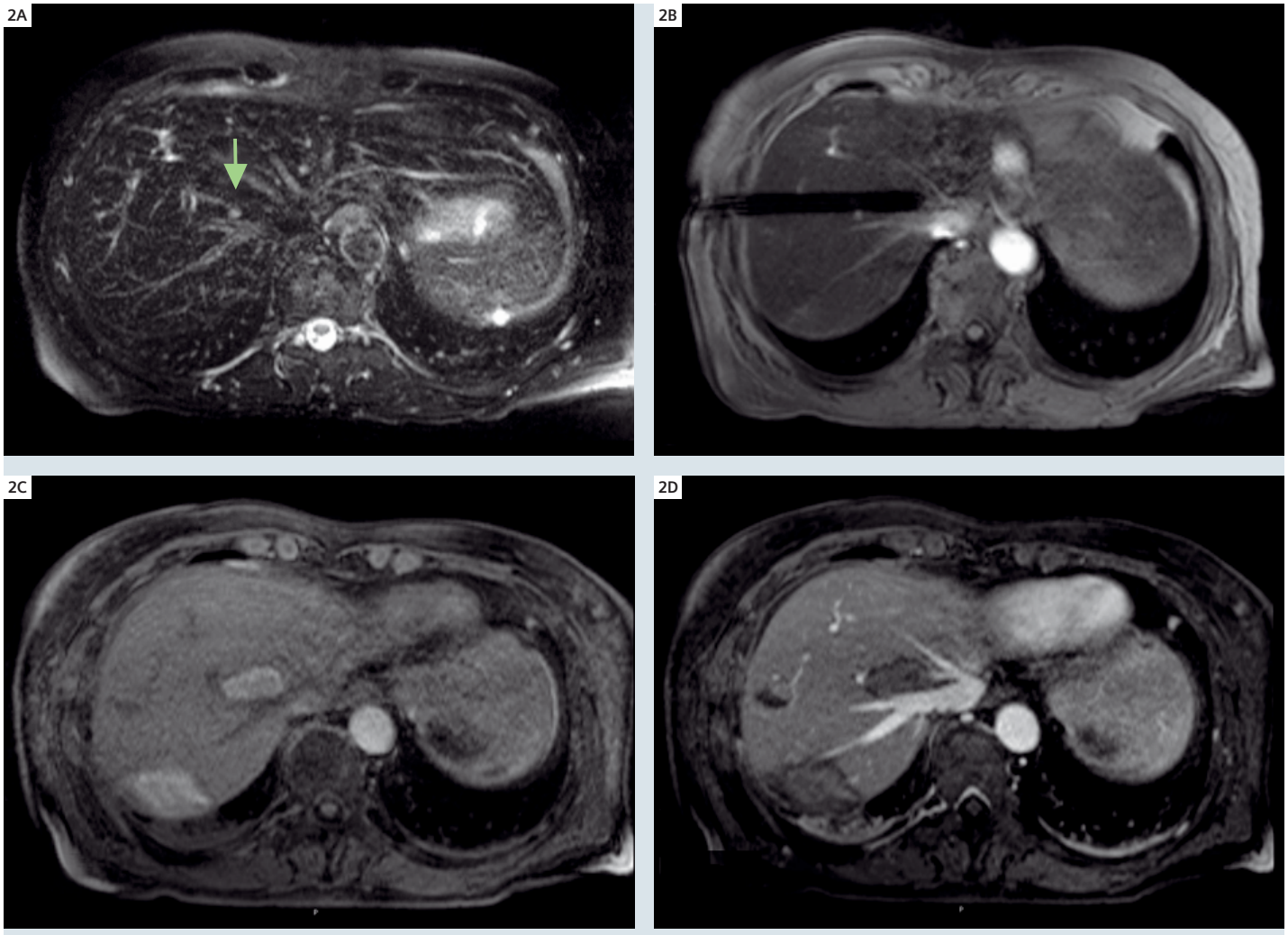

2 **(A):** T2-weighted hyperintense liver metastasis of a colon cancer. **(B):** Placement of the RF applicator **(C):** Post-interventional T1 hyperintense coagulation zone. Another ablation zone is visible below. **(D):** Coagulation zone is not perfused with contrast enhanced imaging.

by relocating the applicator after energy deposition. Tissues resistance to heat considerably varies; furthermore, adjacent vessels may lead to an unwanted cooling of the target volume. The unpredictable reaction of the tissue and the sometimes complex geometrical situation between the different applicator positions make a monitoring of the therapy effects indispensable.

Due to its sensitivity to thermal effects, high field MR is superior to other imaging modalities concerning the display of therapy effects during radiofrequency ablation. Necrotic tissue shows reduced water content and can be identified due to its well-delineated hypointense appearance on T2-weighted images [9]. On T2-weighted images, the ablation zone is characterized by a zonal structure. The former needle track is filled with a proteinaceous, extracellular fluid which appears as a centrally located thin hyperintense line on the T2-weighted images. The T2-weighted hypointense ablation zone is limited at its outer rim by a hyperintense margin which histologically corresponds to a zone of transition between the necrotic area and normal parenchyma. It is characterized by a reactive hemorrhagic reaction, the presence of red blood cells, liver cells in process of degeneration and an interstitial edema [10]. T2-weighted images are suitable to estimate the size of the necrotic area, as a possible overestimation of the induced coagulation has been shown to be less than 2 mm [10]. STIR and T1-weighted images tend to underestimate the induced coagulation, which appear as a hyperintense zone on them, whereas T1-weighted contrast enhanced images, which the show a non-enhancement, lead to a slight overestimation (up to 4 mm) [12]. Gadolinium enhanced images, however, cannot be repeated randomly as the contrast media has to be cleared from organism first. The contrast between the tumor and the

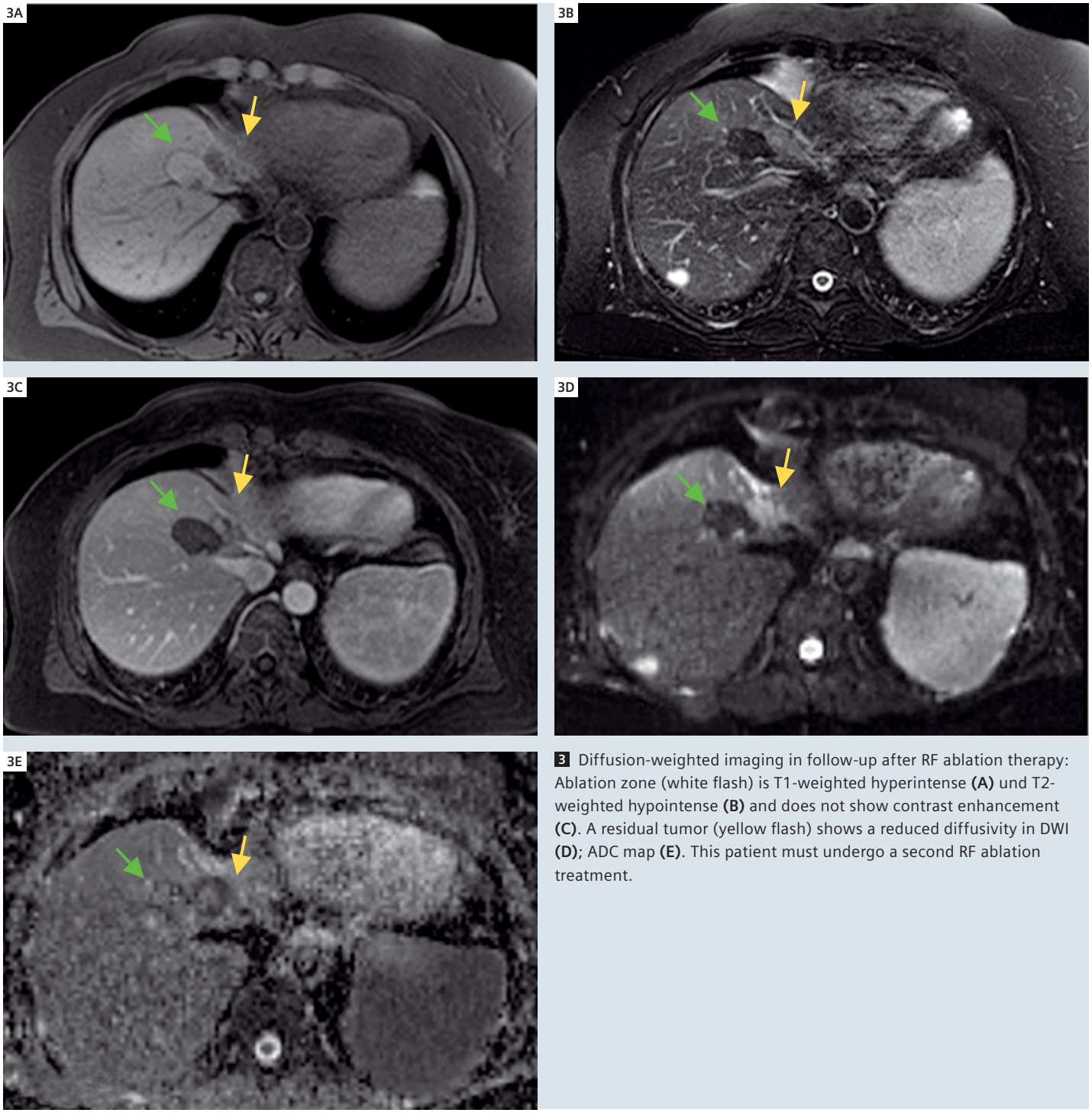

3 Diffusion-weighted imaging in follow-up after RF ablation therapy: Ablation zone (white flash) is T1-weighted hyperintense **(A)** und T2-weighted hypointense **(B)** and does not show contrast enhancement **(C)**. A residual tumor (yellow flash) shows a reduced diffusivity in DWI **(D)**; ADC map **(E)**. This patient must undergo a second RF ablation treatment.

coagulated area is optimal in T2-weighted and STIR images, which are therefore useful to detect residual tumor areas after RF ablation. In conclusion, T2-weighted images are most useful for characterizing the necrotic area and for detecting possibly remaining tumor areas (Fig. 2).

Controlling

Beside the different T1 or T2-weighted images, other options to control energy application do exist. The generators used for the energy deposition may offer the possibility to check temperature and impedance. Temperature is typically measured by a thermometer placed at the tip of the needle. An estimation of the induced coagulation can be established based on the information about temperature persisting over a certain period of time at the centre of the zone. Impedance measurements rely on the fact that

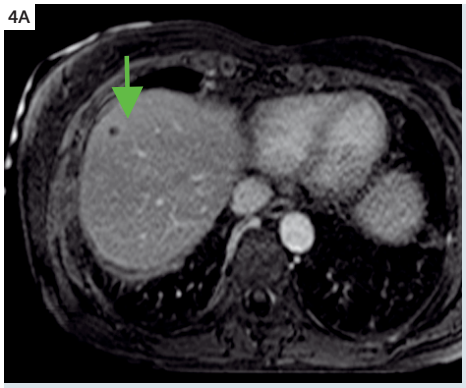

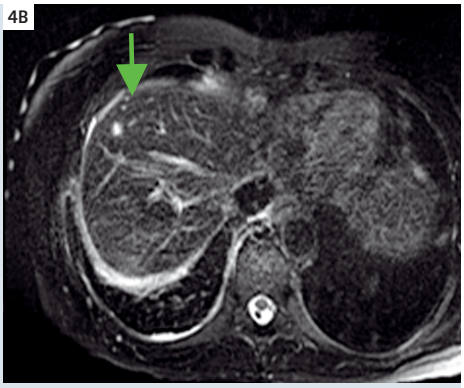

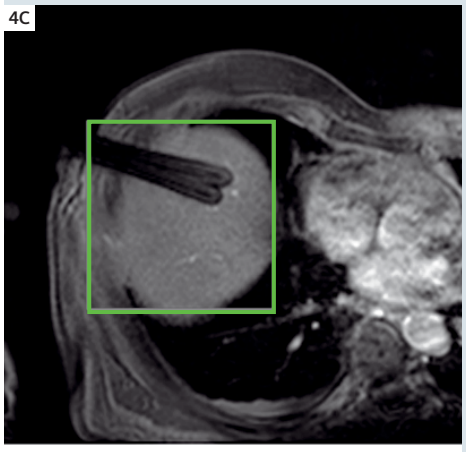

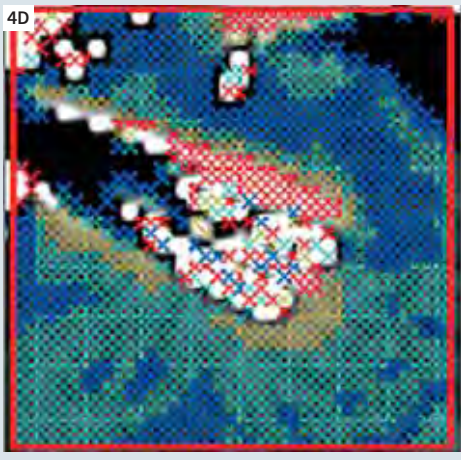

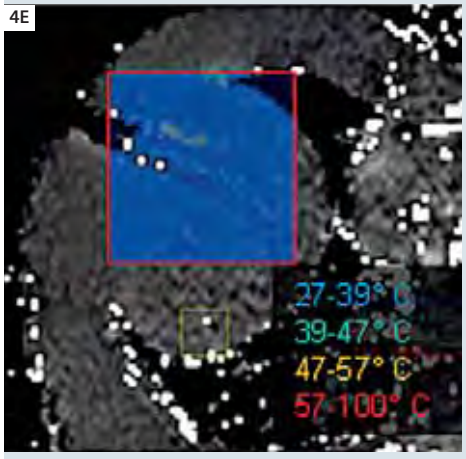

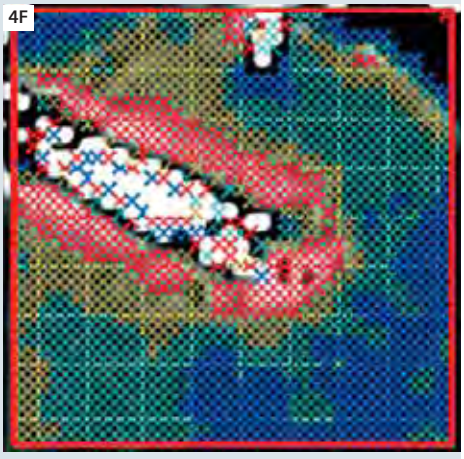

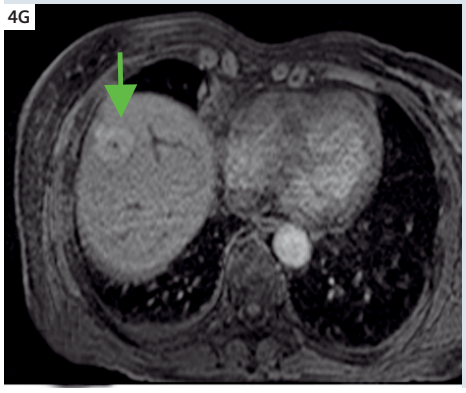

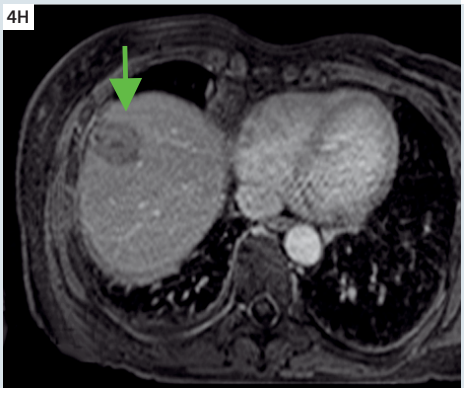

the water content in the target tissue decreases in the course of radiofrequency ablation. Lower water content scales with higher electric resistance. The impedance information given by commercially available RF systems can thus be used to evaluate the progress in coagulation [13]. However, monitoring size and shape of the coagulated zone is only feasible by imaging.

Magnetic resonance imaging offers more than the mere spatial information about the coagulated zone. With high field scanners, thermometric and functional imaging become feasible and clinically applicable. In delicate situations, these sequences may allow the use of radiofrequency ablation without taking risks.

Diffusion-weighted imaging

Due to recent technical developments, diffusion-weighted imaging (DWI) of the abdomen has become possible in clinical routine. In DWI, image contrast is determined by the thermally induced motion of water molecules, called Brownian motion. This random motion in applied field gradients leads to incoherent phase shifts resulting in signal attenuation [14]. Thus, DWI allows for characterization of biological tissue on the basis of its water diffusion properties determined by the microstructural organization, cell density and viability of the studied tissue [15]. Therefore, DWI may be useful in the detection of thermally-induced tissue necrosis and offer valuable diagnostic possibilities both in controlling and in the follow-up imaging of RF ablation (Fig. 3).

4A-4C Metastasis in upper part of the liver with T1-weighted hypointense and T2-weighted hyperintense signal (white flash).
4D-4F Multipolar applicator placement and thermometry reference image with proton resonance frequency shift method. Enlarged: Temperature development during RF ablation.
4G, 4H Coagulation zone after treatment (white flash).

MR-temperature mapping

MR temperature monitoring with modern MR scanners benefits from the opportunity of combining online anatomical and temperature information in one image, thus allowing for the protection of tissue nearby the heated area which is in danger of heat necrosis, such as the heart or the intestine. Several physical properties that can be measured by MR can be used to perform a temperature measurement by applying different techniques. 2D or 3D temperature maps can be derived from measuring the thermal diffusivity, performing single voxel spectroscopy, using temperature sensitive contrast agents, and measuring the spin-lattice relaxation time T1 or the proton resonance frequency shift (PRF). The PRF method is currently the most commonly used temperature sensitive MR technique [16]. It has been demonstrated to be tissue independent [17] for all water protons. The method is based on a change of proton's Larmor frequency which scales with a temperature change. This variance is attributed to a changing shielding of the electrons in water molecules due to the changes in the strength and length of the hydrogen oxygen bond. Temperature changes can be calculated by subtracting phase images acquired before and after a temperature change. Temperature mapping is susceptible to artifacts due to the low order of the temperature coefficient (10−8/°C) and interfering factors such as body movement, respiration, and metallic applicators. Fast sequences – using parallel imaging or EPI-techniques – and trigger schemes have been established to overcome the motion artefacts (Fig. 4).

Arterial Spin Labeling (ASL) for renal perfusion study

RF ablation is also a convenient therapy option in case of malignancies of the kidneys, such as renal cell carcinomas. The MR-guided intervention may for instance be useful in the case of older patients with comorbidities not allowing for a surgical treatment. As the kidneys are highly perfused and the differentiation between residual tumor and liquid deposits or a minor hemorrhage after ablation is difficult, additional monitoring and controlling may be useful. As contrast-enhanced T1-weighted perfusion imaging may be performed only once during treatment because the contrast-medium requires several hours for clearance from the blood stream, spin-labeling perfusion imaging may be an alternative for perfusion assessment of the tumor and the coagulation necrosis. In the spin labeling technique, blood water is used as an endogenous tracer allowing for arbitrary repetitions of perfusion assessment. Spin labeling perfusion imaging is performed using a FAIR-TrueFISP technique [18, 19]. This technique works with magnitude images recorded after slice selective or global inversion, respectively. An adiabatic inversion RF FOCI (frequency offset corrected inversion) pulse is used for slice-selective inversion. Perfusion images are generated by subtraction of the images with selective and global inversion.

One of the greatest advantages of RF ablation compared to surgical resection is that it can be performed in several ablation cycles until completeness of tumor coagulation is achieved, which can be visualized by a non-perfused zone. Therefore, the spin labeling technique seems most favorable as monitoring modality.

In addition to spin-labeling perfusion imaging, 3D spoiled gradient echo sequences in good image quality may be acquired during one breathhold allowing for the implementation of a MR urography protocol for depiction of the ureter. In RF ablation of renal cell carcinoma, the ureter is especially in danger in case of treatment of a lesion at the lower pole of the kidney, which typically has a close anatomical relationship to the ureter.

Post-interventional imaging

The response of the ablation therapy must be assessed by post-interventional imaging and is a compulsory part of the oncological aftercare, which normally also comprises regular extrahepatic imaging, clinical examinations and laboratory tests, depending on the primary tumor. Both, excellent contrast between possible residual tumor areas and the coagulated zone and the best comparability to the prior interventional images make MR a good choice in oncological aftercare imaging. Residual tumors and new metastasis appearing in a formerly healthy part of the liver can be assessed by a second radiofrequency ablation therapy, if a multidisciplinary team indicates the therapy.

Clinical results

Reports in literature about the clinical application of percutaneous RF-ablation under MR-guidance are much fewer in number than reports about the treatment under ultrasound or CT-guidance. The feasibility of RF-ablations under MR-guidance have been demonstrated and can be performed by low-field open-architecture MR-systems as well as with closed-bore MR systems operating at 1.5T [21]. The low number of publications and the still limited follow-up period make a comparison of different image modalities guiding the RF therapy difficult. Furthermore, it has to be considered that patient selection will not be consistent as the repartition of imaging capacities and patient's complexity will differ with the size of the performing medical centre. The clinical experience in the application of MR-guided RF-ablation is summarized in Table 1.

Table 1: Clinical experience

Author	Year	Patients (n)	Sessions (n)	Magnetic field strength	Tumors (n) (HCC/Met.)	Tumor size (cm)	Follow-up (months)	Major complications	Complete coagulation
Lewin	1998	NA	NA	0.2T	6 (0/6)	NA	NA	0	NA
Kelekis	2003	4	6	0.23T	8 (3/5)	2.0 (1.2-2.4)	4.4 (1-9)	0	7/8 (88 %)
Huppert	2000	11	22	0.2T	16 (2/14)	2.3 (1.3-3.0)	11.8 (3-18)	0	14/16 (87 %)
Kettenbach	2003	26	33	0.2T	48 (15/33)	2.9 (0.6-8.6)	NA (1-2)	4/26 (15 %)	18/35 (51%)
Aschoff	2000	8	NA	0.2T	19 (0/19)	NA	NA	NA	NA
Mahnken	2004	10	10	1.5T	14 (1/13)	3.3 (2.0-4.7)	12.2 (1-18)	NA	13/14 (93 %)
Gaffke	2006	8	9	1.5T	12 (0/12)	2.4 (1.0-3.2)	7 (4-9)	0	12/12(100 %)

Conclusion

MR-guided radiofrequency ablation is a safe and effective minimally invasive therapy in the treatment of primary and secondary malignancies of the liver as well as renal cell carcinoma. Multiplanar imaging, a high soft-tissue contrast and the possibility of fluoroscopy facilitate targeting and monitoring. Open-bored high field scanners like the 1.5T Siemens MAGNETOM Espree combine the advantages of interventional low field scanners such as good patient access with fast and high-contrast imaging available only at high field scanners. Interactive capabilities and special software and hardware equipment like a shielded monitor and condensed image representation with the IFE tool help the operator. Therapy controlling may be simplified with special imaging sequences allowing for instance real-time temperature measurement. Consequently, larger tumors necessitating precise repositioning of the applicator and controlling of overlapping ablation zones can be approached, while faster and due to the better imaging safer treatments may increase clinical results and therefore interdisciplinary acceptance.

References

1 Abrams HL, Spiro R, Goldstein N: Metastases in carcinoma. Cancer 3 (1950) 74–85.

2 Jaffe BM, Donegan WL, Watson F et al.: Factors influencing survival in patients with untreated hepatic metastases. Surg Gynecol Obstet 127 (1968) 1–11.

3 Goslin R, Steele G, Zamcheck N et al.: Factors influencing survival in patients with hepatic metastases from adenocarcinoma of the colon and rectum. Dis Colon Rectum 25 (1982) 749–754.

4 Stelle G, Ravikumar TS: Resection of hepatic metastases from colorectal cancer: biologic perspective. Ann surg 210 (1989) 127–138.

5 Lewin JS, Connell CF, Duerk JL, et al. Interactive MRI-guided radiofrequency interstitial thermal ablation of abdominal tumors : clinical trial for evaluation of safety and feasibility. J Magn Reson Imaging 1998;8(1): 40–7.

6 Kettenbach J, Kostler W, Rucklinger E, et al. Percutaneous saline-enhanced radiofrequency ablation of unresectable hepatic tumors: initial experience in 26 patients. AJR Am J Roentgenol 2003;180(6): 1537–45.

6 Ishihara Y, Calderon A, Watanabe H, A precise and fast temperature mapping using water proton chemical shift. Magn Reson Med. 1995 Dec; 34(6):814-23.

7 Mahnken AH, Buekcer A, Spuentrup E, et al. MR-guided radiofrequency ablation of hepatic malignancies at 1.5 T: initial results. J Magn Reson Imaging 2004; 19(3): 342–8.

8 Graham SJ, Bronskill MJ, Henkelman RM. Time and temperature dependence of MR parameters during thermal coagulation of ex vivo rabbit muscle. Magn Reson Med 1998;39(2):198–203.

9 Lazebnik RS, Breen MS, Lewin JS, Wilson DL. Automatic model-based evaluation of magnetic resonance-guided radio frequency ablation lesions with histological correlation. J Magn Reson Imaging 2004; 19(2):245–54.

10 Lorenz CH et al. Proc. ISMRM w.

11 Merkle EM, Boll DT, Boaz T, et al. MRI-guided radiofrequency thermal ablation of implanted VX2 liver tumors in a rabbit model: demonstration of feasibility at 0.2 T. Magn Reson Med 1999; 42(1): 141–9.

12 Pereira PL, Trübenbach J, Schenk M, et al. Radiofrequency ablation: in vivo comparison of four commercially available devices in pig livers. Radiology 2004; 232(2): 482–90.

13 Colagrande S, Carbone SF, Carusi LM, Cova M, Villari N. Magnetic resonance diffusion-weighted imaging: extraneurological applications. Radiol Med (Torino) 2006; 111:392–419.

14 Naganawa S, Kawai H, Fukatsu H, et al. Diffusion-weighted imaging of the liver: technical challenges and prospects for the future. Magn Reson Med Sci 2005; 4:175–186.

15 Hindman JC. Proton resonance shift of water in the gas and liquid state. J Chem Phys 1966; 44:4582–4592.

16 Cline HE, Hynynen K, Schneider E, et al. Simultaneous magnetic resonance phase and magnitude temperature maps in muscle. Magn Reson Med. 1996 Mar;35(3):309–15.

17 Quesson B, de Zwart JA, Moonen CT. Magnetic resonance temperature imaging for guidance of thermotherapy. J Magn Reson Imaging. 2000 Oct;12(4):525–33.

18 Martirosian P, Klose U, Mader I, Schick F. FAIR True-FISP perfusion imaging of the kidneys. Magn Reson Med. 2004;51:353–361.

19 Boss A, Martirosian P, Schraml C, Clasen S, Fenchel M, Anastasiadis A, Claussen CD, Pereira PL, Schick F. Morphological, contrast-enhanced and spin labeling perfusion imaging for monitoring of relapse after RF ablation of renal cell carcinomas. Eur Radiol. 2006; 27:1–11.

20 Clasen S. et al. Eur J Radiology. Magnetic resonance imaging for hepatic radiofrequency ablation. 2006; 140–148.

21 Clasen S, Boss A, Schmidt D, Schraml C, Fritz J, Schick F, Claussen CD, Pereira PL. MR-guided radiofrequency ablation in a 0.2-T open MR system: Technical success and technique effectiveness in 100 liver tumors. J Magn Reson Imaging. 2007 Sep 25;26(4):1043–1052.

Listen – Discuss – Share
6th MAGNETOM World Summit

May 29 – June 1, 2008 in Munich, Germany

We invite you to join our community of Siemens MR users worldwide to the 6th MAGNETOM World Summit in Munich, Germany.
The positive feedback from 5 previous events is proof that the meeting is an ideal opportunity to meet other members of the MAGNETOM World, to develop contacts and to exchange valuable information.

You can attend a wide spectrum of presentations to help keep you on the edge of new trends in MR.
- Hear about best practices and clinical trends from the world's leading experts
- Learn advanced techniques and innovative solutions
- Exchange ideas and knowledge with other MAGNETOM users

The MAGNETOM World Summit will take place at the Sofitel Hotel Bayerpost, right next to the central railway station in the middle of Munich.
Even though Munich, the capital city of Bavaria, is Germany's third largest city, it is called *"Weltstadt mit Herz"* (metropolis with a heart). Located on the river Isar north of the Alps it is right in the middle of some of the most beautiful scenery in Europe. The city features beautiful architecture and a cultural scene that is second to none. World famous however, is its annual Oktoberfest, *d'Wiesn* as the locals call it.
Munic is home to everything quintessentially Bavarian. Besides its breweries it is well-known for *Weißwurst*, a breakfast sausage, *Schweinsbraten mit Knödeln und Kraut* (roased pork with dumplings and cabbage) or *Leberkässemmeln* (an untranslatable specialty you will have to try.) These delicacies are often served in the beergardens. During the evening events we will present to you the traditional Munich as well as the modern city that is celebrating its 850th birthday this year.

We look forward to seeing you there!

For more information and to register, please visit

www.siemens.com/magnetom-world

Munich, Germany

The 6th MAGNETOM World Summit is sponsored in part by Bayer Schering Pharma AG, Berlin, Germany and by IMRIS, Manitoba, Canada.

Bayer HealthCare
Bayer Schering Pharma

IMRIS

"Dynamic" Time-Resolved Large FoV 3D MRA*

Alex Frydrychowicz, M.D.; Mathias Langer, M.D.; Jürgen Hennig, Ph.D.; Michael Markl, Ph.D.

Department of Diagnostic Radiology and Medical Physics, University Hospital Freiburg, Germany

Introduction

Contrast-enhanced MR-angiography (ce-MRA) has largely influenced angiographic diagnostics throughout the past two decades[1]. Despite recent reports about contrast agent side effects ce-MRA remains a safe and easy procedure. With its high sensitivity and specificity towards clinically relevant pathologies it has evolved to a reference standard which is in large parts supported by its straightforward applicability and widespread availability.

Improvements in MR hard- and software technology over the last 10–15 years have provided image sampling strategies such as parallel imaging [2], view sharing [3, 4], and partial Fourier transform which are beneficial for magnetic resonance (MR) image acquisition. As correct bolus timing and short sequences due to the limited breathhold capabilities of individual patients are prerequisites to ce-MRA which is based on fast T1-weighted imaging, ce-MRA benefits largely from the combination of modern image acceleration methods to fast acquisition schemes. Comprehensively added to standard gradient echo sequences, improvements in temporal and/or spatial resolution can be reached. Consequently, if acquisition time and spatial resolution are kept to constant values, the temporal updated rate can be increased and allows for dynamic angiographic imaging.

Dynamic or rather time-resolved contrast-enhanced 3D MR-angiography (tr-ce-MRA) is easy to use in clinical routine since no additional bolus timing and time-consuming sequence adjustments are necessary. In addition, tr-ce-MRA techniques provide an excellent separation between arteries and veins. In addition, "dynamic"

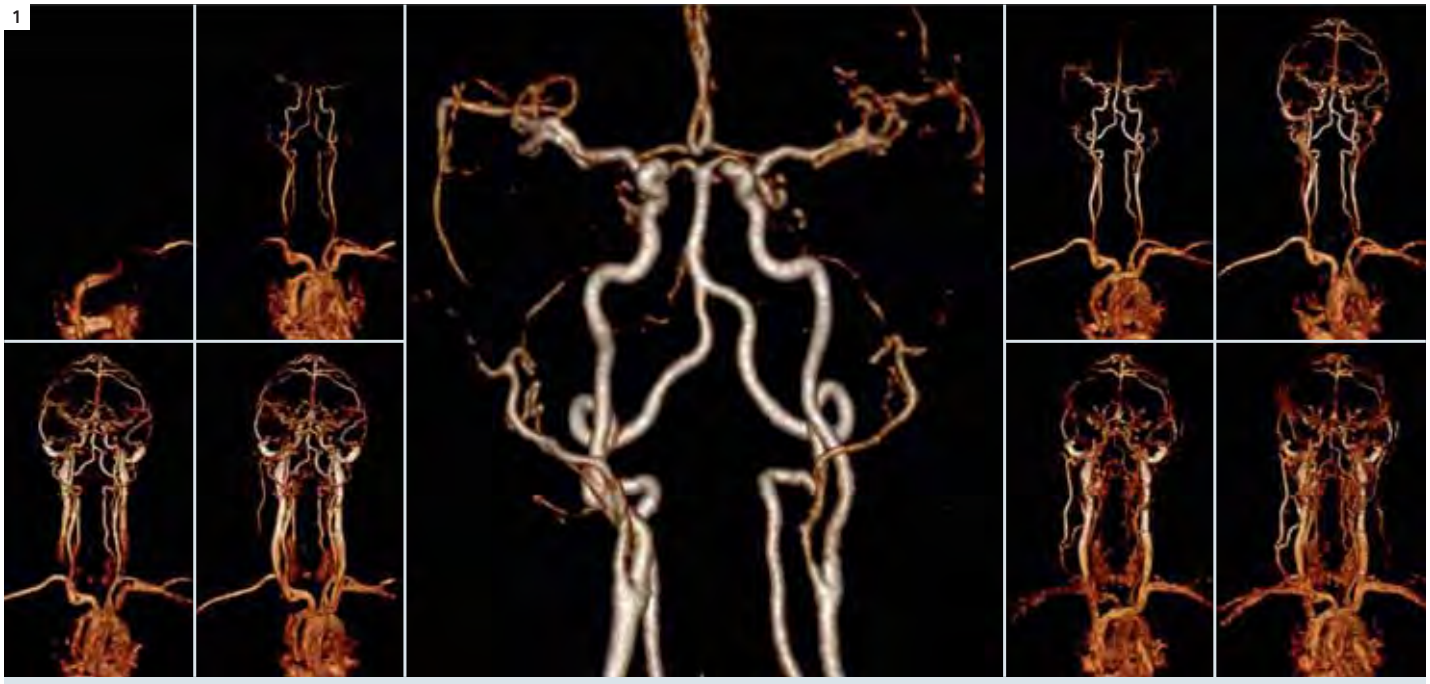

1 Large FoV time-resolved ce-MRA in craniocervical imaging provides information on arterial vasculature as well as venous filling in this patient with suspected thrombosis of the left jugular veins which was excluded. Also, additional information about other vascular territories is available, e.g., arterial filling of the left and right carotid arteries and the circle of Willis.

information about contrast agent distribution over time can be gathered "for free" (Fig. 1). This can be appreciated as the reason why this technique is constantly gaining influence in daily routine especially in imaging of the thoracic vasculature. In thoracic MR-angiography, a good separation of arteries and veins is crucial to diagnosis especially in intitial or follow-up examinations of congenital cardiovascular diseases. Although the currently achievable temporal update rates in the order of seconds do not permit true sub-second hemodynamic analyses which are at still subject to multidimensional phase contrast imaging, the clinical applications of tr-ce-MRA are widespread and focus on the pulmonary vasculature [5], thoracic and cerebral vessels. Applications include clinical questions such as pulmonary embolism, arterio-venous malformations and the vascular anatomy. Additionally, the dynamics of contrast material distribution can be used e.g, for pulmonary perfusion studies [6], in search of arterio-venous malformations, shunts or steal phenomena in high-grade stenoses (Fig. 2). Further, it can aid the diagnosis and facilitate the discrimination of true and false lumen in dissection (Fig. 3). Time-resolved sampling schemes such as dynamic projection angiographies and 3- dimensional (3D) sampling schemes have been presented as early as 1996 for routine scanning at 1.5 Tesla [7]. The more recent introduction of modern high-field scanners promises a further gain in signal-to-noise ratio (SNR). Especially in fast T1-based contrast-enhanced ce-MRA this can be exploited as the decrease of T1 relaxation times and thus enhanced T1 shortening effect of (Gd-) gadolinium-based-contrast agents enables for preservation of SNR despite shorter acquisition periods.

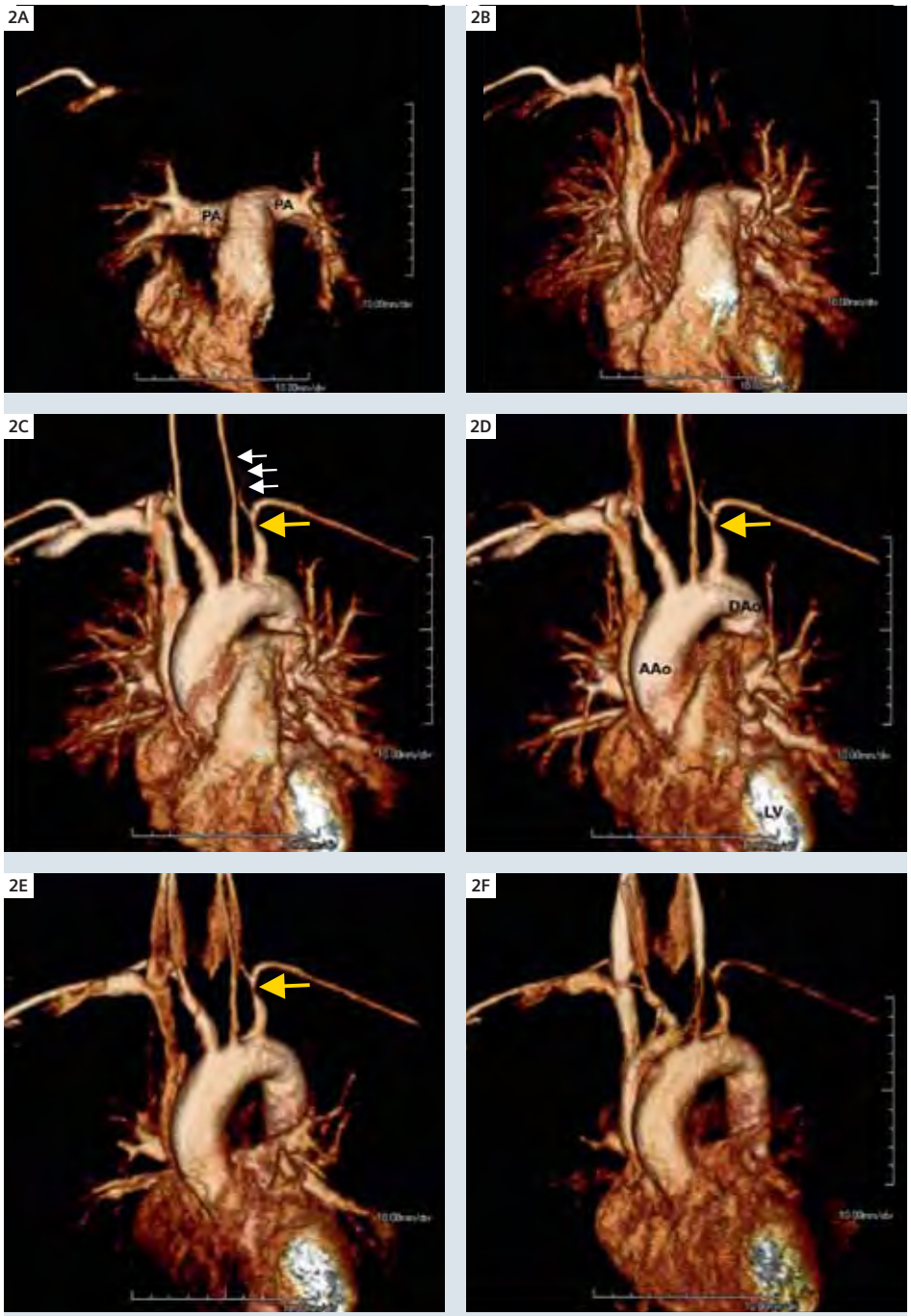

2 Volume rendered time-resolved MR-angiography underlines the quality of images which can be reconstructed easily in 3D. Furthermore, this patient with a relevant left sided stenosis of the proximal subclavian artery (yellow arrow) shows instant filling of the left vertebral artery indicating that a subclavian steal phenomenon can be ruled out (white arrows).

3 Representative images from time-resolved large FoV MRA in a patient with Type-A-dissection after surgical repair of the ascending aorta. Next to the clear delineation and diagnostic capability with respect to the exclusion of local insufficiencies or aneurysms, true and false lumen of the dissection can clearly be differentiated by their diverse temporal contrast behavior.

We provide an overview of the technique by focussing on large field-of-view (FoV) applications. These are of interest to clinicians since a large number of routine protocol settings depend on the administration of contrast material but do not focus on the first-pass imaging characteristics. By adding a single sequence in the order of 1 minute scan time, an additional large FoV angiography can be gained for free at virtually no cost for the patient and the diagnosing physician.

How does it work?

Image acquisition is based on a standard angiography technique i.e., rf-spoiled 3D gradient echo sequence. In order to permit data acquisition with an acceptable spatial resolution as well as a temporal update rate in the order of 2.0–3.5 seconds, several image acceleration procedures are combined to generate a useful time-resolved 3D ce-MRA protocol for neurovascular imaging (cranial and cervical vessels) as well as the depiction of the thoracic angiography (thoracic aorta and branching vessels).

First, parallel imaging (k-space based GRAPPA reconstruction [2]) with an acceleration factor of up to four along the phase encoding direction is employed. In addition, partial Fourier acquisition along the phase and slice encoding direction (for both, partial Fourier factor = 6/8) permits a further reduction of the scan time needed for the acquisition of an entire 3D data volume. Further, view sharing strategies along the temporal domain (such as *syngo* TWIST or TREAT imaging, see also figure 4) based on elliptical centric view ordering, double update rate of central k-space and sharing of outer k-space regions is added to the imaging protocol [3, 8]. As a result, the effective temporal resolution can <be improved by a factor of 1/3 without compromising the spatial resolution of the individual 3D data volumes [9].

How do we perform time-resolved ce-MRA

Since time-resolved ce-MRA at 3T is fast and easy to perform, it can easily be attached to virtually any contrast enhanced MR imaging protocol in which vascular pathologies are of interest. Thoracic MRA is routinely performed using a standard 8-channel or 12-channel phased-array surface coil. Sagittal oblique or coronal data volumes can be used likewise dependent on the individual patient's anatomy. A dedicated 8-channel phased-array neurovascular coil or a combination of standard Tim Head and Neck Matrix coils can be

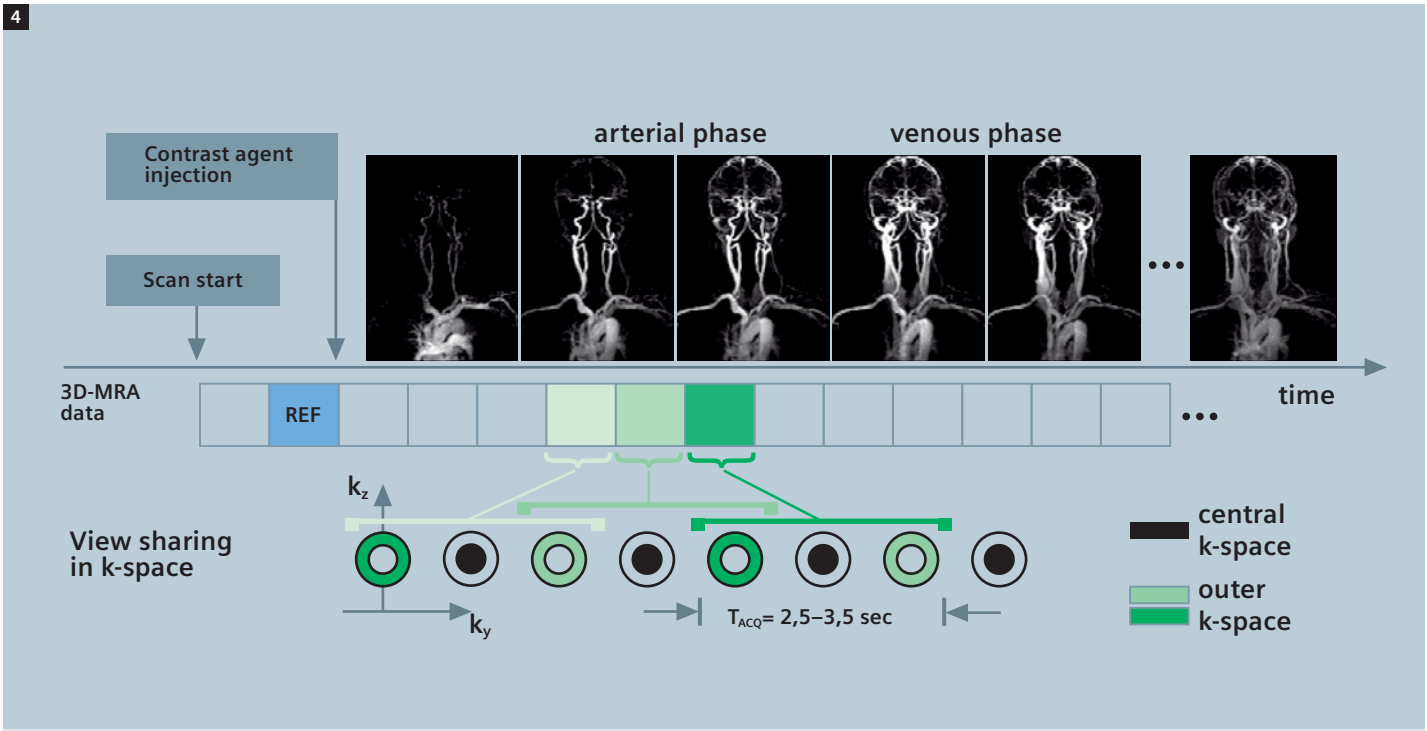

4 Data acquisition and image acceleration strategies for time-resolved ce-MRA. Following the scan start, contrast agent is administered after the acquisition of two precontrast 3D data sets. Subsequently acquired 3D MRA data sets depict the dynamics of the passage of the contrast agent bolus as illustrated in the time series of maximum intensity projections reflecting arterial and venous phases of the contrast agent distribution within the vascular system. The effective update rate of the MRA data is increased using temporal view sharing in the ky-kz space as shown for three successive time frames (gray shaded squares). Background subtraction was performed using the pre-contrast data set indicated by REF.

Table 1: Typical scan protocol parameters for large FoV time-resolved ce-MRA

Application	TE / TR [ms]	FoV [mm] (read/phase)	Matrix (read/phase)	Slices/ partitions	Spatial res. [mm] (read/phase/slice)	Flip angle	Parallel imaging
Thoracic MRA	0.8 / 2.0	coronal 400 x 400 sagittal 400 x 300	320 x 160	64	coronal 1.3 x 2.5 x 2.2 sagittal 1.3 x 1.9 x 2.2	15-25	GRAPPA accel. factor = 4 24 ref. lines
Craniocervical MRA	1.0 / 2.3	coronal 400 x 320	384 x 192	64	1.0 x 1.7 x 2.0	15-25	GRAPPA accel. factor = 4 24 ref. lines

used for craniocervical scans. Typical scan parameters are summarized in table 1. With the resulting imaging protocol 20–30 T1-contrast 3D data volumes are acquired consecutively with a temporal update rate of 2.5-3.3 s. ce-MRA is performed using intravenous gadolinium contrast agent.

As a result of the high temporal update rate no individual assessment of bolus arrival time is needed and contrast agent injection can simply be started after the completion of the acquisition of the first two 3D data volumes (approximately 6 seconds following the initiation of data acquisition). To avoid transient effects, the second data volume is typically used as a full resolution precontrast data set for background signal elimination through mask subtraction. For a schematic illustration of scan and injection timing see figure 1.

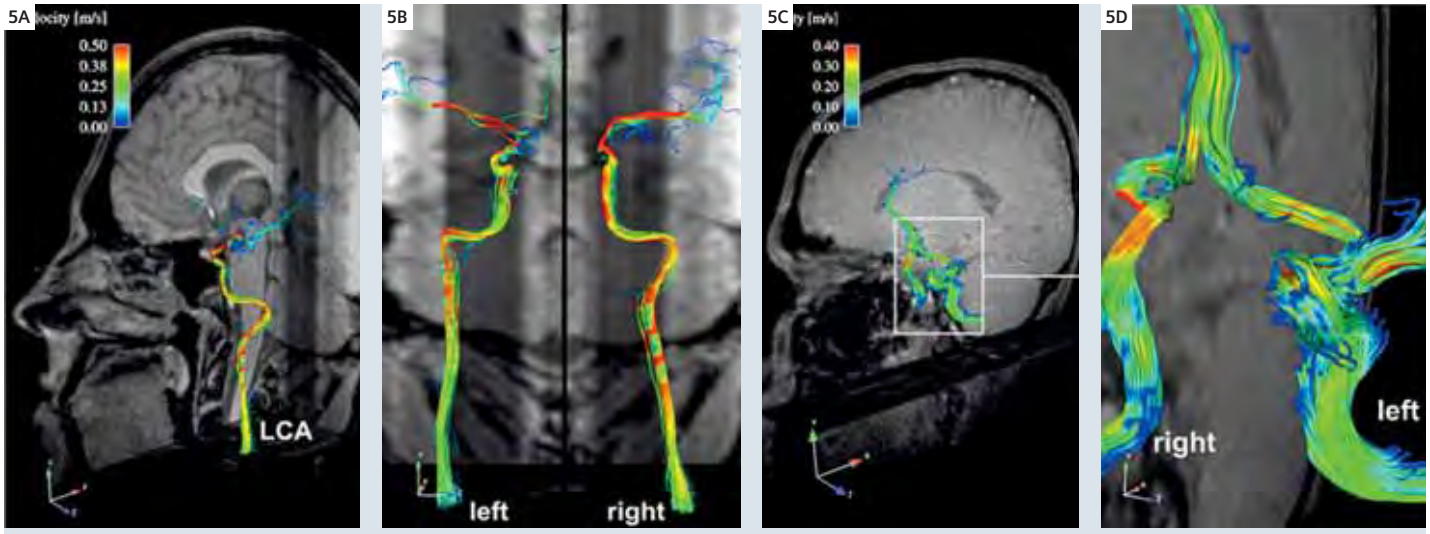

5 True "dynamic" information on blood flow can be gathered by "4D" phase contrast MRI (time-resolved 3D acquisitions with flow encoding for all three spatial directions). Images were acquired on a Siemens MAGNETOM Trio and reveal blood-flow characteristics directly acquired in the extra- and intracranial carotid arteries. Flow velocities and directions are directly measured and displayed color-coded with respect to the actual flow velocities. Note that no simulation of the in-vivo data is necessary.

Conclusion

Time-resolved 3D contrast-enhanced MR-angiography with imaging acceleration along both the spatial encoding direction and temporal domain offers a sound tool to clinicians for everyday routine. Its major advantage derives from the easy to use protocols which allow for MR angiography with every application of contrast agent in approximately 60 seconds of examination time during free breathing. Without the necessity for a bolus timing, MRA can be performed in demanding situations such as impaired cardiac output, large contrast agent dilution volumes such as in aneurysms and may offer additional information on the detected pathologies. Novel applications exploiting the sensitivity of the MR signal to blood flow are currently emerging that permit further insights into the true hemodynamic conditions of entire vascular systems. Recently reported applications of such a technique called flow-sensitive 4D MRI have demonstrated its potential for the detailed assessment of the effect of vascular pathologies on local and global time-resolved 3D blood flow (Fig. 5) but are at present limited to research application at a few worldwide centers [10, 11].

*Some of the concepts and information presented in this paper are based on research and are not commercially available in the U.S.

References

1 Prince MR, Narasimham DL, Jacoby WT, et al. Three-dimensional gadoliniumenhanced MR angiography of the thoracic aorta. AJR Am J Roentgenol 1996;166(6):1387-1397.
2 Griswold MA, Jakob PM, Heidemann RM, et al. Generalized autocalibrating partially parallel acquisitions (GRAPPA). Magn Reson Med 2002;47(6):1202-1210.
3 Fink C, Ley S, Kroeker R, Requardt M, Kauczor HU, Bock M. Time-resolved contrast-enhanced three-dimensional magnetic resonance angiography of the chest: combination of parallel imaging with view sharing (TREAT). Invest Radiol 2005;40(1):40-48.
4 Wilman AH, Riederer SJ, King BF, Debbins JP, Rossman PJ, Ehman RL. Fluoroscopically triggered contrast-enhanced three-dimensional MR angiography with elliptical centric view order: application to the renal arteries. Radiology 1997;205(1):137-146.
5 Nael K, Michaely HJ, Kramer U, et al. Pulmonary Circulation: Contrast-enhanced 3.0-T MR Angiography – Initial Results. Radiology 2006;240(3): 857-868.
6 Fink C, Bock M, Puderbach M, Schmahl A, Delorme S. Partially parallel threedimensional magnetic resonance imaging for the assessment of lung perfusion-initial results. Invest Radiol 2003;38(8): 482-488.
7 Korosec FR, Frayne R, Grist TM, Mistretta CA. Time-resolved contrast-enhanced 3D MR angiography. Magn Reson Med 1996;36(3):345-351.
8 Wilman AH, Riederer SJ. Performance of an elliptical centric view order for signal enhancement and motion artifact suppression in breath-hold three-dimensional gradient echo imaging. Magn Reson Med 1997;38(5):793-802.
9 Frydrychowicz A, Bley TA, Winterer JT, et al. Accelerated time-resolved 3D contrastenhanced MR angiography at 3T: clinical experience in 31 patients. Magma 2006;19(4):187-195.
10 Markl M, Harloff A, Bley TA, et al. Time-resolved 3D MR velocity mapping at 3T: improved navigator-gated assessment of vascular anatomy and blood flow. J Magn Reson Imaging 2007;25(4):824-831.
11 Wigstrom L, Ebbers T, Fyrenius A, et al. Particle trace visualization of intracardiac flow using time-resolved 3D phase contrast MRI. Magn Reson Med 1999;41(4):793-799.

Listen – Discuss – Share
6th MAGNETOM World Summit

May 29 – June 1, 2008
in Munich, Germany

We invite you to join our community of Siemens MR users worldwide to the 6th MAGNETOM World Summit in Munich, Germany.
The positive feedback from 5 previous events is proof that the meeting is an ideal opportunity to meet other members of the MAGNETOM World, to develop contacts and to exchange valuable information.

We look forward to seeing you there!

Please don't forget to register:

www.siemens.com/magnetom-world

MAGNETOM Flash – Imprint

Publisher:
Siemens AG
Medical Solutions
Business Unit Magnetic Resonance,
Karl-Schall-Straße 6, D-91052 Erlangen,
Germany

Editor in Chief: A. Nejat Bengi, M.D.

Associate Editior: Antje Hellwich
(antje.hellwich@siemens.com)

Editorial Board: Dagmar Thomsik-Schröpfer, Ph.D.; Cécile Mohr, Ph.D.; Heike Weh; Bernhard Baden; Peter Kreisler, Ph.D.; Milind Dhamankar, M.D.; Kathleen Giannini; Gary R. McNeal; Sunil Kumar S.L., M.D.

Production: Norbert Moser, Siemens AG, Medical Solutions

Layout: independent Medien-Design
Widenmayerstrasse 16, D-80538 Munich

Printers: Farbendruck Hofmann, Gewerbestraße 5, D-90579 Langenzenn, Printed in Germany

MAGNETOM Flash is also available on the internet:
www.siemens.com/magnetom-world

MAGNETOM Flash with a total circulation of 25,000 copies is sent free of charge to Siemens MR customers, qualified physicians, technologists, physicists and radiology departments throughout the world. It includes reports in the English language on magnetic resonance: diagnostic and therapeutic methods and their application as well as results and experience gained with corresponding systems and solutions. It introduces from case to case new principles and procedures and discusses their clinical potential.

We welcome your questions and comments about the editorial content of MAGNETOM Flash. Please contact us at magnetomworld.med@siemens.com. Manuscripts as well as suggestions, proposals and information are always welcome; they are carefully examined and submitted to the editorial board for attention. MAGNETOM Flash is not responsible for loss, damage, or any other injury to unsolicited manuscripts or other materials. We reserve the right to edit for clarity, accuracy, and space. Include your name, address, and phone number and send to the editors, address above.

Subscription

Please enter your business address

Institution

Department

Title

Name

Street

Postal Code

City

State

Country

MR System used

Please include me in your mailing list for the following Siemens Healthcare customer magazine(s):

- [ ] Medical Solutions
- [ ] MAGNETOM Flash
- [ ] SOMATOM Sessions
- [ ] AXIOM Innovations

Stay up to date with the latest information
Register for:

- [ ] the e-Newsletter

E-mail

- [ ] Yes, I consent to the above information being used for future contact regarding product updates and other important news from Siemens.
- [ ] unsubscribe from info service

Please print clearly!

SUBSCRIBE NOW!

– and get your free copy of future MAGNETOM Flash! Interesting information from the world of magnetic resonance – gratis to your desk. Send us this postcard, or subscribe online at **www.siemens.com/MAGNETOM-World**

MAGNETOM Flash

Siemens AG
Medical Solutions
Magnetic Resonance
Antje Hellwich - Marketing
P.O. Box 32 60
D-91050 Erlangen
Germany

Order No.
A91MR-1000-50C-7600
Printed in Germany
CC MR 01000 ZS 040825.

www.siemens.com/healthcare-magazine

On account of certain regional limitations of sales rights and service availability, we cannot guarantee that all products included in this brochure are available through the Siemens sales organization worldwide. Availability and packaging may vary by country and is subject to change without prior notice. Some/All of the features and products described herein may not be available in the United States.

The information in this document contains general technical descriptions of specifications and options as well as standard and optional features which do not always have to be present in individual cases.

Siemens reserves the right to modify the design, packaging, specifications and options described herein without prior notice.
Please contact your local Siemens sales representative for the most current information.

Note: Any technical data contained in this document may vary within defined tolerances. Original images always lose a certain amount of detail when reproduced.

Siemens AG
Wittelsbacherplatz 2
80333 Muenchen
Germany

Headquarters

Siemens AG, Medical Solutions
Magnetic Resonance
Henkestr. 127
91052 Erlangen
Telephone: +49 9131 84-0

Contact Addresses

Asia/Pacific:
Siemens Medical Solutions
Asia Pacific Headquarters
The Siemens Center
60 MacPherson Road
Singapore 348615
Telephone: +65 9622-2026

Canada:
Siemens Canada Limited
Medical Solutions
2185 Derry Road West
Mississauga ON L5N 7A6
Canada
Telephone: +1 905 819-5800

Europe/Africa/Middle East:
Siemens AG, Medical Solutions
Henkestr. 127,
91052 Erlangen
Germany
Telephone: +49 9131 84-0

Japan:
Siemens-Asahi
Medical Technologies Ltd.
Takanawa Park Tower 14 F
20-14, Higashi-Gotanda 3-chome
Shinagawa-ku
Tokyo 141-8644
Japan
Telephone: +81 35 42 38 489

Latin America:
Siemens S.A., Medical Solutions
Avenida de Pte. Julio A. Roca No 516, Piso 7
C1067ABN Buenos Aires
Argentina
Telephone: +54 11 4340 8400

USA:
Siemens Medical Solutions U.S.A., Inc.
51 Valley Stream Parkway
Malvern, PA 19355-1406
USA
Telephone: +1-888-826-9702